THE UNIVERSITY OF CHICAGO

# REVEALING T-CELL SIGNALING STATES BY 4-DIMENSIONAL LATTICE LIGHT-SHEET MICROSCOPY OF RECEPTOR DYNAMICS

A DISSERTATION SUBMITTED TO

THE FACULTY OF THE DIVISION OF THE BIOLOGICAL SCIENCES

AND THE PRITZKER SCHOOL OF MEDICINE

IN CANDIDACY FOR THE DEGREE OF

DOCTOR OF PHILOSOPHY

COMMITTEE ON CANCER BIOLOGY

BY

JILLIAN NICOLE ROSENBERG

CHICAGO, ILLINOIS

JUNE 2021

# TABLE OF CONTENTS

Supplemental Movies 1-10 are available online as part of this dissertation.

# LIST OF FIGURES

# LIST OF TABLES

# ABBREVIATIONS

ACE2: Angiotensin-Converting Enzyme 2

AO: Adaptive Optics

AO-LLSM: Adaptive Optics Lattice Light-sheet Microscope

CAR-T: Chimeric Antigen Receptor T cell

CD: Cluster of Differentiation

CTLA-4: Cytotoxic T-Lymphocyte-Associated Protein 4

CTLA4B: CTLA-4 Blockade

COVID-19: Caronavirus Disease 2019

DLS: Dynamic Light Scattering

dTHP-1: differentiated THP-1 macrophages

EVLP: *Ex vivo* Lung Perfusion

FBS: Fetal Bovine Serum

FDA: Food and Drug Administration

K5: Lysine Residue 5 mutated MCC

LaMDA: Lattice Light-Sheet Multi-Dimensional Analyses

Lck: Lymphocyte-specific protein tyrosine kinase

LLSM: Lattice light-sheet microscope

MCC: Moth Cytochrome C

NHS: N-hydroxysuccinimide

PALM: Photoactivated Localized Microscopy

PBS: Phosphate Buffered Saline

PD-1: Programmed Death 1

PD-L1: Programmed Death Ligand 1

PD1B: PD-1 Blockade

Pen/Strep: Penicillin Streptomycin

PFOB: Perfluorooctyl Bromide

PLL: Poly L-Lysine

pMHC: peptide major histocompatibility complex

PLA: Polylactice Acid

PS: Phosphatidylserine

PSF: Point Spread Function

RPMI: Roswell Park Memorial Institute Media

SEM: Scanning Electron Microscopy

SHAP: SHapley Additive exPlanations

SIM: Structured Illumination Microscopy

SMAC: Supramolecular Activation Cluster

STED: Stimulated Emission-Depletion Microscopy

STORM: Stochastic Optical Reconstruction Microscopy

TCR: T-cell receptor

TEM: Transmission Electron Microscopy

TIRF: Total Internal Reflection Microscopy

TOCCSL: Thinning Out Clusters while Conserving Stoichiometry of Labeling

UMAP: Uniform Manifold Analysis Platform

VSV: Vesicular Stomatitis Virus

ZAP70: Zeta-chain-associated protein kinase 70

102S: Residue 102 in MCC mutated to Serine

# ACKNOWLEDGEMENTS

I would like to thank my mentor, Dr. Jun Huang, for teaching me how to be a successful, independent scientist. Thank you for allowing me so much creative freedom in choosing and forming my project, and for bringing me to so many conferences and courses where I could learn and discuss my science for others. Lastly, thank you for giving me the opportunity to mentor and teach others, as I was able to discover my passions for leading and mentoring.

I would like to thank my lab, all members past and present, for truly being my family throughout my PhD. My lab has been the most supportive, encouraging, and helpful group of individuals I have ever met. Our time together, be it in the lab, at lunch, or out for a fun impromptu dinner in Chinatown has been the highlight of my time in Chicago. Thank you to Dr. Dibyendu Sasmal for teaching me what a successful PhD looks like. Thank you to Devin Harrison for showing me what dedication and hard work can do, and for always being there to discuss science, academia, and life. Thank you to Andrés Moya-Rodriguez for always making me laugh and for beating all my video games for me. Thank you to Laura Pulido for making everything in the lab easier through organization, cleanliness, and attention to detail, and for always providing conversation to make my day better. Thank you to Chufan Cai and Doremi Feng for being true friends both in the lab and beyond. Thank you to Yifei Hui for being the most patient, kind-hearted spirit and for listening anytime I need to talk. Thank you to Nick Asby for always being available for any conversation and for providing dog photos anytime I need. Thank you to Dr. Nick Ankenbruck for providing humor in any situation and for all of your indispensable life advice. Thank you to Dr. Min Chen for bringing me onto your Nanotrap team, teaching me about nanoparticles, and for sharing all of your incredible photography. Thank you to Thao Cao for bringing such bright energy to the end of my time here. Thank you to Yu “Ethan” Zhao and Tony Pan for listening to my endless ramblings about our lab and Chicago. Though I have not known you long, thank you to Erting Tang and Dr. Xiaolei Cai for joining our lab family. Thank you to all my high school, undergraduate, and graduate student trainees for teaching me how to be a leader and a mentor. And last, but certainly not least, thank you to Guoshuai

“Daniel” Cao for being my partner and rock throughout our entire project. You taught me how to stand up for myself and my science, and for that I will be forever grateful. Thank you for being such a great friend and for introducing me to your culture and food; without you I would not have made it to this day.

I would like to thank my thesis committee: Dr. Barbara Kee, Dr. Megan McNerney, and Dr. Melody Swartz. Thank you for providing crucial guidance to my project, publishing advice, and encouragement throughout my entire project.

I would like to thank the University of Chicago Light Microscopy Core, particularly Dr. Vytas Bindokas and Dr. Christine Labno. You have been such important mentors to both myself and my project. Thank you for taking the time to share your passions for microscopes with me and for spending so much time discussing both my own science and general microscope designs while I spent so many hours in the core collecting and processing data. I could not have had such a successful project without you both.

I would also like to thank my friends and family for their unwavering support. Thank you to my parents for all of your encouragement and efforts to get me to this point; I could not be here without you. Thank you to my brother for providing humor even in my darkest days. Thank you to my friends in the CCB program for coming up with fun breaks from work. Thank you to Anna Stanley-Lee, Alyssa Cruse, and Rachel Kirshtein for always being only a phone call away, for visiting me in Chicago, and for all of your encouragement to keep me going. Thank you to Stephanie Konecki for sharing in my love of home decor, cooking, and Samin Nosrat, and for always meeting up for lunch to brighten my day. Thank you to Jorge Emilliano Medellin for so many de-stressing coffee breaks.

And most importantly, thank you to my partner, Eric Bueter, for everything you have done to support me throughout the most difficult thing we have ever done. Words cannot express my appreciation for you, but I will try. Thank you for being my biggest cheerleader, my best friend, and a safe space for anything I need to talk about. Thank you for keeping me laughing, for showing me how to relax, and for giving me a family away from my own, a home away from home. Thank you for exploring Chicago with me and for introducing me to the wonders of national parks. I cannot wait for this next phase of our life.

# ABSTRACT

Lattice light-sheet microscopy provides large amounts high-dimensional, high-spatiotemporal resolution imaging data of cell surface receptors across the 3D surface of live cells, but user-friendly analysis pipelines are lacking. In this thesis, lattice light-sheet microscopy multi-dimensional analyses (LaMDA) is described, which is an end-to-end pipeline comprised of publicly-available software packages that combines machine learning, dimensionality reduction, and diffusion maps to analyze transmembrane receptor dynamics and classify cellular signaling states without the need for complex biochemical measurements or other prior information. LaMDA is used to analyze images of TCR microclusters on the surface of live primary T cells under resting and stimulated conditions. LaMDA accurately differentiates stimulated cells from unstimulated cells, precisely predicts attenuated T-cell signaling after CD4 and CD28 receptor blockades, provides interesting insight to checkpoint inhibitors, reliably discriminates between structurally similar TCR ligands, and presents coordinated global spatial and temporal changes of TCRs across the 3D cell surface. Finally, in response to the global COVID-19 pandemic that arose in 2019, a nanoparticle entitled "Nanotraps" is presented that inhibits entry of SARS-CoV-2 to ACE2-expressing cells and triggers subsequent phagocytosis by macrophages to clear the virus. The Nanotraps showed a neutralizing capacity of more than 10 times that of its soluble ACE2 or neutralizing antibody counterparts.

# CHAPTER 1: INTRODUCTION

This dissertation describes the use of recently developed high-powered Lattice Light-Sheet Microscopy (LLSM) to study the 4-dimensional T-cell receptor (TCR) dynamics on the surface of live T cells. The following section details the need for and development of LLSM from years of microscopy development, the role of T cells in the immune system, the known TCR signaling cascade, and provides a discussion on the presence of TCR clusters on the surfaces of T cells.

**History of the Microscope: The Advent of LLSM**

The creation of the original microscope dates back to the late 16$^{th}$ century. Microscopes have since been used heavily in the fields of cell and molecular biology to discover the ways in which our cells function. Several advances have been made to improve upon the original compound microscopes. For example, Marvin Minsky patented the first confocal microscope in 1957[1,2]. Confocal microscopes take advantage of the known point spread function (PSF), or the distortion of the image of a point. PSF have a distinct pattern of light diffraction that is unique to the light path of each microscope. Confocal microscopes collect images through a pinhole, which blocks the out-of-focus light, thus limiting the distortion of the PSF and improving upon the final resolution of the image. Now, confocal microscopes can be made to be line-scanning, in which the pinhole scans across the sample during imaging, or spinning-disk, in which a disk of pinholes spins to "move" the pinhole much more quickly[3].

In the late 1980s, a new microscopy technique was created by Daniel Axelrod, called total internal reflection fluorescence, or TIRF[4,5]. TIRF microscopy eliminates out-of-focus light through a different mechanism: light is shone at the sample at an angle such that an evanescent wave is propagated along the surface, e.g. coverslip, and the rest of the light is reflected downward. In this way, only the surface of the sample right at the coverslip, or along the evanescent wave, is illuminated, and no out-of-focus sample is excited[5]. TIRF microscopy is fast and provides high resolution images with little to no

out-of-focus light. However, it cannot image in 3D, and thus, can only be used to image molecules and organelles at the interface of the cell and the coverslip. Due to their existence at the cell surface, TCRs are studied heavily with TIRF microscopy[6–10].

In 1878, Ernst Abbe derived a mathematical equation linking the wavelength of light to image resolution, an equation that still stands today. The "Abbe Diffraction Limit" as it is now called, is about 200 nm for visible light. Recent advances in science have allowed us to "break" the diffraction limit, resulting in super-resolution microscopy techniques. In 1994, Stimulated Emission-Depletion (STED) microscopy was invented[11,12]. STED uses a similar principal to confocal microscopy, in which a depletion laser in the shape of a ring is used to quench signal around a specific size pinhole. The pinhole size is determined by the PSF of the microscope. The depletion ring is then moved across the sample such that fluorescence is quenched enough to break the diffraction limit. However, the depletion ring quenches so much signal that this technique is not feasible for low-light samples. While resolution may vary from system to system, today's STED microscopes can reach resolutions of about 30 nm[13,14]. In 1997, another super-resolution technique termed Structured Illumination Microscopy (SIM) was created[15]. SIM uses a series of laser gratings to shift the phase of the illumination light, then reconstructs the image with higher resolution than is achievable by a single phase of light[16]. SIM can achieve a resolution of about 100 nm[16].

In 2006, three independent groups published similar yet distinct methods for another super-resolution technique, termed localization microscopy. The papers, published by Xiaowei Zhuang[17], Eric Betzig[18], and Samuel Hess[19], were all published within four months of each other. Despite not being the first to publication, Eric Betzig is the only author of these papers to receive the Nobel Prize in Chemistry in 2014 for the technique. Localization microscopy is also based on the principal of the PSF. Knowing that the PSF is a distorted image of a point, we can take any PSF and find the mathematical center, thus cutting out any out of focus light. However, with so many overlapping fluorophores in a sample which are much closer together than the diffraction limit of 200 nm, we cannot calculate the center of any single point. Thus, each localization microscopy technique uses a different method to make fluorophores blink,

such that only a few fluorophores are illuminated in any single image. Hundreds of images are taken, and the final image is a reconstruction of the center point of each fluorescent blink. Localization microscopy techniques have been used to study TCR clustering[20–24], but due to the time it takes to generate a single image, this technique should not be used to image live cells.

While these super-resolution techniques are certainly ground-breaking, they are largely unsuitable for low-light imaging of live cells. TIRF is unable to image a full 3D cell, and thus cannot be used for imaging real-time dynamics across the entire 3D cell surface. Confocal imaging is relatively slow. Further, while a confocal image is being collected only through a pinhole, the entire sample is illuminated, causing high levels of photobleaching and phototoxicity to the sample. The light-sheet microscope, which dates back to 1903[16], solves both the photobleaching and phototoxicity issues of confocal microscopy, the 3D limitation of TIRF, and the live-cell limitation of super-resolution techniques. Light-sheet microscopy uses an illumination light structured into a thin beam, which thus illuminates only a single plane of a sample. This plane is then moved through the sample, achieving 3D imaging. In 2004, the light-sheet microscope got an upgrade to selective plane illumination microscopy (SPIM)[16]. The advent of SPIM brought an increase in usage of light-sheet microscopes.

In 2014, light-sheet microscopy was further improved with Eric Betzig's creation of lattice light-sheet microscopy (LLSM)[25]. LLSM uses an ultra-thin lattice-structured light sheet that dithers back and forth to create a far gentler sheet of light than standard light-sheet microscopy. The LLSM has high axial resolution (~200 nm XY and ~400 nm Z) with negligible photobleaching and out-of-focus light, allowing for extremely high temporal resolution (~1 3D cell/second). Due to the ability to adjust the lattice pattern of the structured sheet, LLSM can also be used for SIM. LLSM had a slow start due to the complicated alignment process[26] (see methods), but is slowly gaining users[26–40]. Furthermore, Zeiss recently announced the launch of its own LLSM system with fully automated calibration[41]. In 2018, Betzig's team further advanced the LLSM by adding adaptive optics (AO)[42]. AO is a principle used by telescopes[25] in which a laser is used to project a "guide star" in order to measure the atmospheric disturbance and

diffraction, which is then corrected for in the final image. The AO-LLSM thus utilizes a two-photon laser to create a guide star within the sample, and corrects for the aberrations with a phase modulation element. This results in extremely clear images with very little distortions. Due to the cost and availability of the AO-LLSM, the microscopy described in this dissertation is conducted with the 2014 LLSM, made commercially available by 3i.

**T Cells: Mediators of Adaptive Immunity**

T cells are the main effector cells of adaptive immunity. T cells signal through a main receptor called the T-cell receptor (TCR) which binds to the peptide-presenting major histocompatibility complex (pMHC) on antigen presenting cells (APCs). TCR signaling also requires co-receptor CD4 or CD8; which co-receptor a T cell expresses determines its function; $CD4^+$ T cells are "helper" T cells, and $CD8^+$ T cells are "cytotoxic" T cells[43]. Adaptive immunity first starts with APC recognition of a foreign antigen. The APCs uptake the foreign antigen and present it on both class I and II MHC. $CD4^+$ T cell recognition of the class II pMHC stimulates the secretion of IL-2, which is required to prime $CD8^+$ T cells[44]. The $CD8^+$ T cells, upon recognition of the class I pMHC and receipt of IL-2 stimulation from the $CD4^+$ T cells, is activated to find and kill cells presenting this antigen on class I pMHCs.

Upon activation, both $CD4^+$ and $CD8^+$ naïve T cells become primed T cells and enter a clonal expansion phase. In the expansion phase, the responsive TCR clone undergoes proliferation, which occurs 24-30 h after *in vivo* introduction of antigen[45]. Primed $CD8^+$ T cells gain the ability to produce cytotoxic molecules granzyme and perforin as well as cytokines IFNγ and TNFα[43]. Following clearance of the infection, $CD8^+$ T cells enter a contraction phase in which about 90-95% of cells die; the surviving cells enter the third phase of infection, becoming long-lived "memory" cells[46]. Memory $CD8^+$ T cells are typically divided into three distinct groups based on function, location, and identifying markers: resident ($T_{RM}$), effector ($T_{EM}$), and central ($T_{CM}$)[44]. How and when these $CD8^+$ T cells become destined to become memory cells is still a point of controversy in the field; some groups believe T cells are destined to become memory cells upon initial priming, while others believe this designation occurs later[44]. Further,

whether $CD4^+$ T cells form a memory compartments is also a controversial topic: the $CD4^+$ compartment shrinks more quickly than its $CD8^+$ counterpart in the contraction phase, and long-lived $CD4^+$ may not require antigen stimulation, raising the question of whether these can actually be called "memory" cells[47].

Prolonged exposure to an antigen, such as in the case of chronic infection[48] or cancer[49], can lead to T-cell exhaustion. Exhausted T cells lose the ability to proliferate, secrete IL-2, and kill target cells, and thus are unresponsive to clearing infection. Furthermore, exhausted T cells lose the ability to create memory T cells[50]. One mechanism of exhaustion was discovered to be the interaction between PD-1 and PD-L1[51]: PD-1 on the surface of T cells binds to PD-L1 either in *cis*[52] or *trans*[53], and blocks activation. It was shown that blocking this interaction can reinvigorate T cells, and has thus been used as a treatment for chronic infections such as HIV and CMV[54], as well as cancer[55]. However, only a fraction of patients respond to checkpoint inhibitor therapy[56], and responders often acquire resistance[57]. In addition, PD-1/PD-L1 signaling does not account for the full exhaustion pathway; the exact pathway to exhaustion has not yet been fully delineated[50,53,58,59].

**T-Cell Receptor (TCR) Signaling**

The main signaling molecule on a T cell is the TCR. TCRs have an α and a β chain[60], expressed at the TRAC locus in the genome[60], that together bind to and recognize the pMHC. The TCR exists at the surface of the T cell complexed together with CD3[60]. CD3 has six components: one γ chain, one δ chain, two ε chains, and two ζ chains, which form a εδ-heterodimer, a γε-heterodimer, and a ζζ-homodimer[61,62]. The γ, δ, and ε chains each have one ITAM, while the ζ chains have 3 ITAMs each. CD3 is stable at the cell surface without the TCR, but the TCR is not stable at the cell surface without CD3[61,62]. In a resting T cell, the CD3ζ chains are positively charged, and associate with the negatively charged plasma membrane[63]. Upon identification of a pMHC presenting a foreign peptide, the TCR ligates with the pMHC and CD4/8 binds to the MHC. The TCR changes conformational shape upon ligation[63], and CD4/8 recruits kinase Lck, which phosphorylates the ITAMs on CD3. Phosphorylation of the CD3ζ ITAMs adds

negative charge, causing dissociation from the plasma membrane[63]. The phosphorylated CD3ζ then becomes a binding site for ZAP-70[64], which is further activated and stabilized by phosphorylation by Lck. ZAP-70 activates LAT, which is a main signaling molecule in the TCR cascade[65–67]. LAT activates the calcium release pathway, which globally changes the membrane potential and is thus a positive feedback loop for maintaining CD3ζ dissociation from the membrane. LAT also activates cytoskeletal rearrangement, cell cycle, survival, growth pathways, and induces transcriptional regulation[65–67].

For complete TCR signaling, a secondary signal must come from co-stimulatory molecule CD28[68–71]. CD28 binds to ligands CD80 and CD86 (also known as B7.1 and B7.2, respectively). Upon ligation, CD28 phosphorylation activates PI3K, which is also activated by LAT for signal amplification. In addition, CD28 recruits PKCθ, which, through further downstream signaling, activates cell growth, effector function, and survival pathways. Another co-stimulatory molecule is CD45, a common marker for lymphocytes. CD45 is a tyrosine phosphatase that is required to activate Lck by removing its inhibitory phosphorylation site at the C-terminus[72]. CD45 is also an important molecule for T-cell maturation and differentiation.

In addition to co-stimulatory molecules, there are a number of co-inhibitory molecules present on the T-cell surface which are thought to dampen TCR signaling in an effort to prevent overstimulation and exhaustion. One such molecule is CTLA-4, which, interestingly, binds to the same ligands as CD28, but with higher affinity[71,73]. However, upon ligation with CD80/86, CTLA-4 sends an inhibitory signal, dampening TCR activation[74,75]. CTLA-4 has also been shown to sequester CD80/86 from CD28 at the immunological synapse[76], and is thus thought to be a temporal negative regulator to prevent overstimulation. Another co-inhibitory receptor is PD-1, discussed above. Unlike CTLA-4 which directly interferes with TCR co-stimulation, PD-1 inhibits downstream TCR signaling cascades: upon ligation, PD-1 recruits phosphatase SHP-2[77], which de-phosphorylates, thus inactivating, CD3ζ, ZAP-70, and PKCθ[78]. As described above, these co-inhibitory molecules have been deemed “checkpoint inhibitors” and are targeted as a method of reinvigorating T cells for cancer immunotherapy[55].

**T-Cell Receptor (TCR) Clustering**

One important question that remains controversial in T cell biology is whether or not TCRs exist in non-covalently linked clusters, termed nanoclusters or microclusters, before signaling. The clustering of TCRs after TCR engagement is fairly well accepted: the trafficking of TCRs to the supramolecular activation cluster (SMAC) at the immunological synapse is a phenomenon that is easily observed by a simple microscope[79–82]. Originally identified by Kupfer *et al.*[82], the SMAC has been delineated into three layers: the central SMAC (cSMAC), peripheral SMAC (pSMAC), and the distal SMAC (dSMAC)[83]. The cSMAC contains the TCR, CD3, CD28, and PKCθ[83]. The pSMAC contains adhesion molecules, such as ICAM-1 and integrin LFA-1[84]. The dSMAC was shown to contain CD45, which has a much longer intracellular tail[85]. However, these studies were conducted using TIRF imaging on a functionalized supported lipid bilayer, and thus may not be representative of what occurs when a T cell interacts with the 3D APC surface. Still, while the organization of the synapse is controversial, the clustering of TCRs following antigen recognition is widely accepted. However, TCRs may also cluster before signaling and simply aggregate upon antigen recognition.

One school of thought postulates that clustering of TCRs allows for an increase in avidity of TCRs binding to pMHCs, and thus enables signal amplification much more quickly[86]. There is significant evidence supporting this theory. For example, fracture transmission electron microscopy (TEM) has shown the TCRs exist in clusters on the resting cell surface[87], and that these clusters are disrupted by MβCD, a lipid raft dissociator[88]. However, TEM cannot image live cells, and there is a significant amount of sample preparation that can cause artifacts. Other groups have utilized localization microscopy to claim that TCRs exist in nanoclusters prior to signaling, which, upon activation, increase in molecular density[89,90]. However, localization microscopy also should not be conducted in live cells. Other groups have also used confocal[87,91,92] and TIRF microscopy[93–95] to show pre-synaptic clustering of TCRs; however, TIRF cannot image in 3D, and both TIRF and confocal are diffraction-limited.

The other school of thought postulates that the clustering of proteins causes each necessary molecule of the signaling complex to be segregated from one another, thus suppressing initial signaling

events[96]. One group claims that the mathematical recombination of images in localization microscopy causes artifacts that result in the overcounting of points[97]. However, the maximum resolution of STORM[17] is about 25 nm, and with the receptor size at ~10 nm[98], even single-pixel signal could be a clustered TCR. Brameshuber *et al.* used an elegant approach termed TOCCSL (thinning out clusters while conserving stoichiometry of labeling), which labels TCRs with two different colors, photobleaches an area, and then tracks the signal that comes into the frame. They showed that while CD3 and TCR colocalize in their system, two-color TCRs do not, indicating that the TCRs exist at the surface in monomers[99]. However, there is no way to perfectly ensure an even distribution of labeling or to exclude the possibility of same-color clustering.

In truth, this question will likely stay unanswered until an imaging technique is developed with nanometer resolution on live cells. As this technology does not currently exist, we have no way to definitively prove whether or not TCRs form small clusters prior to signaling that aggregate into larger clusters upon antigen recognition, or whether the TCRs are truly monomeric prior to signaling.

# CHAPTER 2: MATERIALS AND METHODS

## METHODS FOR CHAPTERS 3-6

*Cell culture*

Cytosolic mCherry-transduced CH27 cells were a gift generously donated by Dr. Enfu Hui. To obtain blasting T cells, 5C.C7 mouse spleen was harvested and run through a 70 μm cell strainer with warm complete RPMI. Splenocytes were resuspended in 5 mL of RBC Lysis Buffer (Life Technologies) for 5 min, washed three times, and resuspended in 5 mL of complete RPMI. MCC peptide (ANERADLIAYLKQATK; 10 μM) was added to stimulate T cell proliferation, and recombinant mouse IL-2 (100 U/mL, Sigma-Aldrich) was added the following day. Blasting T cells were used on days 6–10 after peptide pulsing. mCherry-CH27 cells and 5C.C7 blasting T cells were both maintained in complete medium (RPMI 1640 supplemented with 10% [v/v] FBS, 1% [v/v] Pen/Strep, L-glutamine [2 mM], 2-mercaptoethanol [50 μM]).

*Cell Preparation*

Cells were prepared as previously described[26]. Briefly, mCherry-CH27 cells were used as antigen presenting cells for imaging experiments. Dead mCherry-CH27 cells were first removed by Ficoll-Paque Plus (GE Healthcare, cat: 17-1440-03) density gradient centrifugation (centrifuged at 930 × g for 10 min at 4 °C, acc/dec: SLOW/SLOW). Live mCherry-CH27 cells were washed three times with complete medium, and then incubated with 10 μM K5 (ANERADLIAYFKAATKF), MCC (ANERADLIAYLKQATK) or 102S (ANERADLIAYLKQASK) for 3 h at 37 °C and 5% $CO_2$. Peptide-pulsed mCherry-CH27 cells were then washed three times and resuspended in imaging media (phenol red-free Leibovitz's L-15 medium supplemented with 10% [v/v] FBS, 1% [v/v] Pen/Strep, L-glutamine [2 mM]) for use.

Naïve T cells were prepared by negative isolation using 5C.C7 transgenic mouse spleens. Mouse splenocytes were prepared by Ficoll-Paque Plus (GE Healthcare, cat: 17-1440-03) density gradient

centrifugation (centrifuged at 930 × g for 10 min at 4 °C, acc/dec: SLOW/SLOW) to remove dead cells. Naive $CD4^+$ T cells were then harvested by negative isolation (MojoSort Mouse CD4 T Cell Isolation Kit, BioLegend, cat: 480033). Cells were washed three times with complete medium and incubated with Alexa488-labeled anti-TCRβ (2 μg; clone H-57, Biolegend) antibody Fab for 30 min at 37 °C and 5% $CO_2$. After three washes, naïve T cells were resuspended in imaging media for use.

Day 6-10 blasting T cells were prepared by Ficoll-Paque Plus (GE Healthcare, cat: 17-1440-03) density gradient centrifugation (centrifuged at 930 × g for 10 min at 4 °C, acc/dec: SLOW/SLOW) to remove dead cells. Live blasting T cells were washed three times with complete medium and incubated with Alexa488-labeled anti-TCRβ (2 μg; clone H-57, Biolegend) antibody Fab for 30 min at 37 °C and 5% $CO_2$. After three washes, blasting T cells resuspended in imaging media for use.

*CD3ζ-GFP Transduction*

Primary 5C.C7 T cells were retrovirally transduced with CD3ζ-GFP according to a previously published method[100]. Briefly, calcium phosphate precipitation was used to transfect MIG-CD3ζ-GFP vector into ecotropic platinum-E retroviral packaging cells. Supernatant containing virus was harvested after 48 and 72 h and filtered through 0.2 μm cellulose acetate membrane. Splenocytes isolated from 5C.C7 mice cultured in complete RPMI were stimulated with anti-CD3ε mAb (5 μg/mL; Clone 145-2C11, University of Chicago Monoclonal Antibody Facility), anti-CD28 mAb (0.5 μg/mL; Clone 37.51, Biolegend), and recombinant human IL-2 (40 U/mL; Peprotech). A 6-well plate was coated with Retronectin (12.5 μg/mL; Clontech) in PBS at 4 °C overnight, then centrifuged for 90 min at 3,000 x g with 2 mL of viral supernatant. Day 1 activated splenocytes were transferred to plate with viral supernatant, protamine sulfate (4 μg/mL) was added, and plate was centrifuged at 800 × g for 90 min. After 24 h, medium was replaced with fresh viral supernatant containing protamine sulfate (4 μg/mL), and plate was centrifuged at 800 × g for 90 min. After 16 h, transduction efficiency was determined by examining GFP fluorescence using flow cytometry.

*Fab preparation*

All Fabs used in this study were prepared using a Micro Fab Preparation Kit (Thermo Fisher Scientific). Briefly, anti-TCRβ, anti-CD4, and anti-CD28 whole antibodies were prepared with desalting column, then digested with papain, a nonspecific thiol-endopeptidase, for 6 h on tabletop shaker at 37 °C. Digested Fabs were purified according to kit instructions. Fab purification was confirmed with SDS-PAGE gel electrophoresis.

*Signaling Perturbation Assays*

For PP2 assay, day 6-10 blasting T cells were pre-incubated with PP2 (10 μM; 4-Amino-5-(4-chlorophenyl)-7-(t-butyl)pyrazolo[3,4-d]pyrimidine; Sigma-Aldrich) for 1 h at 37 °C and 5% $CO_2$. Pre-treated cells were imaged at 37 °C and 5% $CO_2$ in the presence of 10 μM PP2.

For CD4 and CD28 blockade, an anti-CD4 (clone Gk1.5, BioLegend) or anti-CD28 (clone 37.51, BioLegend) Fab was prepared and purified with Micro Fab Preparation Kit (Thermo Fisher Scientific). Day 6-10 T cells were pre-incubated for 1 h at 37 °C and 5% $CO_2$ with anti-CD4 Fab (2 μg/mL) or anti-CD28 Fab (4 μg/mL) then imaged in the presence of 2 μg/mL Fab.

*Lattice Light-sheet Microscopy*

Version 2 of the Lattice Light Sheet Microscope (3i) was used for 4D imaging experiments. The LLSM was aligned daily according to manufacturer's instructions (See Fig. 1). Briefly, 30 μL fluorescein (1mg/mL stock) was added to the water bath, the lattice pattern was visualized (Fig. 1A), and the single Bessel beam was centered (Fig. 1B). The bath was washed with 200 mL water, and then the bath was filled with imaging media and warmed to 37 °C. Standard fluorescent beads were used to further optimize the galvo, objective collar, and focus micrometer alignment (Fig. 1C-F)[26]. Point spread functions were collected for later deconvolution. Round coverslips (5 mm) were prepared prior to imaging by incubation with 0.1%

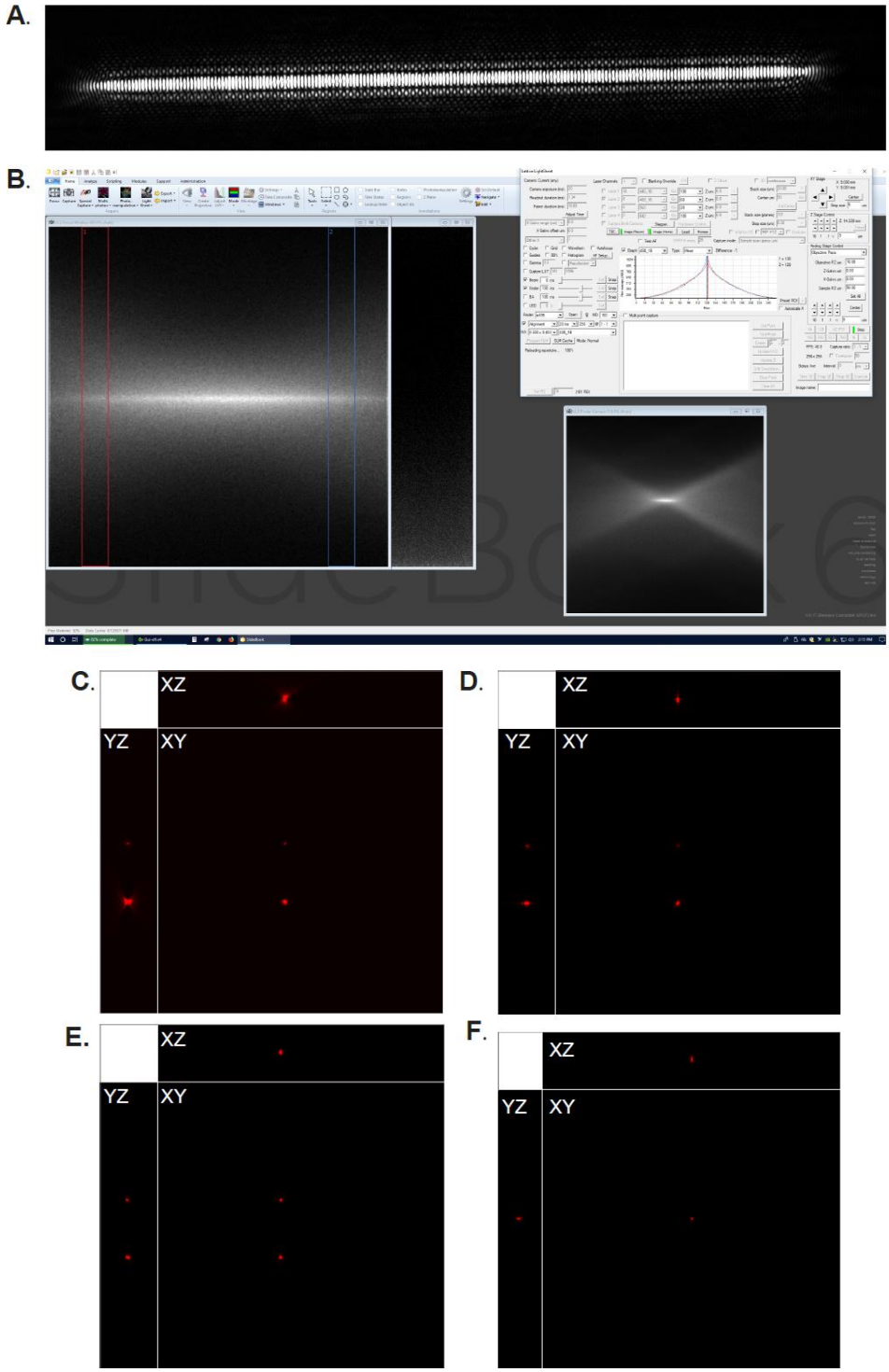


**Figure 1: LLSM Alignment.** (**A**) Desired beam pattern for LLSM imaging experiment. (**B**) Screenshot of the beam alignment process; on the left is the focus window showing the narrowed, focused beam; at the top right is a graph showing that the beam is centered within the window; at the bottom right is the finder camera, which should also be a thin, focused beam. (**C**) Maximum intensity projections (MIPs) of a bead by objective scan. (**D**) Maximum intensity projections (MIPs) of a bead by z-galvo scan. (**E**) Maximum intensity projections (MIPs) of a bead by z+objective scan. (**F**) Maximum intensity projections (MIPs) of a bead by sample scan. This figure is reproduced from Rosenberg, et al., *JoVE* 2020.

[w/v] solution of Poly-L-Lysine for 30 min. Poly-L-Lysine was aspirated, and coverslips were allowed to dry. To prepared coverslips were added 200,000 peptide-pulsed mCherry-CH27 cells. Cells were allowed to settle for 10 min before adhering to sample holder and placing in LLSM bath. T cells (200,000) were added dropwise to the LLSM bath above the coverslip and imaged immediately. Imaging was conducted with dither set to 3 and 10 ms exposures. Z-steps (60) were collected with a 0.4 μm step size. Cells were imaged for no more than one hour before exchanging with fresh cells.

*Image Processing*

Data were deskewed and deconvolved using LLSpy (cudaDeconv) software, used under license from Howard Hughes Medical Institute, Janelia Research Campus; collected point spread functions (PSF, collected under imaging conditions) were used to deconvolve, and 20 iterations were conducted. Bleach correction was conducted in ImageJ using histogram matching. Deskewed, deconvolved, and debleached videos were imported into Imaris (Bitplane) for rendering and tracking. Tracking TCR microclusters was conducted with the "surfaces" module using the Autoregressive Motion Expert tracking method; any two consecutive surfaces were allowed to move a maximum distance of 0.5 μm and disappear for no more than 3 frames to be considered on one track; watershed was not enabled. The surfaces module was also used to create a surface of the antigen presenting cell, and a distance map was made extending outward from the antigen presenting cell surface. Surface module statistics were exported for every TCR surface. Thus, for all following sections of the Methods, "surfaces" or "surface modules" refer to the segmentation and tracking of TCR microclusters conducted by Imaris.

*Data Preprocessing*

For each cell, the raw surface module statistics from the TCR microcluster tracks were imported and processed in R as follows. All non-numerical or missing statistics values were removed. All statistical variables were then combined into a dataframe with rows as unique surface modules and columns as the

different statistical variables, including track-specific variables. For the initial parameter extraction from Imaris, 36 variables out of 134 available parameters were collected[33]. These variables were selected by refraining from fitting a certain shape to the surface unit, thus removing all shape-specific features such as "BoundingBoxAA Length" or "Ellipsoid axes". Additionally, only first-order measurements were included where first and second order are available, so as to minimize errors in tracking; for example, displacement XYZ was included, but not displacement$^2$, as any error in connecting the two surface units along the track would be propagated. As a separate example, all acceleration measurements were also excluded, as they depend on velocity measurements, which depend on the displacement. This would compound any "displacement error". Redundant features were preserved (such as standard deviation vs. variation of speed along track), as the XGboost classifier would only select one parameter to analyze at a time, thereby self-excluding the effect of redundant parameters. To normalize the dynamic range, all intensity-related variables (e.g., Mean Intensity, Max Intensity, Min Intensity, etc.) and all size-related variables (e.g., Area, Volume, Number of Voxels, etc.) were then log transformed.

*XGboost Decision Trees Ensemble Binary Classifier*

To build the classifier and make predictions, all data were further processed as follows. For each cell, 19 out of the 36 variables were selected as features of interest (see Data Sharing and Availability for complete list). In this subset, all track-specific (as opposed to surface-specific) parameters were removed in order to focus the decision tree on each surface (or TCR microcluster), rather than each track, as an individual unit. The only exception was Track Duration, which is important for lifetime distribution studies. For a series of surface modules that were assigned to the same track by Imaris, the track duration feature values were defined as the temporal length of that track (i.e., the same value for surface modules of the same track). In addition, position XYZ was removed, as the position of a surface is always relative to the orientation of the cell in that particular video, therefore irrelevant to compare across videos. The chosen statistics from all microclusters on all cells were then pooled for each group to avoid bias on the biological variation from cell to cell. Surface modules with Mean Intensity ($I_{mean}$) values lower than mean($I_{mean}$)-

1.5×IQR($I_{mean}$) were removed as they are likely to be noise rather than a true surface module. Then, all statistics were standardized: $\frac{x-\bar{x}}{SD(x)}$.

The processed data were then used to train a binary classifier to differentiate between microclusters from resting cells and microclusters from stimulated cells as follows. Of the four groups of cell types, microclusters from stimulated blast T cells and resting naïve T cells were chosen to train the classifier, which was later tested on the stimulated naïve cells and resting blast cells. This division of cell types was chosen for two reasons: (1) to avoid any strong correlation within the same cells; and (2) to test against the confounding effect of "past stimulation" (i.e., naïve vs. blast). To build the classifier, a "train-test-validate" approach was used to avoid overfitting (Fig. S1I). Thus, the processed data of stimulated blast T cells and resting naïve T cells were divided into a training set (75%; 117,066 surface modules), validation set (17.5%; 27,316 surface modules) and internal test set (7.5%; 11,705 surface modules). The binary classifier was built as a XGBoost logistic regression decision tree ensemble, using the caret package (v.6.0) in R, with 5-fold cross-validation and the following parameters: nrounds = 150; max_depth = 3; eta = 0.4; gamma = 0; colsample_bytree = 0.8; min_child_weight = 1; and subsample = 1. Feature importance was then assessed using the SHAP values extracted from the xgb.plot.shap function. All subsequent plots were constructed using the ggplot2 (v.3.2.0) and the ggpubr (v.0.2.1) package in R. Finally, the model was tested on every surface module (i.e., TCR microclusters) from new data (stimulated naïve and resting blast categories) to predict whether these TCR microclusters were from stimulated blast T cells or from resting naïve T cells. The final label was assigned to be the one with greater predicted probability (i.e., either stimulated blasting T cells or resting naïve T cells).

*XGboost Decision Tree Ensemble Softmax Classifier*

To differentiate multiple ligands, a separate multi-class XGboost classifier was constructed as follows. For each cell, the same 19 out of 36 variables as used for the initial XGboost Decision Tree Ensemble Binary Classifier were selected; however, a 20$^{th}$ variable, average distance to antigen presenting

cell, was added. The last feature was not applicable to the binary classifier above because the resting cells do not encounter antigen presenting cells, but it is applicable to all classes here. Surface modules with Mean Intensity ($I_{mean}$) values lower than mean($I_{mean}$)-1.5×IQR($I_{mean}$) were removed since they are likely to be noise rather than a true surface module. Then, all statistics were standardized:$\frac{x-\bar{x}}{SD(x)}$.

The processed data of microclusters from blasting T cells stimulated by MCC, 102S, and K5 were pooled and divided into a training set (75%; 126,254 surface modules), validation set (17.5%; 29,460 surface modules) and test set (7.5%; 12,623 surface modules). The softmax classifier was built as a XGBoost decision tree ensemble using softmax probabilities as the objective, using the caret package (v.6.0) in R, with 5-fold cross-validation and the following parameters: nrounds = 500; max_depth = 6; eta = 0.3; gamma = 0; colsample_bytree = 1; min_child_weight = 1; and subsample = 1. The final model was used to re-predict the probability of every surface module from the blasting T cells stimulated by MCC, 102S, and K5. The final label was assigned to be the peptide (MCC, 102S, or K5) with greatest predicted probability. Results were plotted using the ggplot2 (v.3.2.0) and the ggpubr (v.0.2.1) package in R.

*Weibull Distribution*

Weibull distribution[101] is a commonly used statistical distribution that describes lifetime distribution. The three-parameter Weibull model we used is of the form:

$$f(T) = \frac{\beta}{\eta}(\frac{T-T_0}{\eta})^{\beta-1}\exp(-\frac{T-T_0}{\eta})^{\beta}$$

where:

$T \geq 0;\ \eta > 0;\ \beta > 0$

A Weibull distribution was used to fit the raw track duration values for each group using the WeibullR (v.1.0.10) package in R. The location ($T_0$), shape ($\beta$), and scale ($\eta$) parameters were extracted directly from the model. The mean life-time values were calculated as:

$$\bar{T} = T_0 + \eta \cdot \Gamma(\frac{1}{\beta} + 1).$$

*UMAP*

Pre-processed data were separately processed as an independent validation of the XGboost classifier. For each cell, the same 19 out of the 37 variables as used for the XGboost classifier were selected as features of interest (see Data Sharing and Availability for complete list). The chosen statistics from all cells of all groups were then pooled for each group to avoid bias on the biological variation from cell to cell. Surface modules with Mean Intensity ($I_{mean}$) values lower than mean ($I_{mean}$)-1.5*IQR ($I_{mean}$) were removed since they are likely to be noise rather than a true surface module. Then, all statistics were then standardized:$\frac{x-\bar{x}}{SD(x)}$. Then data of the groups of interest were then pooled and used to build a UMAP[102] using the uwot (v.0.1.3) package in R with parameters: min_dist = 0.1; n_neighbors = 25; all others set to default. All subsequent plots were constructed using the ggplot2 (v.3.2.0) and the ggpubr (v.0.2.1) package in R.

*Diffusion Maps*

To construct the diffusion maps[103], pre-processed data were further processed similarly to the above UMAP, except that only seven variables were selected (see link in Data and Software Availability for complete list). These seven variables were selected from the distinguishing features identified by both the supervised XGboost classifier and the unsupervised UMAP. First, the six features from the SHAP value analysis were chosen. However, "Time since Track Start" and "Track Duration" are partially redundant. While "Track Duration" indicates the stability of the microcluster on the surface of the T cell, "Time since Track Start" simply indicates the order the microclusters appear along this track, and therefore has less physical meaning. Thus, "Track Duration", was selected and "Time since Track Start" was excluded. In addition, "Mean Intensity" was selected over "Median Intensity", since the former is a more common analysis metric. Finally, "Area" and "Speed" were also selected, as they encode independent information that have not been captured by the initial 5 features; for instance, surface units with the same volume can have different shapes, thereby lending to different surface area.

To conserve computational resources, a subset of 8,000 surface modules were randomly sampled from every group. Data from four core groups, including stimulated blast T cells, stimulated naïve T cells, resting naïve T cells, and resting blast T cells, were pooled and used to build the diffusion maps using the diffusionMap (v.1.1.0.1) package in R with default parameters. Nystorm out-of-sample extension was then used to estimate the diffusion coordinates of surface modules of other groups. All subsequent plots were constructed using the ggplot2 (v.3.2.0) and the ggpubr (v.0.2.1) package in R.

*Pseudo-energy Plots*

For each group, the diffusion coordinates of the 8,000 sampled surface modules were used to build its pseudo-energy plot. The local probability density, $\hat{p}(\vec{x})$, at each data point on the diffusion map was estimated using the ks-package (1.11.5) in R. The density values from the diffusion map embedding coordinates can be used to derive Free Energy Surface as follows:

$$\beta G(\vec{x}) = -\ln \hat{p}(\vec{x}) + const$$

Where $\beta = \frac{1}{k_B T}$; G is the Gibbs free energy, and $\hat{p}(\vec{x})$ is the estimated local probabilistic density on the diffusion map. Here, we used $-\ln \hat{p}(\vec{x})$ as a pseudo-energy since we cannot experimentally determine the constant term, but this pseudo-energy should be linearly related to the Gibbs free energy and thus gives a good representation of the free energy surface[104].

**METHODS FOR CHAPTER 7**

*Synthesis of Nanotraps*

To synthesize the Nanotraps, we employed a two-step method developed for polymer-lipid hybrid nanoparticles, in which the polymer and lipid components were prepared separately and combined at the end of the process. The PLA nanoparticles were prepared in accordance with existing methods[105] through an oil-in-water emulsion solvent evaporation process. 100 mg of PLA and 100 µL of perfluorooctyl bromide

(PFOB)[106] were dissolved in 3.5 mL of dichloromethane. The organic phase was mixed with 20 mL of 2.0% PVA solution. The mixture was emulsified by sonication (Fisher Sonics) on ice for 2 min. The dichloromethane in the emulsified mixture was evaporated under magnetic stirring at 300 rpm for 3-4 h at room temperature. The resulting solution was centrifuged, and the pellets were washed with PBS 3 times (5,000×g for 10 min), and then the pellets were lyophilized and stored at 4°C before use. For any fluorescence labeling, 0.05 mg DiD or DiO was added into the 100 mg PLA organic phase when preparing the Nanotraps. For PLA nanoparticles with size 200 nm, 100 mg of PLA was emulsified with 2.0% PVA and the supernatant was collected after centrifugation instead of the pellet. For PLA nanoparticles with size 500 nm, 100 mg of PLA and 100 µL PFOB were mixed, then emulsified with 2.0% PVA and the pellets were collected after centrifugation. For PLA nanoparticles with size 1200 nm, 100 mg of PLA and 100 µL PFOB were mixed and emulsified with 1.0% PVA and the pellets were collected after centrifugation. For further details on the synthesis of PLA nanoparticles with varying sizes, please see Table 1.

Functionalized PLA-nanoparticles composed of 15% phosphatidylserine and 0.5% DSPE-PEG2000-biotin were prepared by dissolving DOPS (0.388 µmol), DSPC (1.292 µmol), cholesterol (0.775 µmol), DSPE-mPEG2000 (0.166 µmol) and DSPE-PEG2000-biotin (0.013 µmol) at a molar ratio of 10:120:60:9:1 in dichloromethane. The dichloromethane solvent was slowly evaporated by heating the lipid solution at 55°C to remove the solvent and further dried in a vacuum drying oven to produce a dried lipid film. The lipid film was reconstituted in 2 mL of PBS (pH 7.4) containing 0.2 mg PLA nanoparticles and the contents were hydrated at 60°C under ultrasonication (Branson CPX5800H). Then the mixture was sonicated with a sonicator probe (Fisher Sonics) for 2 min (100 W, 22.5 kHz, 30% amplitude). Formulations for Nanotraps with different phosphatidylserine surface densities were listed in Table 2.

To synthesize Nanotrap-ACE2, 1 mg of the biotin functionalized PLA nanoparticles were then incubated with streptavidin (34.25 µL, 2 g/L) on ice for 40 min under magnetic stirring. The resulting solution was centrifuged at 5,000×g for 10 min and washed with 1 mL PBS for 3 times to remove excess streptavidin. The pellet was resuspended in 100 µL PBS and incubated with biotinylated ACE2 (Bioss

**Table 1: Formulations of polymer core with varying sizes**

| Size (nm) | Collected Fraction | PFOB | PVA |
|---|---|---|---|
| 200 | supernatant | no | 2% |
| 500 | pellet | yes | 2% |
| 1200 | pellet | yes | 1% |

**Table 2: Formulations of lipid shell with different phosphatidylserine densities (molar ratios)**

| Formulation | DOPS | DSPC | Cholesterol | DSPE-$mPEG_{2000}$ | DSPE- $PEG_{2000}$-biotin |
|---|---|---|---|---|---|
| 0% PS | 0% | 65% | 30% | 4.5% | 0.5% |
| 5% PS | 5% | 60% | 30% | 4.5% | 0.5% |
| 10% PS | 10% | 55% | 30% | 4.5% | 0.5% |
| 15% PS | 15% | 50% | 30% | 4.5% | 0.5% |

Antibodies) for 30 min on ice and any free ACE2 were removed by washing with PBS against an Ultra-centrifugal tube (100kDa) for 3 times (3,000×g for 10 min). The resulting PLA@DOPS/ biotin~SA~ACE2 nanoparticle was termed as Nanotrap-ACE2.

Nanotrap-Antibody was synthesized by combining 15% DOPS (0.313 mg, 0.386 μmol), 50% DSPC (1.018 mg, 1.287 μmol), 30% cholesterol (0.300 mg, 0.773 μmol) and 5% DSPE-PEG2000-NHS (0.370 mg, 0.129 μmol) in dichloromethane. The lipids mixtures were vacuum dried overnight, and the resulting thin film was hydrated with PLA-NPs PBS solution under ultrasonic water bath and further reacted with 100 μg of SARS-COV-2 neutralizing antibody (Sino Biological) for 4 h at 4℃. Any free antibodies were removed by washing with PBS for 3 times (5,000×g for 10 min).

*Characterization of Nanotraps*

The sizes of Nanotraps were measured by a dynamic light scattering particle size analyzer (Malvern Zetasizer). Briefly, 1 μL of Nanotraps were dispersed in 0.1× PBS and further dispersed in ultrasonic water bath for 10 min before testing. The size measurement was carried at 25℃ with count rates within 300-500 kcps and measured 3 times. The zeta potentials of Nanotraps were performed by a Möbiuζ system (Wyatt Technology). The data were presented as mean ± SD.

AF488-labeled anti-ACE2 antibody (Santa Cruz Biotechnology) was added to the Nanotrap-ACE2 for 30 min on ice and centrifuged at 5,000×g for 10 min, the pellet was washed with PBS for 3 times. The resulting Nanotraps were resuspended in 50% glycol and imaged by total internal reflection fluorescence microscopy (Nikon) with 488 nm and 647 nm excitation lasers and 200 ms exposure. Line scans were performed in Fiji.

The sizes and morphologies of the Nanotraps were studied by scanning electron microscopy. Briefly, 10 μL of Nanotrap-ACE2 were diluted in MiliQ water and further dispersed on ultrasonic water bath for 10 min before adding onto a silicon chip. 40 μL of SARS-CoV-2 spike pseudotyped lentivirus was fixed by 4% PFA at 37℃ for 30 min, the virus was then washed by PBS 3 times using an Amicon Ultra-15

Centrifugal Filter (pore size 100 kDa) at 3,000×g, 10 min. The resulting fixed virus was incubated with 10 μL Nanotraps-ACE2 at 37°C for 1 h and added onto the 1 $cm^2$ silicon chip followed by airdrying overnight. After dehydration, the samples were coated with 8 nm platinum/palladium by sputter coater (Cressington 208HR). The scanning electronic microscope (Carl Zeiss Merlin) was used to image the morphology of the Nanotraps with an accelerating voltage of 2.0 kV. For each sample, more than 10 measurements with different magnification were performed to ensure the repeatability of the results. For TEM imaging, 10 μl of the Nanotrap solution was drop-cast on a carbon film supported TEM grid (Ted Pella Inc, 01843) which was pre-treated with oxygen plasma. Then the grid was gently rinsed with DI water droplets and stained with 1% uranyl acetate aqueous solution for 1 min. The resultant solution was gently removed with filter paper. The sample was then imaged by an FEI Tecnai G2 F30 electronic microscope at 300 kV after thoroughly drying.

For long-term storage, the Nanotraps were freeze-dried into solid powder using a lyophilizer (Freezone 6, Labconco). Briefly, the Nanotrap solution was transferred into Eppendorf tubes and frozen on dry ice. The lid of the frozen tube was removed and quickly embedded with parafilm; holes were punctured in the parafilm using pipette tips. The tubes were placed in the glass tank connected to a lyophilizer with lids up. The lyophilizer was vacuumed using an oil-pump such that any water in the tube was sublimated under –53.3°C for 24 h, resulting in the Nanotrap powder. The tubes with Nanotrap powder were sealed by parafilm and immediately stored in a -20°C freezer. The Nanotrap powder was reconstructed six months later by adding PBS solution followed by ultrasonication.

The density of surface ACE2 or neutralizing antibody on the Nanotrap surface was measured by flow cytometry[107]. DiD-loaded Nanotrap-ACE2 was stained with anti-ACE2-PE (Sino Biological) for 30 min on ice. DiD-loaded Nanotrap-Antibody was stained with anti-IgG-PE (BioLegend) for 30 min on ice. Double positive populations were gated, and then PE Quantitation Beads (BD Quantibrite) were used to calculate surface densities according to manufacturer's instructions.

*Cell lines*

HEK293T-ACE2 cells were provided by Integral Molecular (Integral Cat# C-HA102) and were cultured by cell culture media containing DMEM + 10% FBS + 10 mM HEPES + 1% Penicillin-Streptomycin. Human lung epithelial cell line A549 cells were obtained from (ATCC® CCL-185™) and cultured in DMEM + 10% FBS + 1% Penicillin-Streptomycin. THP-1 cells were kindly provided by Dr. Aaron Esser-Kahn and cultured in RPMI 1640 + 10% FBS + 1% Penicillin-Streptomycin. All cells were maintained in a $CO_2$ incubator (Thermo Scientific, STERI-CYCLE i250) at 37°C and 5% $CO_2$. Vero E6 cells (ATCC) were infected under biosafety level 3 conditions with SARS-CoV-2 (nCoV/Washington/1/2020, kindly provided by the National Biocontainment Laboratory, Galveston, TX).

*Flow cytometry analysis of Nanotraps phagocytosis*

Macrophage differentiation was conducted as follows[108]: THP-1 cells were treated with 150 nM PMA for 24 h and replaced by fresh culture medium for another 24 h. The differentiated THP-1 cells were harvested as dTHP-1 macrophages and maintained in RPMI 1640 supplemented with 10% FBS and 1% Penicillin-Streptomycin. The dTHP-1 macrophages were then released from the plate with Trypsin-EDTA (0.25%) and cell number was counted by a hemocytometer. 1 million dTHP-1 macrophages were seeded into each 6-well plate overnight, and DiO-labeled Nanotraps (200, 500, and 1200 nm) were incubated with dTHP-1 macrophages for 0, 24, or 48 h. For phosphatidylserine investigation, dTHP-1 macrophages were incubated with Nanotraps containing different phosphatidylserine molar ratios (0%, 5%, 10%, 15%) for 0, 2, 4, 6, 24, or 48 h. The cells were harvested and washed 3 times with PBS at 300×g for 5 min, and stained with Zombie NIR™ Fixable Viability Kit (BioLegend) on ice for 10 min. Then cells were washed with FACS buffer (PBS, 10% FBS, 0.1% NaN3) 2 times and resuspended in 200 µL FACS buffer. Flow cytometry was carried on a BD LSRFortessa™ Flow Cytometer. Live and single cells were gated (Figure S2C) and DiO fluorescence channel was used to indicate the phagocytosis efficiency of different Nanotraps. The data were further analyzed by FlowJo (BD) and Prism (GraphPad) software.

*Lattice light-sheet microcopy imaging analysis of Nanotrap phagocytosis*

For lattice light-sheet imaging, $4\times10^4$ dTHP-1 macrophages were seeded onto each coverslip and DiD-labeled Nanotraps with different phosphatidylserine molar ratios (0%, 10%, and 15%) were added for 24- or 48-h incubation. The cells were washed by PBS for 3 times, fixed with 4% PFA, stained with (5 μg/mL) CF488 Wheat Germ Agglutinin (WGA) Conjugates (Biotium), and washed 3 times with HBSS. Coverslips were imaged by lattice light-sheet microscopy (3i) using z+objective scanning. Imaging was conducted with 488 nm and 647 nm lasers, with dither set to 3 and 20 ms exposures. Z-steps (60) were collected with a 0.4 μm step size. Resulting images were deconvolved as described previously[26,33] using LLSpy (cudaDeconv) used under license from Howard Hughes Medical Institute, Janelia Research Campus. Image reconstruction videos were made in Imaris (Bitplane).

*Confocal Microscopy of Endosomes and Lysosomes*

For confocal imaging, $3 \times 10^4$ dTHP-1 cells were seeded into 8-well chambers and 500 nm 15% PS DiD-labeled Nanotraps were added for 6 h at 37°C. The cells were washed by PBS for 3 times, fixed with 4% PFA, and washed 3 times with PBS. The cells were then stained with (10 μg/mL) anti-LAMP-1-AF488 (BioLegend) and (0.5 μg/mL) anti-EEA1-AF594 (Abcam) for 30 min, then washed 3 times with PBS. 300 nM DAPI was then added for 10 min, then washed 3 times with PBS. Confocal imaging was conducted on a Leica SP8 with a white light laser and 100× oil-immersion objective with 1.5× zoom. Z-stacks were acquired with a z-step of 300 nm. Images were z-projected and despeckled in Fiji. Line scan plot profile was conducted in Fiji.

*Kinetics Assays*

SARS-CoV-2 spike pseudotyped lentivirus was labeled with lipophilic dye DiO[109] for 20 min, fixed with 4% PFA then washed 3 times with PBS in an Amicon Ultra-centrifugal tube (100 kDa). DiD-loaded Nanotraps were prepared and incubated with the DiO labeled pseudotyped lentivirus for various

time points. DiD/DiO double positive events were gated and the mean fluorescence intensity of DiO was recorded by flow cytometry until saturation was achieved.

Macrophages were prepared as described above and incubated with DiO-loaded Nanotraps for varying time points until saturation was achieved. The cells were harvested and washed 3 times with PBS at 300×g for 5 min, and stained with Zombie NIR™ Fixable Viability Kit (BioLegend) on ice for 10 min. Then cells were washed with FACS buffer (PBS, 10% FBS, 0.1% NaN3) 2 times and resuspended in 200 µL FACS buffer. Flow cytometry was carried on a BD LSRFortessa™ Flow Cytometer. Live and single cells were gated and DiO fluorescence channel was used to indicate the phagocytosis efficiency at various time points.

*Enzyme-linked immunosorbent assay (ELISA)*

For the IL-6 ELISA, six conditions were conducted to test macrophage activation: 1) Macrophages alone 2) Macrophages and Nanotraps 3) Macrophages and Epithelial cells 4) Macrophages, Epithelial cells, and Virus 5) Macrophages, Epithelial Cells, and Nanotraps and 6) Macrophages, Epithelial Cells, Virus, and Nanotraps. For all wells, $1\times10^5$ dTHP-1 cells were plated into 12-well plates overnight. The next day, to wells containing epithelial cells, $2\times10^5$ HEK293-ACE2 cells were added. To wells that include Nanotraps, 10 µg/mL Nanotraps were added. To wells that include Nanotraps and virus, 10 µg/mL Nanotraps were added to 500 FFU pseudotyped VSV, incubated for 1 h at 37°C, then added to the cells. Plates were incubated for 24 h, then centrifuged at 300 × g for 5 min and supernatants were harvested. IL-6 ELISA (BioLegend) was conducted according to manufacturer's instructions.

*Production of SARS-CoV-2 spike pseudotyped VSV*

Packaging cells (HEK293T) in serum-free DMEM were transfected with 9 µg pCAGGS SARS-CoV-2 spike expression plasmid using polyethylenimine (PEI). After 24 h, $3\times10^7$ FFU VSVdG*G-GFP virus was added to the HEK293T cells and incubated for another 48 h. Media were collected and spun at

500×g for 3 min to remove cell debris, then passed through a 0.45 μm pore filter. The virus was then stored in -80°C. To check the infection rate, HEK293T-ACE2 cells (Integral Cat# C-HA102) were incubated with the final VSVdG-GFP*CoV2 pseudovirus and visualized by the presence of GFP positive cells through direct microscopic imaging or flow cytometry.

*SARS-CoV-2 pseudovirus neutralizing assay*

For SARS-CoV-2 spike pseudotyped VSV neutralizing assay, $4\times10^4$ HEK293T-ACE2 cells (maintained in DMEM supplemented with 10% FBS and 1% Penicillin-Streptomycin) were seeded in a 96-well plate overnight. Different concentrations of ACE2 proteins or Nanotraps (containing 0.2, 0.4, 0.6, 0.8, 1.0, 1.5, 2.0, 3.0, 6.0, 9.0, 12 μg/mL ACE2) were incubated with 500 FFU SARS-CoV-2 spike pseudotyped VSV for 1 h in 37 °C. The virus-Nanotrap solution was added into the HEK293T-ACE2 cells and incubated for 24 h (n=3 for each group). The cells were imaged with a fluorescence microscope (Nikon) using 10×/0.30 NA objective. The excitation wavelengths were 470 ± 25 nm (Spectra X, Lumencor). The emissions of GFP were captured by an Andor iXon Ultra 888 back-illuminated EMCCD camera (Oxford Instruments). The number of GFP-positive cells were counted manually by objective three times. The viral infection rates were calculated as the ratio of GFP-positive cells in the group incubated to that of the group incubated with virus alone.

For SARS-CoV-2 spike pseudotyped lentivirus neutralizing assay, $1\times10^4$ HEK293T-ACE2 cells were seeded onto a 384-well plate overnight. Nanotraps or ACE2 was added to SARS-CoV-2 pseudovirus (4 μL per well) and incubated for 1 h at 37°C. The virus-Nanotrap solution was added to each well (n = 3 for each group). 72 h later, the plate was centrifuged for 5 min at 500×g to prevent cell loss. Supernatant was aspirated and 35 μL of PBS was added. PBS was carefully aspirated, leaving ~15 μL of liquid behind. Renilla-Glo assay substrate was added to the Assay Buffer at a 1:100 dilution, then 15 μL of the substrate:buffer was added to each well of a 384-well plate. The bioluminescence was recorded by a

microplate reader (Fisher Scientific BioTek Cytation 5) with an exposure of 200 ms. Wells infected with pseudovirus only were normalized as 100%.

*Co-culture assay*

THP-1 cells were differentiated into macrophages as described above. Coculture was carried out in a macrophage to A549 cell ratio of 1:5. $4\times10^4$ A549 cells were seeded in an 18-well microslide (Vivid) overnight and $8\times10^3$ dTHP-1 macrophages were added onto the A549 cells for another 6 h. 500 FFU SARS-CoV-2 spike pseudotyped VSV was incubated with Nanotraps or PBS in 37 °C for 1 h before adding to the coculture cells. 24 h later, the cells were fixed with 4% PFA and stained with CF532 Wheat Germ Agglutinin (WGA) Conjugates (Biotium) and DAPI and imaged under a confocal microscope (Leica SP8). Percent infectivity was quantified in FIJI by dividing GFP+ cells by total cell number (DAPI-stained nuclei). Each channel was processed as follows: Image>Threshold ("Huang" preset[110]); Image>Binary>Fill Holes; Image>Binary>Watershed; Analyze>Count Particles.

*In vitro cytotoxicity assay*

A549 or HEK293T-ACE2 cells (both maintained in DMEM supplemented with 10% FBS and 1% Penicillin-Streptomycin) were seed in a 96-well plate at a density of $1\times10^4$ cells/well in 100 μL of culture medium overnight. Nanotraps ($3.8\times10^7$ particles/mL) were added into cells and the cells were cultured in a CO2 incubator at 37°C for 72 h. 10 μL of CCK-8 (MedChem Express) solution was added to each well of the plate. The plate was incubated for 2 h in the incubator. Then it was put into a microplate reader (Fisher Scientific BioTek Cytation 5) and the plate was gently shaken for 1 min before measuring the absorbance at 450 nm. The cytotoxicity was calculated by cell viability, that the relative absorbance from the control wells without Nanotraps were normalized as 100%. The Nanotrap concentrations (particles/mL) were manually counted by a hemocytometer. Briefly, the freshly prepared Nanotraps were vortexed and diluted in PBS in 1 to 1000 dilution. 10 μl of the diluted solution was further mixed with 10 μl Trypan blue for

enhanced contrast, and added onto the hemocytometer, then the number of the Nanotraps were counted under a microscope.

*In vivo biosafety assays*

C57BL/6NHsd mice at the age of 6 weeks were purchased from Envigo and maintained at the Animal Facility of the University of Chicago. The animal study protocols were approved by the Institutional Animal Care and Use Committee (IACUC) of University of Chicago. To evaluate the safety of the Nanotraps, 2 male and 2 female 6-10-week-old C57BL/6NHsd mice were intratracheally administered with 10 mg/kg Nanotrap-ACE2 in 50 μL PBS. Blood samples were collected by submandibular vein via cheek punch using a commercially available 4 mm point lancet after three days. A small aliquot of approximately 100 μL blood was collected into EDTA-containing heparinized tubes, and red blood cells, white blood cells, and platelets were counted by a Hematology Analyzer (Beckman Coulter Act Diff 5 CP) according to the manufacturer's instructions. For the comprehensive chemistry panels, blood was allowed to coagulate in 4 °C for 2 h, and serum was collected after centrifugation (1,000×g for 15 min) for analysis. Serum alkaline phosphatase, alanine aminotransferase, amylase, urea nitrogen, calcium, cholesterol, glucose, total bilirubin, total proteins were determined by a Vet Axcel blood chemistry analyzer (Alfa Wasserman). Lungs, heart, liver, spleen, and kidney were collected from the same mice, fixed in 10% formalin for 24 h, embedded in paraffin. The resulting blocks were cut in 5 μm sections and further stained with hematoxylin and eosin (H&E) by the University of Chicago Human Tissue Research Center. Fluorescent imaging samples were collected in Tissue-Tek® O.C.T. Compound on dried ice and stored in -80 °C before cryosectioning on a cryostat (Leica). The obtained 10 μm thick tissue slides were then further stained with DAPI. The histology and fluorescence slides were scanned by a CRi Pannoramic MIDI 20× whole slide scanner and analyzed on the QuPath software.

*Ex vivo lung perfusion assay*

Non-transplantable human lungs were obtained from deceased individuals provided by the organ procurement organization Gift of Hope. All specimens and data were de-identified prior to receipt. This study was deemed exempt by the University of Chicago Institutional Review Board (IRB19-1942).

Lung Harvest: Lungs unsuitable for transplantation were harvested in standard clinical fashion72 from deceased patients. Figure 5A shows the lung of a 56-year-old male patient (87.2 kg, cause of death: brain death). Lungs were transported to the laboratory at 4°C.

Lung inoculation: Tissue samples were collected from the edge of the right upper lobe before perfusion as an untreated control; 500 μL SARS-CoV-2 spike pseudotyped lentivirus (Intergral Molecular, RVP 701) was resuspended in 5 mL PBS and injected into the lingula of the left lung; 500 μL SARS-CoV-2 spike pseudotyped lentivirus was first incubated with Nanotrap-Antibody carrying 250 μg neutralizing antibody for 1 h at 37 °C before inoculation. This mixture was then injected into the right middle lobe. Tissue samples at all three sites were collected. Some samples were immersed in MACS buffer for tissue dissociation, and other samples were fixed in 4% PFA, sliced with thickness of 5 μm and stained for H&E.

Lung perfusion: The lung bloc was perfused according to published techniques[111,112]. A centrifugal pump was used to perfuse the pulmonary artery with deoxygenated cellular perfusate (1×Dulbecco's Modified Eagle Medium containing 4.5g/K D-glucose, L-glutamine and 110 mg/L of sodium pyruvate, with addition of 5% bovine serum albumin and 2 units of packed red blood cells). The left atrium was left open for gravity drainage. The trachea was incubated and the lung was ventilated with volume control ventilation (tidal volume set at 6-8 mL/weight of ideal body weight (kg) of donor, respiratory rate of 8-13, and fraction of inspired oxygen set at 21%). Sweep gas composed of 8% CO2, 3% O2, 89% N2 was connected to the hollow-fiber de-oxygenator heat exchanger to remove oxygen and add in CO2 into the perfusate returning back to the lung. After initiation of perfusion with gradual warming and increasing pump flow over 30 min, the lung bloc was maintained at 37°C with pump flow calibrated to pulmonary artery pressure of 10 – 20 mmHg for 8 h.

Sampling: Perfusate was sampled at serial time points from the pulmonary artery and left atrium. Differences in oxygen content between perfusate samples were used to calculate the oxygenation capacity of the lung. Airway pressure was measured periodically to calculate lung compliance based on tidal volume. Tissue samples were collected from treated and untreated lobes of the lung at time 0 and time 8 h of perfusion.

Sample Processing: After 8 h perfusion, tissues were harvested as described above. Tissue dissociation was performed by mechanical digestion in DMEM media treated with 2.5 U/mL DNase (company); samples were passed through 70 μm cell strainers (Fisher Scientific). Red blood cells were lysed in 10 mL RBC lysis buffer (Life Technologies), washed 3 times in DMEM (300×g for 3 min), and resuspended in 10 mL DMEM. Cells were counted with a hemocytometer and immediately used for luciferase assay or cryopreserved in Cell Banker medium (Amsbio) at a density of $4\times10^6$ cells/mL.

Samples that were not dissociated were fixed in 4% PFA and sliced with thickness of 5 μm. Some samples were stained for H&E and imaged on a CRi Pannoramic MIDI 20× whole slide scanner. Tissue slides used for RBC quantification were stained for DAPI and imaged on a CRi Pannoramic MIDI 20× whole slide scanner with 488-nm and 560-nm lasers. Both channels were quantified in Fiji as follows: Image>Threshold ("Otsu" preset); Image>Binary>Fill Holes; Analyze>Measure.

For luciferase assay, the cells harvested as described above were washed with PBS (300×g for 3 min) 3 times. Then $2\times10^4$ cells were seeded into 96-well plate. Renilla-Glo Assay Substrate was added to the Assay Buffer at a 1:100 dilution, then 30 μL of the Substrate Buffer was added to each well for 10 min. The bioluminescence from each well was detected by a microplate reader (Fisher Scientific BioTek Cytation 5) with an exposure of 200 ms.

Primary cells harvested from the untreated right superior lobe of the human lung were further used for infection analyses. Briefly, $2\times10^4$ primary lung cells were seeded onto a 384-well plate. 25 μL Nanotraps-Antibody (6.08×107 particles/mL) was added to 20 μL SARS-CoV-2 spike pseudotyped

lentivirus (Intergral Molecular, RVP 701) per well and incubated for 1 h at 37°C before adding to the cells. For virus only group, 10 μL SARS-CoV-2 spike pseudotyped lentivirus was added to the cells. 48 h later, the plate was centrifuged for 5 min at 500×g to prevent cell loss. Supernatant was aspirated and 35 μL PBS was added. PBS was carefully aspirated, leaving ~15 μL of liquid behind. Renilla-Glo Assay Substrate was added to the Assay Buffer at a 1:100 dilution, then 15 μL of the Substrate:Buffer was added to each well of a 384-well plate. The bioluminescence was recorded by a microplate reader (Fisher Scientific BioTek Cytation 5) with an exposure of 200 ms. The infectivity was calculated by the relative luminescence intensity: wells infected with SARS-CoV-2 pseudovirus only were normalized as 100%.

*Authentic SARS-CoV-2 Neutralizing Assay*

All SARS-CoV-2 infections were performed in biosafety level 3 conditions at the University of Chicago Howard T. Ricketts Regional Biocontainment Laboratory. African green monkey kidney (Vero E6) cells were maintained in DMEM supplemented with 10% FBS and 1% Penicillin-Streptomycin. Nanotraps or neutralizing antibodies were serially diluted 2-fold and mixed with 400 PFU of SARS-CoV-2 (nCoV/Washington/1/2020, kindly provided by the National Biocontainment Laboratory, Galveston, TX) for 1 h at 37ºC, then used to infect Vero E6 cells for three days. Cells were fixed with 3.7% formalin and stained with 0.25% crystal violet. Crystal violet-stained cells were then quantified by absorbance at (595 nm) with a Tecan m200 microplate reader. Cell survival was calculated by normalizing untreated cells to 100%.

# CHAPTER 3: LATTICE LIGHT-SHEET MICROSCOPY MULTI-DIMENSIONAL ANALYSES (LaMDA)

**NOTE:**

The following section (Chapter 3) is copied (with the exception of figure numbers, section titles, and reference numbers) from my co-first authored publication "Lattice Light-Sheet Microscopy Multi-Dimensional Analyses (LaMDA) of T-Cell Receptor Dynamics Predict T-Cell Signaling States"[33], which was published in Cell Systems on May 20, 2020 under the Creative Commons CC-BY-NC-ND license (https://creativecommons.org/licenses/).

**AUTHORS:**

Jillian Rosenberg*, Guoshuai Cao*, Fernanda Borja-Prieto, Jun Huang

*These authors contributed equally

**AUTHOR CONTRIBUTION**

Conceptualization, J.R. and J.H. with input from G.C.; Methodology, J.R. and F.B.-P. with input from J.H. and G.C.; Formal Analysis G.C. with input from J.R. and J.H.; Writing, J.R., G.C., and J.H.; Supervision, J.H.

## INTRODUCTION

Lattice light-sheet microscopy (LLSM) is a recently developed microscopy technique that allows for 4D (x, y, z, and time) imaging with exceptionally high temporal resolution (~10 ms/frame, ~1 s/1 cell volume) and minimal photobleaching[25]. LLSM provides high-dimensional, high-spatiotemporal resolution imaging data of cell surface receptors or receptor microclusters (≥ 1,000) over a long duration of time (≥ 4 mins) on the entire 3D surface of live primary cells. As a result of these capabilities, LLSM and other cutting-edge microscopy techniques generate larger and more complex high dimensional data. These data are often underutilized due to a lack of comprehensive and efficient high-dimensional analysis pipelines that are accessible to the general user. The lack of such an analysis pipeline represents a key limitation in the use of imaging systems, including LLSM, that generate big data and are crucial to answering biological questions at the single-molecule level.

In this chapter, I introduce Lattice light-sheet microscopy Multi-Dimensional Analyses (LaMDA), a pipeline to apply big data analysis techniques to high-dimensional LLSM data. LaMDA provides a complete end-to-end pipeline from upstream data collection and feature engineering to downstream machine learning and dimensionality reduction analyses. We intentionally constructed LaMDA using publicly-available packages to enable easy adaptation and incorporation by general users to facilitate broad application across all areas of cell biology. Moreover, it was designed to motivate a paradigm shift wherein, rather than focusing on the cell as the unit of study, we focus on a molecular unit. The LaMDA pipeline supersedes the need for high-throughput collection of single-cell time-lapse data, which is difficult to capture using LLSM, by enabling extraction of sufficient molecular content for the use of high-dimensional analyses.

We applied LaMDA to image and analyze the dynamics of T-cell receptors (TCR) microclusters on the primary T-cell surface with high dimensionality to understand T-cell signaling states. T cells play a central role in adaptive immunity by mediating immune responses against cancer and infection[58,113,114]. As the dominant receptor, TCRs govern the recognition, activation, differentiation, and function of T cells in

health and disease[115–117]. Thus, we applied LaMDA to study TCR clusters in order to determine whether T cell signaling states could be deciphered by simply analyzing the structure and dynamics.

## RESULTS

### *LaMDA Pipeline*

LaMDA was designed to enable big data analysis of high-dimensional LLSM data (Fig. 2). To begin using LaMDA, LLSM is employed to capture single-cell images in four dimensions (x, y, z, and time) with high spatiotemporal resolution (~1 s/cell volume, x and y resolution ~200 nm, and z-step 400 nm) (Fig. 2A, Movie 1). Then, advanced imaging software, such as Imaris, is utilized to track thousands of surface receptor microclusters (or other structures) from individual cells (Fig. 2B) and extract multiple (36 in this study) statistical parameters for each tracked object simultaneously (Fig. 2C). Due to the large size of collected data sets, machine learning and dimensionality reduction methods can be incorporated for analysis (Fig. 2D-E). For example, a machine learning-based classifier[118] could be built to learn the inherently subtle yet very complex differences between the tracked receptors of two or more known cellular conditions. This classifier could then be used to predict the state of the receptor microclusters in new or less-understood cellular conditions (Fig. 2F). Furthermore, feature importance metrics from the classifier can inform on the underlying biological differences in the system (Fig. 2G). Once the classifier metrics are used to select important features, they can be studied individually by building statistical models. To understand if multiple parameters are working together to drive biological differences, dimensionality-reduction techniques, such as uniform manifold approximation and projection (UMAP)[102] and diffusion maps[103,119], could be applied in parallel (Fig. 2D-E) to graphically emphasize three important points: (1) these techniques cluster objects into several groups representative of different physical states; (2) the relative locations of these object states inform us on their relationships, indicating directionality and identifying the properties that change with that direction (Fig. 2H); and (3) the local density at each coordinate on these dimensionality-reduction maps can be further transformed into a pseudo-energy surface to show relative stability of each object (Fig. 2I).

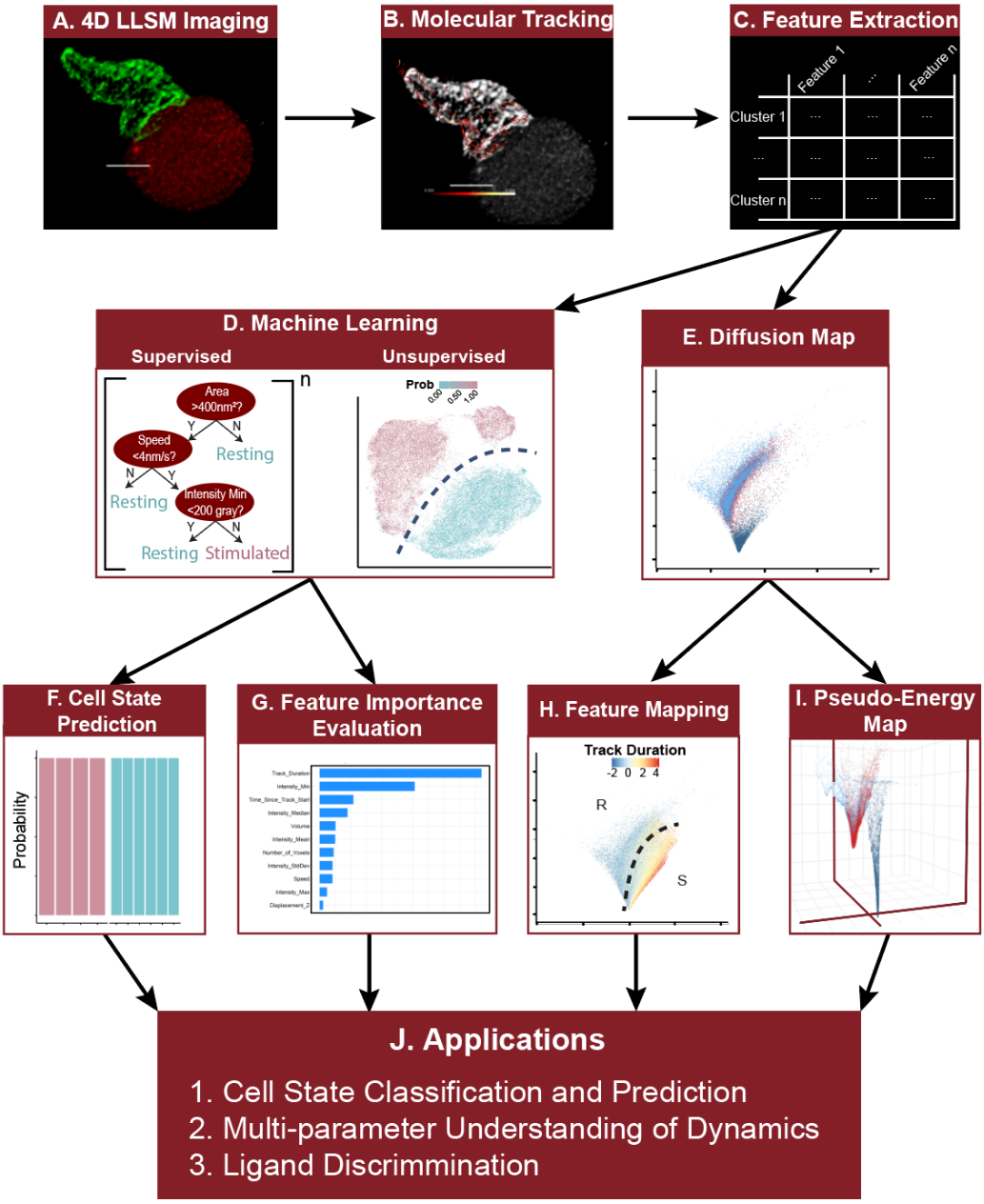


**Figure 2: LaMDA Pipeline** (**A**) Four-Dimensional (4D) imaging is conducted with LLSM. Receptors (green) on a cell are fluorescently labeled and 4D images are collected. Scale bar represents 5 µm. (**B**) After deconvolution and debleaching, receptor microclusters are tracked with Imaris software. Scale bar represents 5 µm. (**C**) Microcluster features are extracted from tracked TCR microclusters. (**D**) Machine learning is conducted on extracted features for prediction. (Left) To classify between different cell states, supervised XGboost decision tree ensembles are trained as a binary classifier then tested and validated. (Right) Unsupervised UMAP clustering is used to independently validate the XGboost binary classifier. The XGboost binary classifier is used to predict the states of cells. (**E**) Diffusion maps are used as a dimensionality reduction technique to further quantify variations among cell states. The diffusion map is built from features selected based on their importance. (**F**) The XGboost classifier is utilized to provide cell state predictions based on TCR microcluster features. (**G**) The importance of each feature in the XGboost classifier is evaluated using SHapley Additive exPlanations (SHAP), and the top feature is individually analyzed using appropriate statistical modeling. (**H**) Diffusion map is colored by normalized features (e.g. track duration shown here). Dotted line indicates approximate divide between resting and stimulated cells. This figure is reproduced from Rosenberg, et al., *Cell Systems* 2020.

Together, LaMDA uses high dimensional imaging and big data analyses to discover differentiating properties between cellular phenotypes and to reveal and predict underlying cellular states (Fig. 2J).

*LaMDA Shows TCR Microclusters Reflect T-Cell Activation State (Resting versus Stimulated), Not the Functional Phenotype (Naïve versus Blasting)*

As a proof of concept of the LaMDA pipeline, we investigated the dynamics of TCRs, one of the most critical molecules in adaptive immunity and their relationship to T-cell activation. TCRs specifically recognize rare agonist peptide-MHCs (pMHCs) among numerous self-pMHCs on the surface of the cell being surveyed to trigger adaptive immune responses and therefore are essential molecules to combat infection and cancer[120,121]. TCRs are known to form microclusters on the surface of the T cell and represent a key mechanism toward understanding T-cell signaling and function[63,90,122–135].

To visualize the 4D TCR microcluster dynamics by LLSM, we either fused a green fluorescent protein (GFP) to the C-terminus of the CD3ζ chain of the TCRs or used an Alexa Fluor 488 (AF488)-conjugated anti-TCRβ Fab to fluorescently label the TCRs at the membrane of live primary 5C.C7 $CD4^+$ T cells. Cytosolic mCherry-transduced CH27 cells were used as the antigen-presenting cells. After fluorescent labeling of TCRs on T cells and loading agonist moth cytochrome C (MCC) peptide onto the antigen presenting cells, both the T cells and antigen presenting cells were added to the LLSM imaging chamber for 4D imaging using 488-nm and 561-nm lasers. We recorded videos (4-6 min) of TCR microclusters across the entire 3D cell surface (x and y resolution ~200 nm, z-step 400 nm, ~1 s/cell volume; Fig. 3A-D, Fig. 16A-G, Movies 1-6, 8) for four T cell states: resting naïve, naïve stimulated by antigen presenting cells, resting blasting, and blasting stimulated by antigen presenting cells (Fig. 3E). We then tracked ~10,000 individual TCR microclusters on each T cell, measuring 36 parameters (including speed, direction, volume, intensity, area, location, and track duration; see Methods for details) for each microcluster across the videos (Fig. 3B and 3D, Fig. 16K, Movie 7). The data were pre-processed and an Extreme Gradient Boosted (XGboost) Decision Tree Ensemble[118] with logistic loss was built on 19 of these parameters (Fig. 3F and

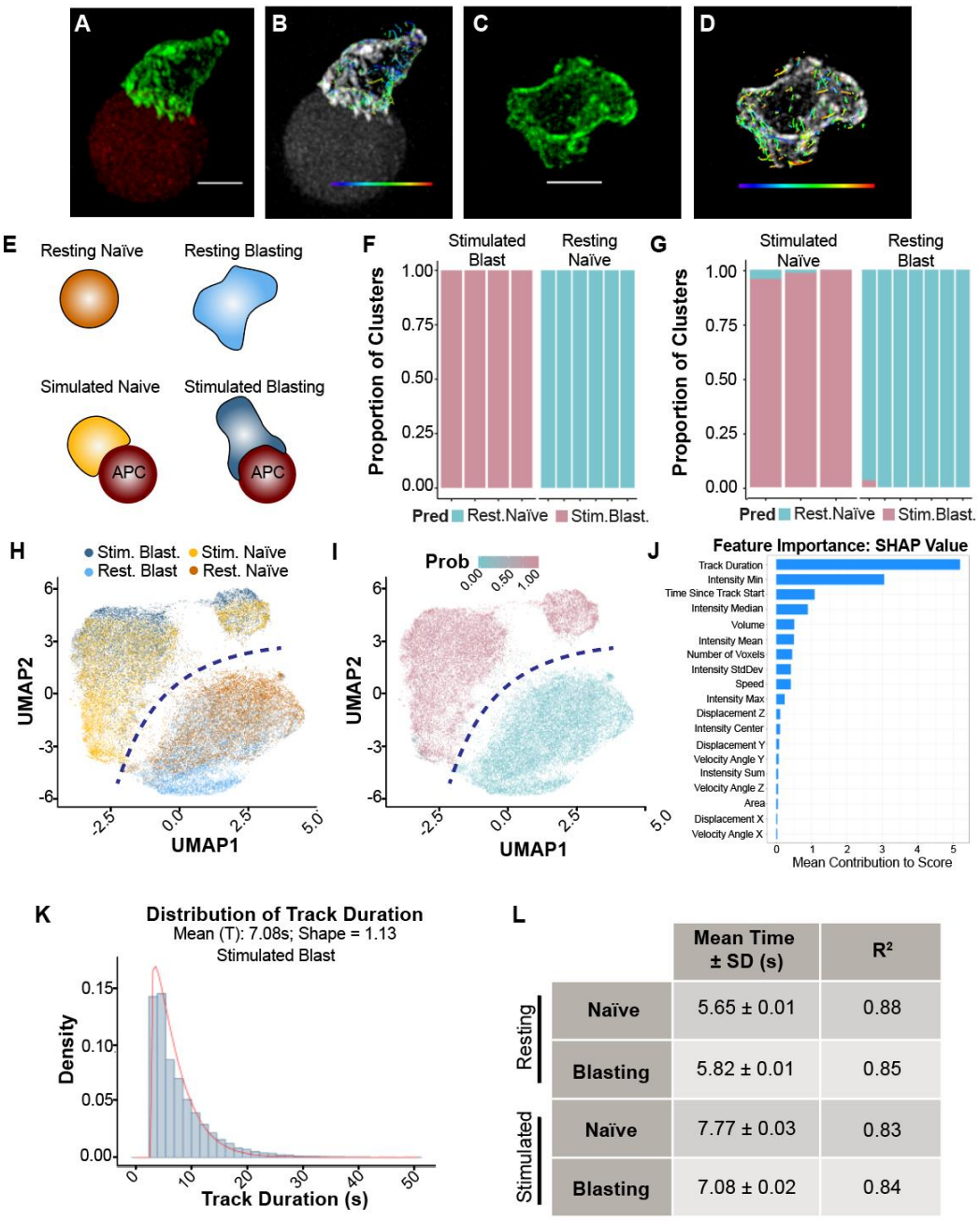


| | | Mean Time ± SD (s) | $R^2$ |
|---|---|---|---|
| Resting | Naïve | 5.65 ± 0.01 | 0.88 |
| | Blasting | 5.82 ± 0.01 | 0.85 |
| Stimulated | Naïve | 7.77 ± 0.03 | 0.83 |
| | Blasting | 7.08 ± 0.02 | 0.84 |

**Figure 3: XGboost binary classifier differentiates between T-cell signaling states.** (**A**) Three-dimensional rendering of a blasting CD4$^+$ T cell stably transduced with CD3ζ-GFP (green) as it encounters a CH27 cell stably transduced with cytosolic mCherry (red). See also Supplemental Movie 1. (**B**) Dragon tails showing particle positions over the previous eight frames overlaid onto (A). Color bar represents Velocity Angle X from 0° (purple) to 180° (red). (**C**) Three-dimensional rendering of a blasting resting CD4$^+$ T cell stably transduced with CD3ζ-GFP (green). See also Supplemental Movie 2. (**D**) Dragon tails showing particle positions over the previous eight frames overlaid onto (C). Color bar represents Velocity Angle X from 0° (purple) to 180° (red). (**E**) Diagram depicting the four cell states, resting naïve, resting blasting, stimulated naïve, and stimulated blasting, graphically. (**F**) XGboost training results. Each bar represents an independent cell (Resting Naïve cells n = 58,784 microclusters; Stimulated Blasting cells n = 97,237 microclusters), Pred = prediction. See also Figure S1K for number of microclusters in each cell. (**G**) XGboost testing results. Each bar represents an independent cell (Stimulated Naïve cells n = 38,809 microclusters; Resting Blasting cells, n = 60,116 microclusters), Pred = prediction. See also Figure S1K for number of microclusters in each cell. This figure is reproduced from Rosenberg, et al., *Cell Systems* 2020.

Fig. 16H-K, referred to henceforth as the XGboost classifier) to classify TCR microclusters as microclusters from resting T cells or stimulated T cells. To avoid strong correlation within the same cells, and to prevent the confounding effect of "past stimulation" (i.e., naïve vs. blast), the XGboost classifier was first trained on microclusters from stimulated blast cells and resting naïve cells (Fig. 3F). The classifier was later tested on stimulated naïve cells and resting blast cells (Fig. 3G). Within the training set, a train-validate-test approach was utilized to avoid overfitting (See Methods, Fig. 16I). The XGboost classifier consists of 150 decision trees, each of which selects up to three parameters to fit a logistic regression model. The weighted values from all 150 trees are used to classify each microcluster (Fig. 16H).

This classifier allows us to identify which observable features of TCR dynamics can function as signatures of a cell's state and allows for classification. For example, we hypothesized that because TCR microclusters behave differently in response to a stimulation (e.g., TCR-pMHC interaction)[90,124,126,128] , TCR microclusters switch from a "resting state" into a "stimulated state" and thus could be differentiated by machine learning. Indeed, in the internal test, the XGboost classifier could precisely differentiate between TCR microclusters on the resting naïve T cell from those on a stimulated blasting T cell with a validation accuracy of 100% and an internal test accuracy of 99.96% (Fig. 3F). This suggests that our machine learning model can reliably predict the cell state, that is resting naïve vs. stimulated blasting, by TCR microcluster dynamics alone. Accordingly, when a similar analysis was performed on two other T cell states, stimulated naïve and resting blasting, we found large differences between TCR microcluster dynamics on stimulated and resting T cells, which allowed for accurate discrimination based on cell state by XGboost (Fig. 3G). These results demonstrate that TCR microcluster dynamics are sufficient to predict cell state. Notably, however, the prediction of cell state is irrespective of prior antigen experience; the XGboost classifier could not distinguish between naïve and blasting T cells (Fig. 3F-G). These results demonstrate that machine learning can precisely predict T-cell signaling states (resting state vs. stimulated state) using surface TCR dynamics, but that from the perspective of the TCR dynamics, naïve and blasting T cells are indistinguishable. This observation is not unique to the XGboost classifier. TCR microclusters

can also be segregated into two groups, resting state TCR microclusters and stimulated state TCR microclusters, using the dimensionality reduction method, UMAP[102] (Fig. 3H-I, decision boundary in blue and Fig. 17A).

Since the dynamic features of TCR microclusters represent a direct reflection of the T-cell signaling states, we next sought to use big data analysis techniques to investigate which biological features contributed to the observed differences. To further understand the features predicted by the XGboost classifier, we plotted the SHapley Additive exPlanations (SHAP) values[136,137] and found that track duration (i.e., the length of time a microcluster could be detected on the cell surface) was the most important feature (Fig. 3J and Fig. 17B). While large SHAP values only directly indicate the features most informative to the decision trees, these features are often biologically relevant. Thus, we plotted the distribution of track duration for resting naïve, stimulated naive, resting blasting, and stimulated blasting T cells and fitted three-parameter Weibull distribution models, a commonly used model for lifetime analyses[101] (Fig. 3K, Fig. 17C-F). The mean duration "T" was derived from the Weibull distributions (See Methods) and describes the average lifetime of TCR microclusters on the surface of a T cell. We determined that antigen stimulation increased the mean duration of TCR microclusters significantly when compared to resting state, for both naïve and blasting T cells (Fig. 3L and Fig. 17F). This implies a signaling pathway was initiated to alter global control of TCR microclusters on the surface.

Next, we characterized TCR microcluster dynamics using diffusion maps, a nonlinear dimensionality reduction technique that focuses on identifying the underlying manifold of the data and reveals diffusion-like behavior between different states[103,119]. We sampled 8,000 microclusters from each cell group and chose a subset of 7 selected features (mean intensity, minimum intensity, intensity sum over the surface, area, volume, speed, and track duration) based on the XGboost classifier feature importance (as previously shown in Fig. 3J) and their mutual independence (See Methods). This diffusion map allowed us to graphically compare resting-state TCRs with stimulated-state TCRs (Fig. 4A). We next estimated the local density of TCR microclusters on the diffusion map (Fig. 4B) and derived the 3D pseudo-free energy

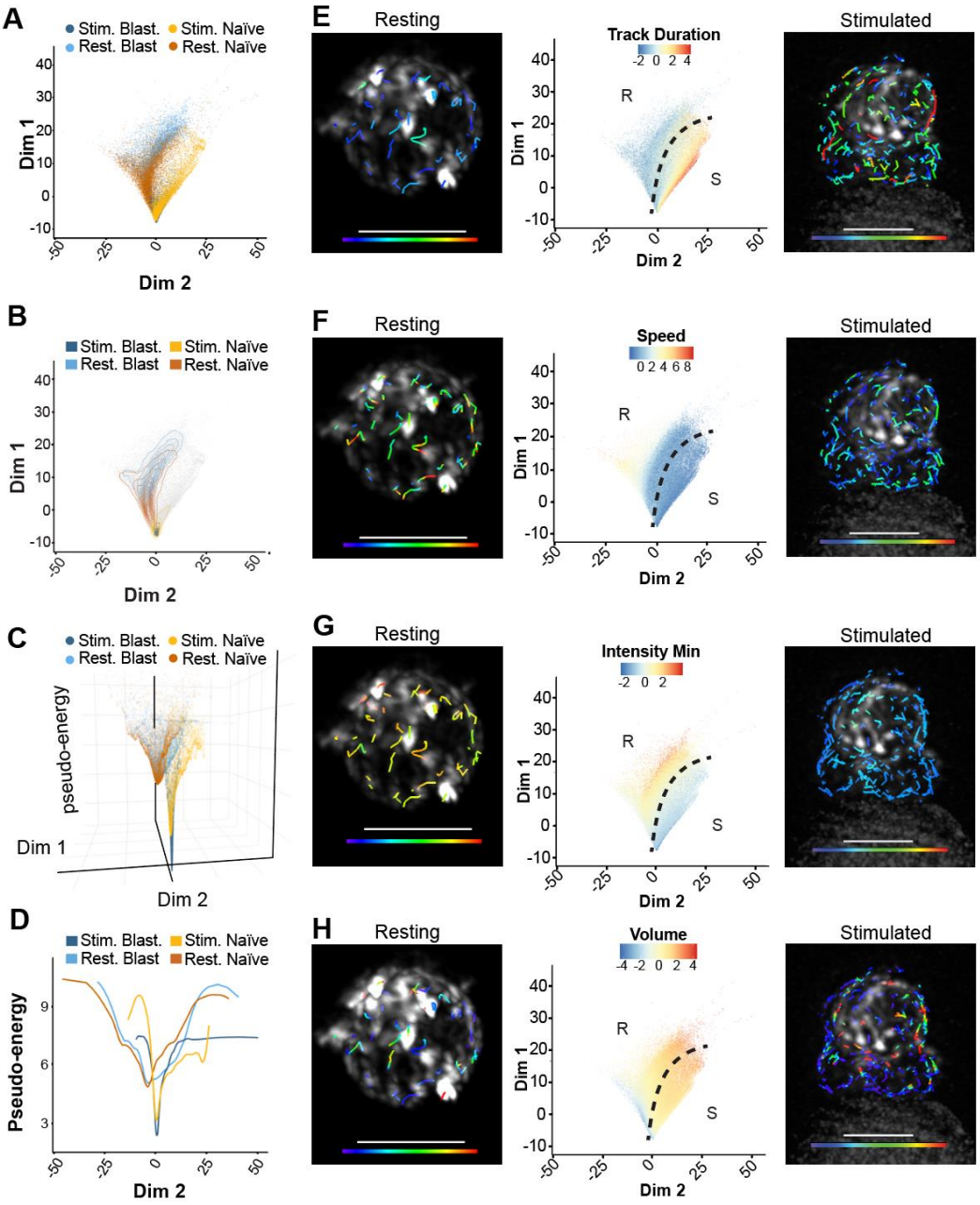


**Figure 4: Diffusion maps differentiate between T-cell signaling states.** (**A**) Diffusion map built from 7 selected features. Colors indicate cell group. (**B**) Density map created by estimating local density on the diffusion map (A). Colors indicate cell group. (**C**) Pseudo-energy map created from density map (B). Colors indicate cell group. (**D**) Projection of pseudo-energy map (C) along dimension 2. Colors indicate cell group. (**E-H**) Left: Resting naïve cell from Figure 16A overlaid with dragon tails showing particle positions over the previous eight frames are color coded to show particle track duration from 0 s (purple) to 25 s (red) (**E**), particle speed from 0.0 μm/s (purple) to 0.5 μm/s (red) (**F**), particle intensity minimum from 0 AU (purple) to 500 AU (red) (**G**), or particle volume from 0.0 $\mu m^2$ (purple) to 0.2 $\mu m^2$ (red) (**H**). Center: Diffusion map from Figure 4A colored by normalized track duration (**E**), speed (**F**), intensity minimum (**G**), or volume (**H**). Approximate boundary line between resting and stimulated cells (see also Fig. 4A) represented in black. Right: Stimulated blasting cell from Figure 16D overlaid with dragon tails showing particle positions over the previous eight frames are color coded to show particle track duration from 0 s (purple) to 25 s (red) (**E**), particle speed from 0.0 μm/s (purple) to 0.5 μm/s (red) (**F**), particle intensity minimum from 0 AU (purple) to 500 AU (red) (**G**), or particle volume from 0.0 $\mu m^2$ (purple) to 0.2 $\mu m^2$ (red) (**H**). This figure is reproduced from Rosenberg, et al., *Cell Systems* 2020.

surface (See Methods) by adapting a method commonly used in molecular simulation research[119] Fig. 4C). For easy visualization and comparison, these 3D energy wells were projected along dimension 2 to become 2D energy wells (Fig. 4D). Assuming all other terms that contribute to energy are held constant, the depth of the energy well directly revealed the stability of the TCR microclusters on each cell (Fig. 4D).

We found the stimulated-state TCR microclusters occupy a much deeper energy well than the resting-state TCR microclusters, on both blasting and naïve T-cell surfaces (Fig. 4D), demonstrating that, assuming all other terms that contribute to energy are held constant, TCR stimulation stabilizes TCR microclusters on the cell surface. We also analyzed the diffusion maps to compare individual dynamic features between resting and stimulated TCR microclusters (Fig. 4E-H, middle panel). For track duration, we found clear separation between resting-state and stimulated-state TCR microclusters in the diffusion map (Fig. 4E). Similar distinctions between resting-state and stimulated-state TCR microclusters were found for speed (Fig. 4F) and minimum intensity (Fig. 4G), whereas the differences in volume (Fig. 4H) were less obvious. These analyses reinforced the reliability of our machine learning prediction. Spatially, we observed that the longest lasting microclusters (red) are not localized to the synapse as would be expected due to the TCR-pMHC bonds, but rather are dispersed throughout the whole cell (Fig. 4E, right panel); similar global distributions were found for speed, minimum intensity, and volume (Fig. 4F-H, right panels), indicating that T-cell activation is a global event.

## CONCLUSIONS

We developed a modular pipeline, LaMDA, that combines high resolution 4D LLSM data with machine learning and dimensionality reduction techniques to analyze TCR microcluster dynamics and predict T-cell signaling states. In contrast to many studies that emphasize differences between naïve and blasting T cells, our LaMDA pipeline identified that the dynamics and distribution of TCR microclusters were primarily determined by the T-cell activation state (resting vs. stimulated), rather than by prior antigen exposure (naïve vs. blasting) (Fig. 3 and 4).

LLSM has been widely used across many biological fields to address a variety of questions[25,27,30,32,34,36,37,138–143] . While LLSM has revealed important insights, current analysis approaches are not capable of considering all of the collected data to maximize the biological understanding or conclusions that could be drawn from the data. Most analysis approaches employed for investigating cell biology primarily focus on single features such as intensity, colocalization, autocorrelation, diffusion rates, resolution, or directional analyses[144,145] . The LaMDA pipeline is able to take full advantage of the 4D (x, y, z, and time) data intrinsically provided by LLSM and utilizes it in a myriad of advanced high-dimensional analysis tools, such as dimensionality reduction techniques and machine learning. However, LLSM is a low-throughput method regarding cell number, and if each cell is treated as a single data point, sufficient numbers for high-dimensional analysis methods cannot be reached. Thus, by considering individual molecules (e.g., TCRs) on the cell surface as opposed to single cells captured by LLSM, we are able provide sufficient data points in a high-throughput manner to utilize these methods. By enacting the paradigm shift from single-cell to single-molecule in LLSM, the utility of data produced can be maximized.

In addition to surface molecules, this pipeline can still be used to track intracellular or recycling molecules. The analysis pipeline presented here could simply be used to address different questions. For example, LLSM has already been used to image and track T-cell granzymes, which are cell-death inducing molecules packaged in intracellular vesicles and delivered to the surface of a target cell[140]. Our analysis pipeline therefore could analyze the tracks of these vesicles and address trafficking rates or directions. While any molecular label can be easily implemented, a large number of fluorescently-detectable molecular units must exist in the biological system, highlighting an important consideration in implementing LaMDA for other studies.

Finally, LaMDA was intentionally designed to utilize existing tools and algorithms to perform complex multi-dimensional analysis, thereby enabling easy accessibility for any biologist without the need for familiarity with data science techniques. Moreover, while we used Imaris for feature extraction and an XGboost classifier for machine learning, this pipeline is highly modular and can be adapted for a variety of

biological systems by incorporating alternative algorithms. Other machine learning techniques with different algorithms (e.g., XGboost or supportive vector machine), architectures (e.g., decision trees or neural network) or tasks (e.g., classification, segmentation, or detection) can be incorporated to substitute the XGboost classifier. In addition, multiple dimensionality reduction techniques are applicable (e.g., tSNE, PCA, etc.), and should be chosen based on desired purpose. Similarly, features do not have to be pre-defined and extracted from a software such as Imaris; rather, researchers could engineer context-specific features useful to their own research questions. Therefore, we anticipate broad usage of LaMDA to maximize biological understanding from LLSM data.

# CHAPTER 4: LaMDA REVEALS SIGNALING STATES AND LIGAND DISCRIMINATION

## INTRODUCTION

Having shown in Chapter 3 that we were able to discern T-cell signaling states simply by analyzing the structure and dynamics of TCR clusters, we sought to perturb signaling states to determine whether our method still stands. As described in Chapter 1, TCR stimulation can only fully activate a T cell in the presence of co-receptor CD4 and co-stimulatory molecule CD28 signaling. Co-receptor CD4 is a monomeric polypeptide that plays an important role in augmenting TCR signaling through associated tyrosine kinase Lck[144,146,147]. Early studies have found that CD4 enhances the TCR signaling by 30 to 300-fold[116,148]. In addition, CD4 is the target for viral entry of HIV, and its blockade is in clinical trials as an HIV therapy[125]. Concomitantly, co-stimulatory receptor CD28 is required to fully activate T cells without causing apoptosis[149–151]. It has been previously shown that TCR triggering without CD28 co-stimulation results in T-cell anergy or unresponsiveness[152,153]. In addition, CD28 blockade has been shown to regulate alloimmune responses during transplants[154]. Furthermore, CD28 has been heavily implicated in response to PD-1 cancer immunotherapy[155,156]. However, how these two receptors orchestrate T-cell activation through regulating the dynamics of TCR microclusters remains unknown[157].

In addition to co-stimulatory molecules, co-inhibitory molecules known as checkpoint blockades are crucial to the function of TCRs. CTLA-4 is one such receptor expressed on T cells. As described in Chapter 1, CTLA-4 shares the same ligands as CD28, CD80, and CD86, but elicits a response antagonistic to that of CD28[158]. Contrary to CD28, CTLA-4 has been shown to exist primarily intracellularly in naïve T cells, and is recruited to the immunological synapse upon TCR engagement[159]. CTLA-4 then sequesters CD80/86 from CD28 at the immunological synapse[76], and is thus thought to be a temporal negative regulator to prevent overstimulation. As an inhibitor of T-cell function, CTLA-4 has become a target for

checkpoint blockade immunotherapy, which has had some success in immune-hot tumors, such as melanomas, lung cancers, and cervical cancers[55,160].

An additional inhibitory molecule to CTLA-4 is Programmed death receptor 1 (PD-1). PD-1 binding to its ligand, programmed death ligand 1 (PD-L1), activates phosphatase SHP1/2, which then dampens signaling of TCR[161]. PD-1 signaling has also been shown to drive TCR downregulation, thus preventing over-stimulation[162]. PD-1 has also been implicated in cancer as a mechanism of immune evasion[163]: tumor cells upregulate expression of PD-L1, thus blocking T-cell recognition and clearance of tumor cells. Interestingly, however, PD-L1 expression in tumors has not been correlated to responders vs. non-responders: conclusive indicators for response to PD-1 checkpoint blockades are still under investigation[164–167]. In addition, the effect of PD-1 signaling versus blockade on TCR cluster structure and dynamics has yet to be determined. Combination therapy of CTLA-4 and PD-1 blockades together has elicited promising results, as has the use of either monotherapy as a neoadjuvant treatment prior to surgical intervention[168].

Beyond accessory molecules to assist in TCR signaling, the ability for a TCR to discriminate between self and foreign ligands is essential for adaptive immunity. The dysfunction of TCR ligand discrimination can directly lead to cancer, infection, or autoimmunity. Moreover, TCR ligand discrimination displays two important characteristics: (1) high sensitivity – TCRs can recognize even a single agonist pMHC in the presence of abundant self-pMHCs[132,169]; and (2) high specificity – TCRs can discriminate between structurally similar peptides and elicit distinct immune responses[170–172] . Despite its critical importance, the molecular mechanism of TCR ligand discrimination remains controversial[121]. A common problem is that most existing mechanistic models were proposed based on *in vitro* studies which often cannot reliably predict physiological events *in vivo*. One example is that the high-affinity, slow off-rate, and high-potency (as defined by *in vitro* measurements) K5 peptide triggers attenuated *in vivo* T-cell responses[173] , and such experimental data cannot be explained by the prevailing kinetic models that were built based on *in vitro* binding affinity and/or half-life[120,121,173] . In an effort to overcome the limitations

imposed by *in vitro* studies, we applied our LaMDA approach to study TCR ligand discrimination to evaluate whether it can accurately predict physiological *in vivo* T-cell responses.

## RESULTS

### *LaMDA Can Distinguish Signaling Blockades from Endogenous Signaling*

To understand the role of CD4 in regulating TCR signaling, we used an anti-CD4 Fab to block CD4 binding, an anti-CD28 Fab to block CD28 binding, and PP2, a Src family kinase inhibitor to block Lck signaling. We first confirmed that our anti-CD28 Fab does not activate TCR signaling, contrary to full CD28 antibodies (Fig. 5A). We next measured the 4D dynamics of TCR microclusters by LLSM. The XGboost classifier predicted that a subset (66%) of the TCR microclusters after CD4 blockade are in the resting state (Fig. 5B). The signaling state change of the T cell after CD4 blockade was further verified by the mean duration of TCR microclusters (Fig. 5C and 5F) obtained by Weibull distribution fitting. Importantly, the value of mean duration alone cannot represent the overall TCR microcluster stability, again reinforcing the need for big data analyses techniques to incorporate many parameters simultaneously. A shift from stimulated state to resting state was also observed in the TCR microcluster diffusion map (Fig. 5I), where the distribution of CD4 blockade was located between those of the resting and the stimulated T cells. We also found that CD4 blockade significantly reduced the stability of TCR microclusters, as shown by the reduction of energy well depth in the pseudo-energy wells (Fig. 5I-K). As CD4 signals through its associated tyrosine kinase Lck[144,146,147] we next blocked the Lck activity using a Src family kinase inhibitor PP2. Similar to CD4 blockade, we found that PP2 inhibition also shifted the T-cell signaling state from stimulated state towards to resting state, as shown by the XGboost classifier predictions (Fig. 5B), mean duration (Fig. 5C and 5G), diffusion maps (Fig. 5I-J) and pseudo-energy well (Fig. 5K). These data reinforce that CD4 and Lck are critical molecules that facilitate TCR signaling.

To understand the role of CD28 co-stimulation to TCR signaling, we used an anti-CD28 Fab to block the CD28 co-stimulatory signal (Fig. 5A). After CD28 blockade, our assays showed that T-cell

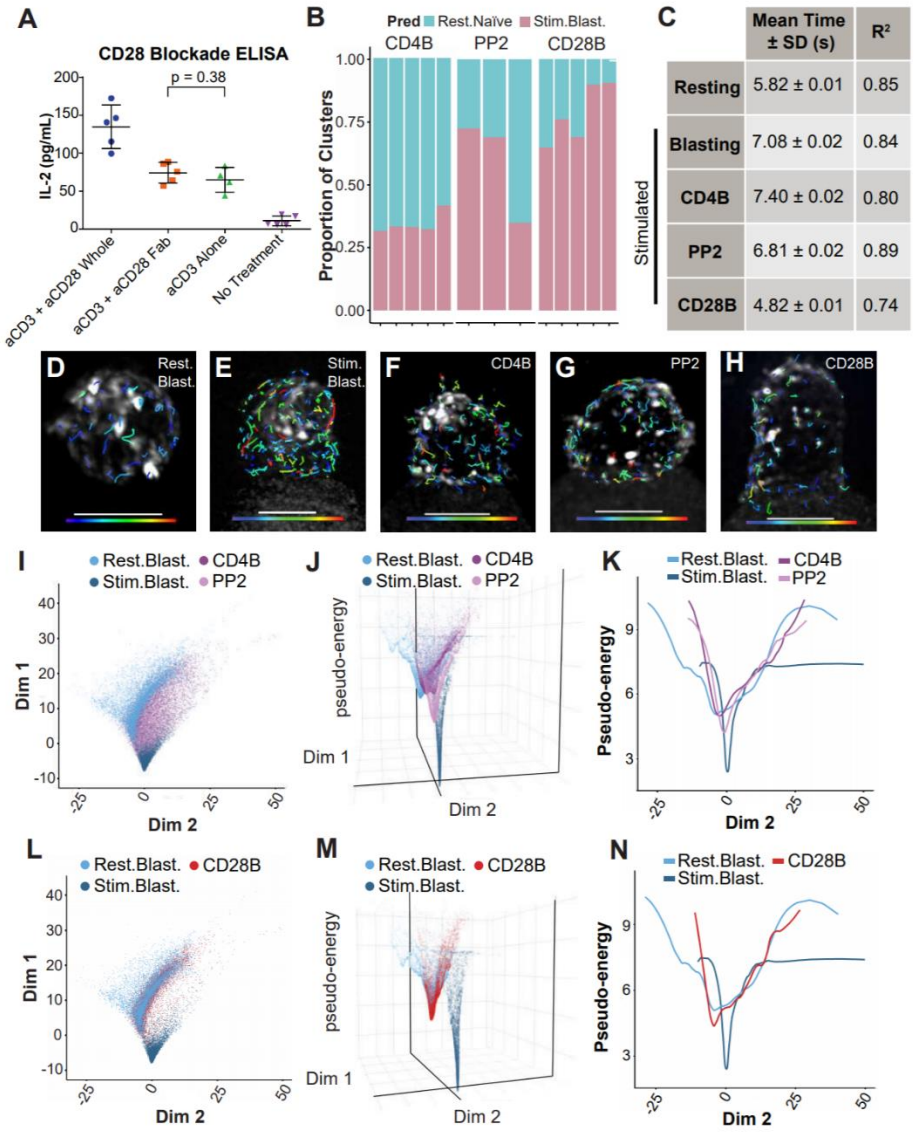


**Figure 5: LaMDA reveals changes in cell signaling states induced by perturbations.** (**A**) CD28 blockade by anti-CD28 Fab diminishes T cell cytokine production. T-cell IL-2 cytokine production measured by ELISA experiment. 5C.C7 T cell blasts are stimulated by anti-CD3 mAb and anti-CD28 mAb, anti-CD3 mAb and anti-CD28 Fab, anti-CD3 mAb alone, and culture medium. Data are presented as mean ± standard deviation (SD). (**B**) XGboost prediction results on microclusters from stimulated blasting cells treated with CD4 blockade (n = 51,383 microclusters), PP2 (n = 35,666 microclusters), and CD28 blockade (n = 34,019 microclusters). Each bar represents an independent cell. (**C**) Table of mean duration obtained by Weibull distribution fittings of microcluster track durations from each cell group. Data are presented as mean ± standard deviation (SD) and the goodness of fit is indicated by $R^2$ values. (**D**-**H**) Three-dimensional renderings of resting blasting cell (**D**), stimulated blasting cell (**E**), stimulated blasting cell treated with CD4 blockade (**F**), stimulated blasting cell treated with PP2 (**G**), and stimulated blasting cell treated with CD28 blockade (**H**). All images are overlaid with dragon tails showing particle positions over the previous eight frames are color coded to show particle track duration (0-25 s). Scale bars = 5 µm. (**I**) Diffusion map built from the same selected features as Figure 4A, with colors indicating cell group. (**J**) 3D Pseudo-energy map of (I) of resting blasting cells, stimulated blasting cells, stimulated blasting cells with CD4 blockade (CD4B) and stimulated blasting cells treated with PP2 with colors indicating each cell group. (**K**) Projection of pseudo-energy map from (J) along dimension 2. (**L**) Diffusion map built from the same selected features as Figure 4A, with colors indicating cell group. Continued on next page.

**Figure 5: LaMDA reveals changes in cell signaling states induced by perturbations.** Continued from previous page: (**M**) 3D pseudo-energy map of (L) of resting blasting cells, stimulated blasting cells, and stimulated blasting cells with CD28 blockade (CD28B) with colors indicating each cell group. (**N**) Projection of pseudo-energy map from (M) along dimension 2. (**H**) UMAP of data from (F-G) with color indicating cell group. Boundary line represented in blue. (**I**) UMAP of data from (F-G) with color indicating probability of microcluster to be a stimulated blasting microcluster as predicted by XGboost binary classifier. Probability was indicated by color scale (0.00-1.00). Boundary line represented in blue. (**J**) SHAP values of each property of the microcluster in XGboost binary classifier. (**K**) Weibull distribution fitting of microcluster track duration from stimulated blasting cells to obtain mean track duration. See also Figure 17C-F. (**L**) Table of mean track duration for each cell group obtained by Weibull distribution fittings. Data are presented as mean ± standard deviation (SD) and the goodness of fit is indicated by $R^2$ values. Scale bars = 5 μm. This figure is reproduced from Rosenberg, et al., *Cell Systems* 2020.

signaling state also transitioned to the resting state, as demonstrated by the XGboost classifier predictions (Fig. 5B), mean duration (Fig. 5C and 5H), diffusion map (Fig. 5L-M), and pseudo-energy well (Fig. 5N).

*LaMDA Results of Checkpoint Blockade Disagree with Prior Data*

We further tested the effect of PD-1 blockade on TCR cluster dynamics as analyzed by LaMDA. Previous experiments in our lab showed that PD-1 expression peaks on Day 2 post stimulation (Fig. 18) so we chose to utilize Day 2 T cells for this experiment. Interestingly, the Day 2 control cells exhibited TCR microclusters that did not fully activate to the stimulated state, as shown by the machine learning prediction (Fig. 6A), Weibull-derived average lifetimes (Fig. 6B), and pseudo-energy map (Fig. 6E). Also, contrary to expectations, both the CTLA-4 and PD-1 blockades resulted in even further inhibition. The machine learning prediction shows that even more of the TCR microclusters remain in the resting state compared to that of the Day 2 control (Fig. 6A). The diffusion map and pseudo-energy maps also show a reduced pseudo-energy and a shift towards the resting state (Fig. 6C-E). Interestingly, Weibull-derived average lifetimes show that CTLA-4 blockade cells have a longer lifetime than that of blasting cells (stimulated for 6-10 days) (Fig. 6B). This could be potentially due to the fact that CTLA-4 directly contributes to downregulation of the TCR by competing for CD28 ligands[160], and thus the removal of this endogenous competition results in the TCRs remaining on the surface longer. By contrast, PD-1 signals further downstream from CTLA-4 and the TCR[160], and may not have the same result.

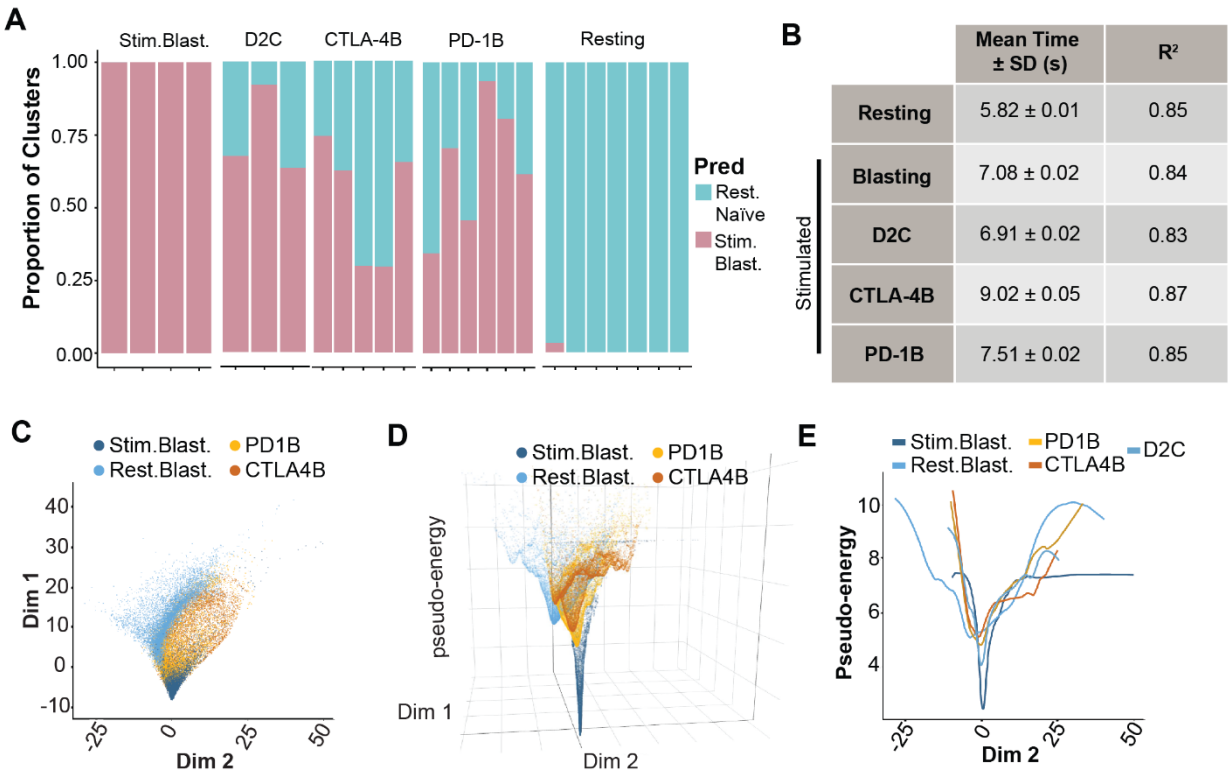


**Figure 6: LaMDA reveals changes in cell signaling states induced by checkpoint blockades.** (**A**) XGboost prediction results on microclusters from stimulated blasting cells: Day 2 Control (D2C) (n = 51,383 microclusters), CTLA-4 Blockade (n = 35,666 microclusters), and CD28 blockade (n = 34,019 microclusters). Each bar represents an independent cell. (**B**) Table of mean duration obtained by Weibull distribution fittings of microcluster track durations from each cell group. Data are presented as mean ± standard deviation (SD) and the goodness of fit is indicated by $R^2$ values. (**C**) Diffusion map built from the same selected features as Figure 4A, with colors indicating cell group. (**D**) 3D Pseudo-energy map of (C) of resting blasting cells, stimulated blasting cells, stimulated blasting cells with PD-1 blockade (PD1B) or CTLA-4 Blockade (CTLA4B) with colors indicating each cell group. (**E**) Projection of pseudo-energy map from (D) along dimension 2.

*LaMDA Ligand Discrimination Agrees with* in vivo *Data*

Next, we measured the TCR microcluster dynamics stimulated by three structurally similar peptides K5, MCC, and 102S using LLSM[173] (Fig. 7B). K5 and 102S were previously designated a super-agonist and weak agonist, respectively, *in vitro*. We then applied the same XGboost classifier trained on MCC-stimulated vs. unstimulated TCR microclusters to this data set. The XGboost classifier predicted that ~89.3 and ~76.1% of the microclusters stimulated by variants K5 and 102S, respectively, are in the stimulated state (Fig. 7A). This indicates that both K5 and 102S stimulations resulted in partial activation, consistent with previous *in vivo* studies which showed that both K5 and 102S peptides resulted in attenuated immune responses compared to the MCC[173]. Consistent with machine learning, we found that the Weibull-derived average lifetimes of 102S- and K5-stimulated microclusters were similar to those of MCC-stimulated microclusters, but significantly different from those of resting microclusters (Fig. 7C-H, Fig. 17F).

To systematically study TCR ligand discrimination, we plotted a diffusion map of the TCR microclusters stimulated by the three structurally similar peptides K5, MCC, and 102S (Fig. 7I-J). After converting the diffusion map to 3D (Fig. 7K) and 2D (Fig. 7L) energy wells, we were able to clearly visualize different activation states of T cells. Compared to the resting-state T cells without stimulation (blue), MCC-mediated stimulation (dark blue) induced the formation of the most stable TCR microclusters, while K5 (dark green) and 102S (green) resulted in less stable TCR microclusters. Our findings are well aligned with a previous *in vivo* study by Allison and colleagues showing that the MCC peptide, rather than the K5 and 102S, triggers the optimal intracellular signaling, cytokine production, and cell proliferation[173].

Additionally, to fully test whether we can apply machine learning to TCR ligand discrimination, we trained another XGboost softmax classifier to distinguish between the TCR microclusters on T cells stimulated by MCC, K5, and 102S. We found that this alternative machine learning approach could be used to precisely differentiate between the TCR microcluster organization following stimulation by the three structurally similar peptides with ~96% accuracy (for training, validation, and test data sets) (Fig. 7M-N).

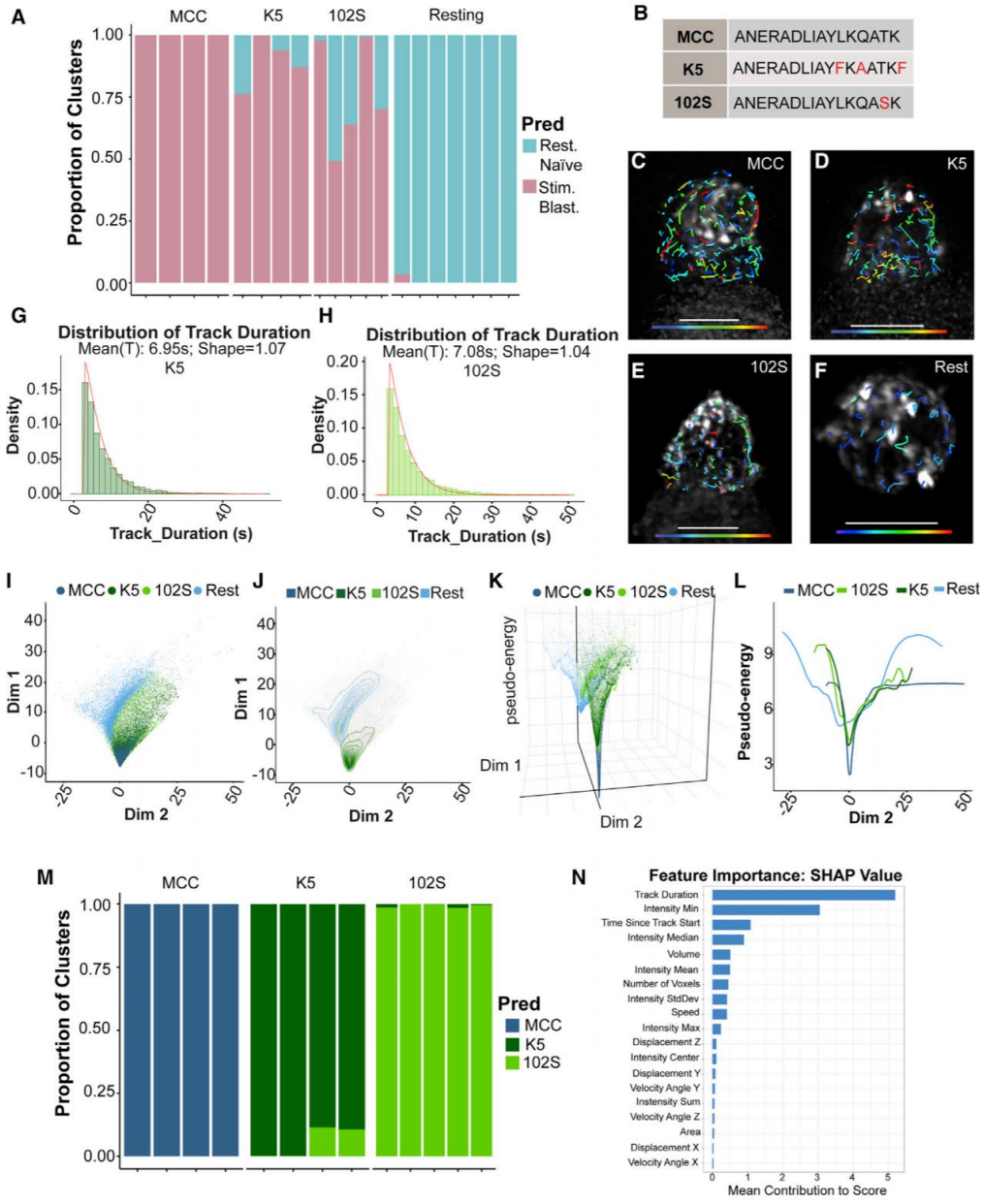


**Figure 7: TCR ligand discrimination by LaMDA.** (**A**) XGboost prediction results on microclusters from blasting cells stimulated with MCC (n = 97,237 microclusters), K5 (n = 24,786 microclusters), and 102S (n = 46,218 microclusters), and unstimulated resting cells (n = 58,784 microclusters). Each bar represents an independent cell. (**B**) Table of peptide sequences for MCC, K5, and 102S. (**C**-**F**) Three-dimensional renderings of blasting cells stimulated with MCC (**C**), K5 (**D**), and 102S (**E**) and unstimulated resting blasting cells (**F**). All images are overlaid with dragon tails showing particle positions over the previous eight frames are color coded to show particle track duration (0-25 s). Scale bars = 5 µm. (**G**-**H**) Weibull distribution fitting of microcluster track duration from blasting cells stimulated with K5 (**G**) or 102S (**H**). (**I**) Diffusion map built from the same selected features as Figure 4A, with colors indicating cell groups. (**J**) Density map created from (I). (**K**) 3D pseudo-energy map created from (J) of blasting cells stimulated with MCC, K5, and 102S peptides, and resting blasting cells, with colors indicating cell groups. (**L**) Projection of pseudo-energy map from (K) along dimension 2. (**M**) Separate XGboost classifier built to differentiate microclusters from cells stimulated with MCC, K5, or 102S. (**N**) SHAP values of each feature as used in XGboost binary classifier in (M). This figure is reproduced from Rosenberg, et al., *Cell Systems* 2020.

## CONCLUSIONS

These data together not only reinforce that the CD4, Lck, and CD28 are critical molecules for TCR activation, but also identify them as enhancers of TCR signaling via global TCR microcluster stabilization, facilitating antigen recognition and signal amplification. However, we found that blockade of inhibitory receptors PD-1 and CTLA-4 resulted in inhibition of signaling as well. This could potentially be due to the use of Day 2 stimulated T cells rather than the conventional blasting T cells that have been stimulated for 6-10 days, as we saw a decrease in TCR activation in the Day 2 control cells (Fig. 6). Further experiments with conventional blasting T cells are required. However, it could also mean that TCR microclusters do not properly function in the absence of inhibitory regulation. In addition, PD-1 does exist on the surface of naïve T cells, and thus PD-1 blockade of naïve cells should be examined. However, this does not hold for CTLA-4 blockade, as CTLA-4 is largely intracellular prior to TCR engagement[158].

In our probing of ligand discrimination, we found that both K5- and 102S-mediated stimulation of T cells resulted in partial activation when compared to MCC (Fig. 7). Our observations complement *in vivo* studies that have shown the K5 peptide results in attenuated immune responses compared to the MCC peptide[173], but stand in contrast to *in vitro* studies that have previously shown K5 is a super-agonist with the highest TCR affinity and results in the strongest activation of T cells amongst the three peptides[173–175] . This suggests that, unlike common *in vitro* approaches, our LaMDA pipeline may be able to predict *in vivo* peptide potency in activating T cells and could be extended toward the development of peptide vaccines to treat infection, cancer, and autoimmunity[176,177] or be used to study thymic education and/or peripheral tolerance, two very important topics in T-cell biology. Further experiments are required to confirm this link to *in vivo* functionality. We expect our LaMDA pipeline can be extended to a wide range of ligand discrimination systems and detect subtle yet important dynamic differences between cell states, which provides a more physiologically relevant approach to study immune molecules and cells in cancer, infection, and autoimmunity.

# CHAPTER 5: LaMDA REVEALS GLOBAL SIGNALING DYNAMICS

## INTRODUCTION

Our data from Chapters 3 and 4 suggest that TCR microclusters directly reveal different signaling states of a T cell and support current biological understanding of TCR dynamics. However, our analyses in Chapters 3 and 4 largely ignore the spatiotemporal advantage of LLSM, so we next sought to probe the global dynamics of the TCR on the entire T cell surface. Previous literature had reported on a "distal pole" or "anti-synapse", a concentration of TCRs on the pole opposite to the interface with the APC that occurs within seconds of initial contact and disperses within one minute[178–181]. First observed in 2001 by Allenspach *et al.* investigating CD43 motion[180], the distal pole was shown to accumulate CD43 and Rho-GDI. The distal pole was later shown to also contain CD28, LAT, Lck, CD3, and PLC$\gamma$[181]. The distal pole was also shown to persist without the TCR and in the presence of microtubule inhibitor nocodozole, despite a decrease in $Ca^{2+}$ flux[181]. Thus, $Ca^{2+}$ is not a causative factor for the distal pole. However, Allenspach *et al.* showed that inhibition of ezrin or moesin, two linkers of molecules to the actin cytoskeleton, did prevent the formation of the distal pole[182]. Thus, we know the formation of the distal pole is reliant on the actin cytoskeleton for motion. It is known that TCR microcluster dynamics are closely linked with the actin network, which globally reorganizes with TCR-pMHC binding and signaling[140,183–189] . Thus, we sought to determine whether the TCR participates in this distal pole reorganization, and to probe whether further dynamic organization could be discerned.

## RESULTS

### *LaMDA Identifies TCR Microcluster Global Change*

Indeed, we observe that upon APC contact, the TCRs concentrated at the distal pole, quickly dispersed into small TCR microclusters, then continuously trafficked to the immunological synapse across the T-cell surface (Fig. 8A-D, Movies 5-6). In agreement with previous literature, this distal pole was

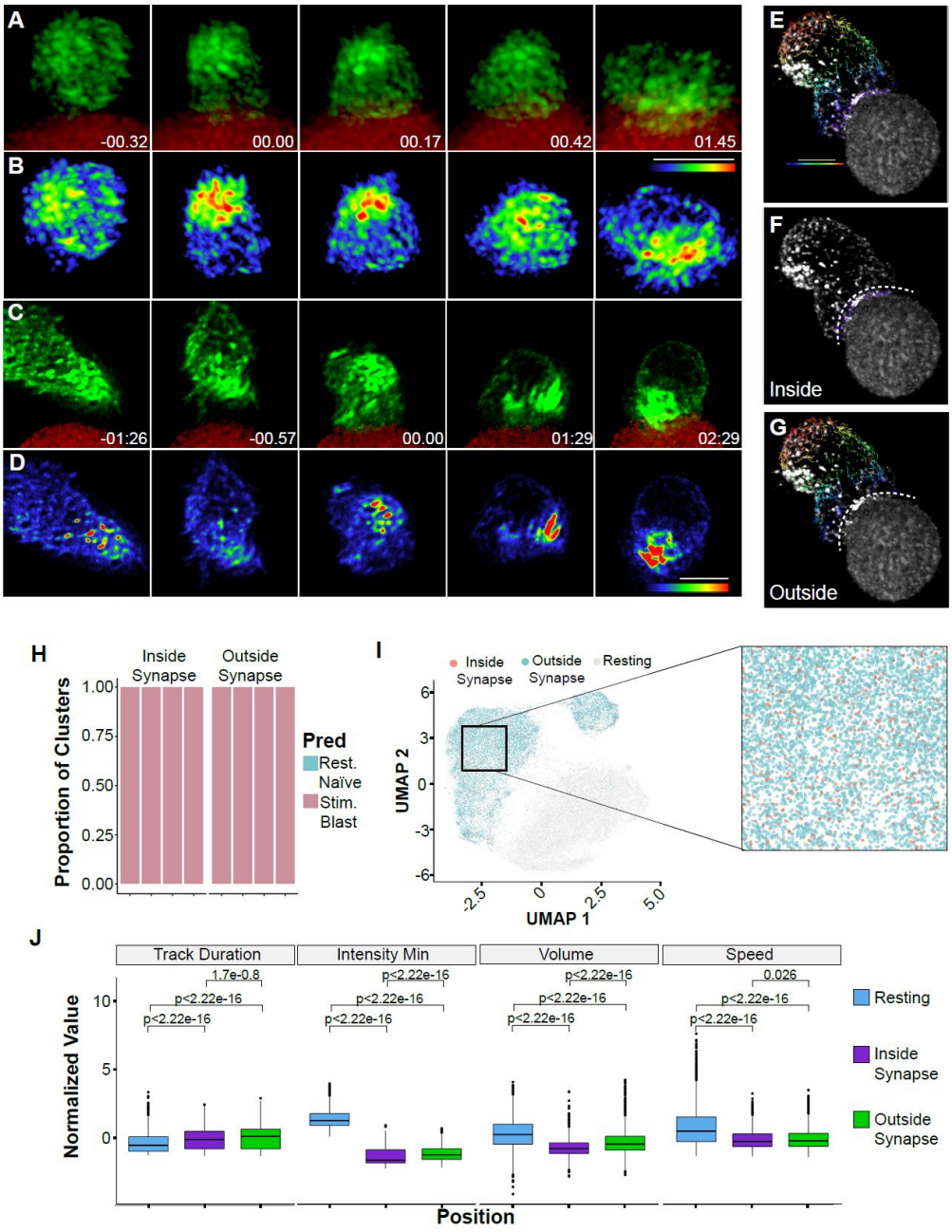


**Figure 8: LaMDA identifies TCR microcluster global change.** (**A**) Time-lapse of a three-dimensional rendering of a naïve CD4+ T cell labelled with anti-TCRβAF488 Fab as it encounters a mCherry-CH27 cell loaded with MCC peptide. See also Supplemental Movie 5. Time is shown as min:s with 00:00 as initial contact time. (**B**) Time lapse from (A) pseudo-colored by intensity from cold (0 gray) to hot (85 gray). (**C**) Time lapse of a three-dimensional rendering of a blasting CD4+ T cell labelled with antiTCRβ-AF488 Fab as it encountered an mCherry-CH27 cell loaded with agonist MCC peptide. See also Supplemental Movie 6. Time is shown as min:s. (**D**) Time lapse (from C) pseudo-colored by intensity from cold (0 gray) to hot (78 gray). Scale bar = 5 µm. (**E-G**) A distance map outward from the antigen presenting cell surface was created to determine the distance of each microcluster from the synapse. With a z-step size of 0.4 µm (representing maximum z-resolution) all microclusters ≤ 0.4 µm from the antigen presenting cell surface were labeled as "inside synapse", and those > 0.4 µm from the antigen presenting cell surface were labeled as "outside synapse". Continued on next page.

**Figure 8: LaMDA identifies TCR microcluster global change.** Continued from previous page: Stimulated blasting cell overlaid with dragon tails showing particle positions over the previous eight frames are color coded to show particle distance from antigen presenting cell. Cell is shown with all tracks (E), tracks inside synapse only, as defined by distance ≤ 0.4 μm (F), and tracks outside synapse only, as defined by distance > 0.4 μm (G). (**H**) XGboost prediction results on microclusters from stimulated blasting cells inside and outside of the synapse. Each bar represents an independent cell. (**I**) UMAP from Figure 3H colored by microcluster location on cell comparing inside synapse versus outside synapse. Inset shows enlarged region. (**J**) Box plots showing the distribution of track duration, intensity minimum, volume, and speed of microclusters from resting, inside synapse, and outside synapse. Center line represents median; box limits represent upper and lower quartiles; whiskers represent 1.5× interquartile range; points represent outliers. P values determined by Wilcoxon signed-rank test. Scale bars = 5 μm. This figure is reproduced from Rosenberg, et al., *Cell Systems* 2020.

transient, and dissociated within a minute[178–181]. We next sought to use the LaMDA pipeline to determine whether there was a difference in TCR microclusters that exist within the immunological synapse versus those that are present in the distal pole. To achieve this, a distance map was created going outward from the APC (Fig. 8E). Microclusters that were less than 400 μm (z-resolution) from the APC were considered inside the synapse (Fig. 8F), and microclusters farther than 400 μm from the APC were designated outside of the synapse (Fig. 8G). Indeed, LaMDA was unable to identify differences between microclusters inside and outside the synapse (Fig. 8H-J). The machine learning prediction labeled TCRs on the entire cell to be synaptic TCRs (Fig. 8H), and when labeled on the UMAP, the synaptic clusters were evenly distributed amongst the outside synapse clusters (Fig 8I). We further analyzed the top four SHAP features (Fig. 3J): Track Duration, Intensity Min, Volume, and Speed. The difference between the microclusters inside versus outside the synapse was lower than that between the resting and blasting microclusters (Fig. 8J). This suggests that TCR triggering at the synapse propagates rapid, global re-organization of TCRs for effective antigen recognition and signaling. To our knowledge, such global, dynamic, and directional structural changes of TCR microclusters on the 3D T-cell surface had not yet been observed using conventional microscopy techniques or other biochemical/biophysical assays.

*Coordinated Global TCR Cluster Dynamics*

With the global TCR dynamics shown, we sought to determine whether there was any coordinated activity over time across the whole cell. Indeed, when plotted against time, the average area of clusters within the synapse (Fig. 8F) are well coordinated with the average distance of these clusters to the APC

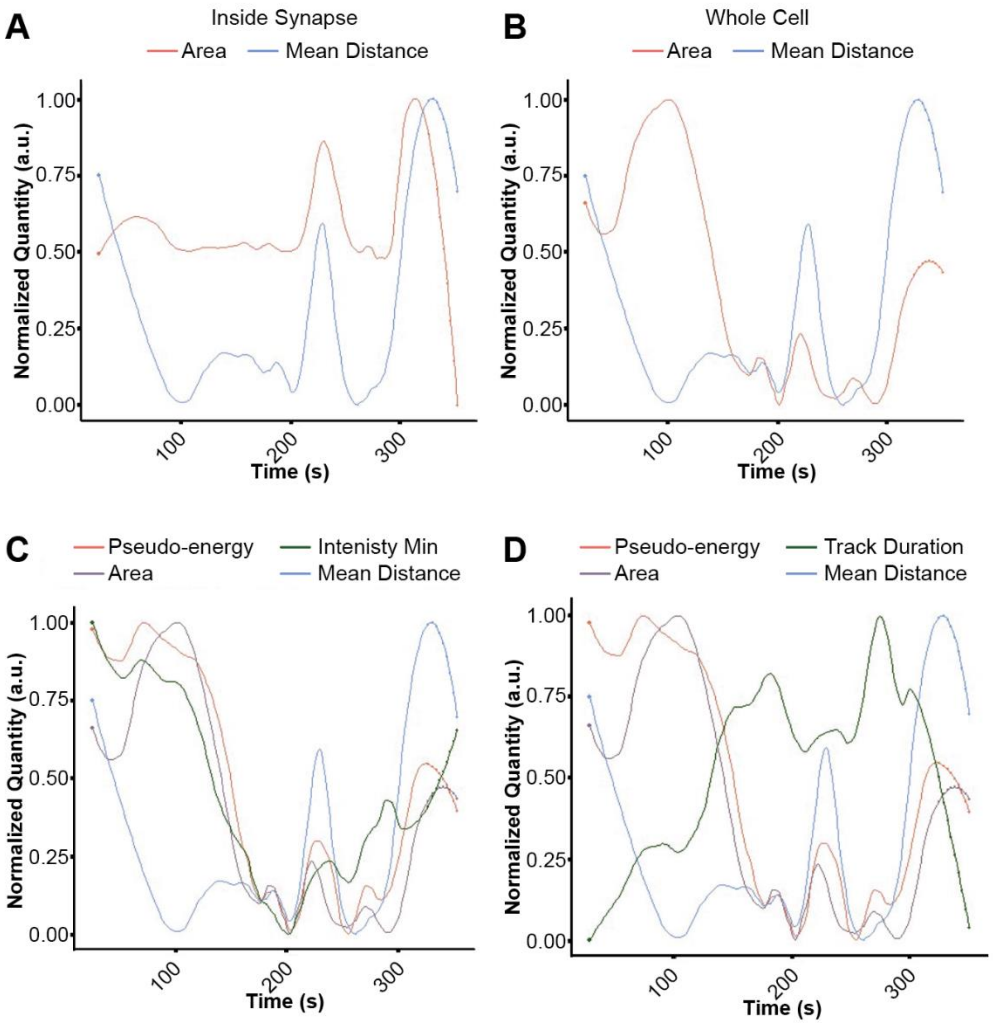


**Figure 9: TCRs Display Coordinated Global Signaling Dynamics.** (**A**) Time course plot showing the average area (red) of clusters within the synapse (Fig. 8F) and the mean distance (blue) of the clusters within the synapse (Fig. 8F) from the APC. (**B**) Time course plot showing the average area (red) of clusters across the whole cell (Fig. 8E) and the mean distance (blue) of the clusters within the synapse (Fig. 8F) from the APC. (**C**) Time course plot showing the average area (purple), average minimum intensity (green), and average pseudo-energy (red) of clusters across the whole cell (Fig. 8E), and the mean distance (blue) of the clusters within the synapse (Fig. 8F) from the APC. (**D**) Time course plot showing the average area (purple), average track duration (green), and average pseudo-energy (red) of clusters across the whole cell (Fig. 8E), and the mean distance (blue) of the clusters within the synapse (Fig. 8F) from the APC.

surface (Fig. 9A). Interestingly, once initial contact between the T cell and APC is made (around 100 s) the area of the clusters across the entire cell (Fig 8E) is also well coordinated to the average distance of the synaptic clusters to the APC (Fig. 9B). We also sought to determine whether this trend applies to features other than area: indeed, pseudo-energy, and minimum intensity were also well coordinated (Fig. 9C). Interestingly, track duration was anti-coorelated to the mean distance (Fig. 9D). Together, these data suggest that TCR signaling is very closely coordinated across the entire cell surface, rather than just at the immunological synapse as was previously thought.

**CONCLUSIONS**

In summary, we demonstrated that, assuming all other terms that contribute to energy are held constant, TCR-pMHC ligation not only stabilizes TCR microclusters globally across the entire T-cell surface (Fig. 8), but also causes coordinated dynamic activity across the TCR clusters on the entire cell. Interestingly, the oscillating pattern of dynamic changes in the TCR microclusters was only observed during the very early synapse dynamics; the longer the synapse occurred, the more damped the oscillation was. In videos in which we did not observe the beginning of the synapse, the oscillation was not observed and coordinated activity was not determined (data not shown). Thus, we hypothesize this oscillation may play a role in preventing overstimulation in T cells, although further studies are needed to confirm.

Such global, coordinate dynamic activity had not been previously reported, and begs the question of what mechanism causes this? This study showed that the distal pole formation is not disrupted by signaling blockades downstream of the TCR. The only known signal cascades that are global are $Ca^{2+}$ signaling[190] and cytoskeleton rearrangement[191–193], but it was previously shown that disrupting the $Ca^{2+}$ cascade does not prevent distal pole formation[181]. Thus, the mechanism must lie within the cytoskeleton, as it has been previously shown that TCR movement and signaling are closely tied with both the microtubule[194,195] and the actin[191–193,196–201] cytoskeletons. Unfortunately, disruption of the cytoskeleton prevents synapse formation, and thus cannot be used as a mechanism of disrupting the global dynamics.

# CHAPTER 6: DISCUSSION

## CONCLUSIONS

In this dissertation, the creation and application of a novel pipeline, entitled LaMDA, was described, which applies machine learning and dimensionality reduction techniques to 4D imaging data from LLSM. We showed that we were able to train our machine learning classifier to decipher between TCR clusters from resting T cells and those from stimulated, synapse-forming T cells with 100% accuracy. Further, we showed patterns of activation in which the TCRs changed speed, density, and size upon activation through diffusion maps. Finally, we showed that we were able to determine the pseudo-energy of each TCR cluster based on the principles of Gibb's Free Energy.

Our LaMDA approach was also able to precisely identify the roles of co-stimulatory receptors and showed interesting results upon the application of checkpoint blockades. While LaMDA confirmed the important roles of CD28 and CD4/Lck signaling, it found reduced signaling capacity upon the blockade of inhibitory receptors. This could indicate the importance of such negative feedback loops; we hypothesize that optimal TCR signaling requires such a dampening effect, and that blocking these pathways may lead to exhaustion and insufficient signaling. However, future studies are required to tease out the mechanism for such dampened signaling. In addition, LaMDA was able to accurately differentiate between T-cell stimulations triggered by structurally similar peptide ligands of different affinities. Interestingly, the LaMDA results were more correlated with previous *in vivo* data, in which the "superagonist" K5 was shown to actually be a weak agonist. However, both the K5 results and the checkpoint blockade results are reminiscent of the concept of thymic selection[202], in which T cells that signal too strongly are selected against, as they may have autoimmune capabilities. Future studies are required to determine whether LaMDA can be used as a model to study tolerance, particularly peripheral tolerance[202].

Finally, these studies resulted in the discovery of global signaling mechanisms, coordinating dynamic activity of TCRs across the entire cell. While the presence of the distal pole had previously been

identified[178,179,182,203–205], we were able to add to these data by confirming that the TCR also participates in such signaling. Furthermore, the coordinated oscillating dynamics had not previously been shown. This coordinated activity may indicate that TCR signaling is even more closely linked to the actin cytoskeleton than previously thought, and also that the synapse is not the only location in which important signaling events happen. Future studies are required to determine what the function of this coordinated global activity could be, as well as determine downstream signaling that originates from outside the synaptic interface. These studies may lead to new models of TCR triggering.

Overall, LaMDA provided new insights to T-cell biology. However, its uses could be far broader than displayed in this dissertation. It is the first comprehensive platform showing the ability to use dimensionality reduction techniques in imaging data, and thus, we expect wide future uses of LaMDA and/or similar pipelines. We hope that it lays the groundwork for deeper analysis of 4D imaging data.

## FUTURE DIRECTIONS

In addition to uncovering new T-cell biology, LaMDA can also be used to guide the pre-clinical design, development, and improvement of immunotherapies and vaccines for cancer, infection, and autoimmunity. Furthermore, as a flexible and broadly applicable pipeline, LaMDA provides a framework for future studies of other surface receptors or intracellular molecules on different cell types by directly linking molecular dynamics to cell signaling/function.

One possible future direction for LaMDA is to use the platform to study Chimeric Antigen Receptor T (CAR-T) cell design. CAR-T cell immunotherapy is a recently developed, paradigm-shifting therapy in which autologous T cells are isolated from a patient, expanded, engineered to express a CAR, and reinfused to the patient[202]. The CAR itself is a receptor in which the exterior portion is an scFv recognizing a tumor antigen, and the interior portion contains T-cell machinery. First generation CARs had only CD3ζ in the intracellular portion, but second generation CARs added either 4-1BB or CD28[202]. Second generation CARs had a much higher tumor-controlling ability, and, as such, there are now several anti-CD19 CAR-T cell

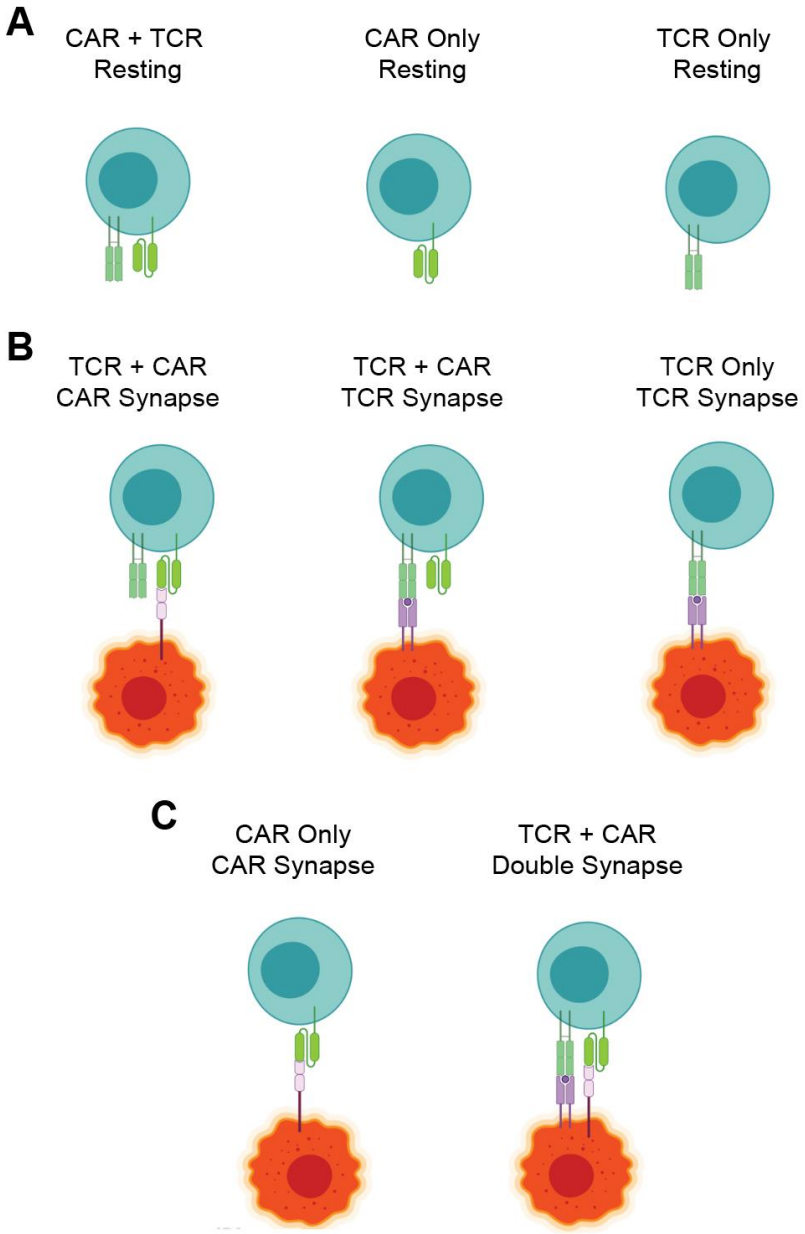


**Figure 10: Proposed project for TCR-Knockout CAR-T cell.** (**A**) Resting T cells with endogenous TCR only (right), TCR-knockout CAR (middle), or CAR with endogenous TCR (left) must be studied to determine differences in resting receptor dynamics. (**B**) Synapse studies comparing second generation CARs (CAR + TCR) engaging with either CAR-antigen (left) or pMHC (middle) should be compared against the benchmark endogenous TCR-pMHC synapse (right). (**C**) Synapse studies comparing TCR-knockout CAR binding with CAR antigen (left) with second generation CARs (CAR + TCR) engaging with both pMHC and CAR antigen (right).

therapies approved for leukemia and lymphoma. However, these therapies are personalized, extremely expensive, and sometimes ineffective[206]. In addition, CAR-T cell therapy has been largely ineffective against solid tumors, such as breast and prostate cancers[207]. Thus, many groups are working on ways to improve upon the CAR design.

A proposed mechanism to improve CAR-T cell therapy is to remove the endogenous TCR. Studies have shown that removing the endogenous TCR prevents Graft vs. Host Disease (GvHD)[208–210], thus allowing CAR-T cells to be made off-the-shelf, rather than personalized. This would greatly reduce both the cost and the time it takes to get to the patient. As such, future studies could use LaMDA to study the 4D dynamics of the CAR and TCR in order to determine whether or not there are differences in function and signaling in the absence of the TCR. The resting T cells would need to be first observed to determine any changes in baseline dynamics (Fig. 10A), and then the second generations CARs (with endogenous TCRs) and endogenous T cells would have to benchmarked for dynamic activity during synaptic engagement (Fig. 10B). Lastly, CARs without the endogenous TCR could be studied and compared against all other conditions (Fig. 10C). This project would thus take a surface receptor dynamics approach to understanding whether or not the endogenous TCR is necessary for full CAR signaling, as well as what the contribution of the TCR is to CAR signaling, leading to greater insights and understanding of CAR-T cell therapy.

Another possible use for LaMDA is to study the differences between 4-1BB CARs and CD28 CARs. It is known that 4-1BB CAR-T cells have increased persistence[211,212] and decreased exhaustion[213] in patients compared with CD28 CAR-T cells. However, CD28 CAR-T cells were shown to expand and clear tumors much more quickly than 4-1BB CAR-T cells[214]. Thus, LaMDA could be used to study the difference in initial synapse formation and global dynamics to determine a possible mechanism for these differences. Finally, LaMDA could be used to study new CAR designs by comparing them with both second generation designs as well as endogenous TCR signaling, in order to designs CARs that function more similarly to endogenous TCRs. This could improve the efficacy of current CAR-T cell therapy.

# CHAPTER 7: NANOTRAPS FOR THE CONTAINMENT AND CLEARANCE OF SARS-CoV-2

**NOTE:**

The following section describes a project that arose due to the COVID-19 pandemic that occurred during my time in graduate school. The following chapter (Chapter 9) is reproduced verbatim, with the exception of chapter title, figure numbering, and reference labeling, from my co-first authored publication entitled "Nanotraps for the containment and clearance of SARS-CoV-2", which was published in *Matter* on June 2, 2021. The authors have filed a provisional patent application for the technology described in this chapter.

**AUTHORS:**

Min Chen*, Jillian Rosenberg*, Xiaolei Cai, Andy Chao Hsuan Lee, Jiuyun Shi, Mindy Nguyen, Thirushan Wignakumar, Vikranth Mirle, Arianna Joy Edobor, John Fung, Jessica Scott Donington, Kumaran Shanmugarajah, Yiliang Lin, Eugene Chang, Glenn Randall, Pablo Penaloza-MacMaster, Bozhi Tian, Maria Lucia Madariaga, Jun Huang

*These authors contributed equally

**AUTHOR CONTRIBUTION**

Conceptualization: M.C. with input from J.H. Methodology: M.C. with input from J.H. and J.R. Investigation/experiments: M.C., J.R., X.C., A.C.H.L., J.S., M.N., T.W., V.M., A.J.E., Y.L. J.F., J.S.D., K.S., Y. L., G.R., B.T., and M.L.M. SARS-CoV-2 pseudotyped VSV generation and discussions: P.P.M. Formal Analysis: M.C. and J. R. with input from J.H. Manuscript writing: M.C., J.H., and J.R.. Funding acquisition: J.H. and E.C. Supervision: J.H. Manuscript editing and review: all authors.

**SUMMARY**

SARS-CoV-2 enters host cells through its viral spike protein binding to angiotensin-converting enzyme 2 (ACE2) receptors on the host cells. Here we show functionalized nanoparticles, termed "Nanotraps", completely inhibited SARS-CoV-2 infection by blocking the interaction between the spike protein of SARS-CoV-2 and the ACE2 of host cells. The liposomal-based Nanotrap surfaces were functionalized with either recombinant ACE2 proteins or anti-SARS-CoV-2 neutralizing antibodies and phagocytosis-specific phosphatidylserines. The Nanotraps effectively captured SARS-CoV-2 and completely blocked SARS-CoV-2 infection to ACE2-expressing human cell lines and primary lung cells; the phosphatidylserine triggered subsequent phagocytosis of the virus-bound, biodegradable Nanotraps by macrophages, leading to the clearance of pseudotyped and authentic virus *in vitro*. Furthermore, the Nanotraps demonstrated excellent biosafety profile *in vitro* and *in vivo*. Finally, the Nanotraps inhibited pseudotyped SARS-CoV-2 infection in live human lungs in an *ex vivo* lung perfusion system. In summary, Nanotraps represent a new nanomedicine for the inhibition of SARS-CoV-2 infection.

## INTRODUCTION

The severe acute respiratory syndrome coronavirus 2 (SARS-CoV-2) caused the global pandemic of coronavirus disease 2019 (COVID-19). As of January 8, 2021, SARS-CoV-2 has spread to over 180 countries and has resulted in more than 88.2 million infections and over 1.9 million deaths globally[215]. Despite tremendous efforts devoted to drug development, safe and effective medicines to treat SARS-CoV-2 infection are largely lacking. Given that the virus is within nanoscale, nanomaterial-based delivery systems are expected to play a paramount role in the success of prophylactic or therapeutic approaches[216,217]. To combat this highly contagious virus, here we set out to devise a nanomedicine termed "Nanotraps" to inhibit SARS-CoV-2 infection.

To gain entry to host cells for infection, SARS-CoV-2 surface spike protein binds to its receptor human angiotensin-converting enzyme 2 (ACE2) with high affinity[218–221]. Blocking entry of SARS-CoV-2 to host cells is one of the most effective ways to prevent infection. To achieve this goal, both soluble recombinant ACE2 proteins[222,223] and anti-SARS-CoV-2 neutralizing antibodies[224–228] have been developed to inhibit the interaction between SARS-CoV-2 spike protein and cell-surface ACE2, although they show limited potency[222,223,229]. Nanomaterial-based detection methods have been developed for COVID-19 diagnosis and monitoring[230–232], but very few nanomaterial-based therapeutic strategies have been reported[233]. Cellular membrane based nanoscale vesicles have also been developed to inhibit infection[234,235], but limited efficacy has been achieved. Inspired by tumor cells secreting PD-L1 exosomes to attenuate T-cell effector functions[236], here we designed a therapeutic nanoparticle termed "Nanotrap" to inhibit SARS-CoV-2 infection. The Nanotrap surfaces were functionalized with either ACE2 recombinant proteins or anti-SARS-CoV-2 neutralizing antibodies with high surface density. This design endowed the Nanotraps with high-avidity to outperform its soluble ACE2 or antibody counterparts to capture and contain SARS-CoV-2. Thus, the high avidity, small size, and high diffusivity of our newly engineered Nanotraps efficiently blocked the binding of SARS-CoV-2 to ACE2-expressing host cells including epithelial cells in the respiratory system, resulting in abrogation of SARS-CoV-2 entry.

Furthermore, we aimed to clear the virus after containment by the Nanotrap-mediated macrophage phagocytosis. The role of macrophages in the control of infections has long been documented[237], and recent single-cell RNA sequencing found abundant monocyte-derived macrophages in the bronchoalveolar lavage fluid of COVID-19 patients[238]. As professional phagocytes, macrophages engulf apoptotic cells by recognizing phosphatidylserine on the outer leaflet of the plasma membrane of apoptotic cells[239–241]. Phosphatidylserine coatings have been previously employed to enhance the uptake of liposomal nanoparticles by macrophages[242,243]. Thus, our Nanotraps were further designed to guide the phosphatidylserine-specific phagocytosis by macrophages, enabling not only the containment but also the clearance of SARS-CoV-2 through binding and subsequent phagocytosis.

Herein, we engineered Nanotraps composed of a Food and Drug Administration (FDA)-approved polylactic acid (PLA) polymeric core, a liposome shell, surface ACE2/neutralizing antibodies, and phosphatidylserine ligands. Our Nanotraps completely blocked pseudotyped SARS-CoV-2 entry into susceptible ACE2-overexpressing HEK293T cells, lung epithelial A549 cells, and human primary lung cells, as well as authentic SARS-CoV-2 infection of Vero E6 cells. The neutralizing capacity of the Nanotraps was shown to be ~10 times more effective than its soluble counterparts. Subsequently, macrophages efficiently engulfed and neutralized virus-bound, biodegradable Nanotraps through phosphatidylserine-guided phagocytosis without causing infection to macrophages *in vitro*. Furthermore, *in vitro* cell culture and *in vivo* intratracheal administration of Nanotraps to immunocompetent mice demonstrated an excellent biosafety profile. Lastly, the Nanotraps completely inhibited infection of SARS-CoV-2 pseudovirus in live human lungs maintained under normothermic physiologic conditions on a clinically applicable *ex vivo* lung perfusion (EVLP) system[111,244], confirming the therapeutic efficacy. Our Nanotraps are safe, effective, biocompatible, ready for mass production, and convenient to use. It presents a new type of nanomedicine to effectively contain and clear SARS-CoV-2 for the prevention and treatment of COVID-19.

## RESULTS

*Design, Synthesis, and Characterization of Nanotraps*

SARS-CoV-2 gains entry into host cells via surface spike proteins that bind to human ACE2 receptors on host cells with very high affinity[220,245–247]. To inhibit SARS-CoV-2 infection, we set out to engineer a family of nano-enabled virus-trapping particles, termed "Nanotraps", to contain and clear SARS-CoV-2 (Figure 11A). We used an FDA-approved, biodegradable PLA polymeric core and liposome shell materials to synthesize the Nanotraps. Nanotraps with different diameters (200, 500, and 1200 nm) were synthesized by varying polymer concentrations (see Methods for details) (Figure 20A). The solid PLA core acts as a 'cytoskeleton' to provide mechanical stability, controlled morphology, biodegradability, and large surface area for nanoscale membrane coating and surface modification. The lipid shell enveloping the PLA core exhibits behavior similar to that of cell membranes. The lipid shell provides a nanoscopic platform and can interact with a wide variety of molecules[248–250] either within the membrane or on the surface[251,252]. Thus, we aimed to functionalize the Nanotrap surface with a molecular bait (a recombinant ACE2 protein or an anti-SARS-CoV-2 neutralizing antibody) and a phagocytosis-inducing ligand (phosphatidylserine). We hypothesized that (1) the high-density ACE2 or neutralizing antibodies on the Nanotraps can outcompete low-expression ACE2 on host cells in capturing SARS-CoV-2, thus enabling selective virus containment by the Nanotraps, and that (2) surface phosphatidylserine ligands on suitably sized Nanotraps can trigger subsequent phosphatidylserine-mediated phagocytosis by professional phagocytes, such as macrophages, thus enabling viral clearance (Figure 1A). The resultant structures were monodispersed and significantly smaller than mammalian cells, yet still large enough to bind several SARS-CoV-2 virions (Figure 11B-F).

To characterize the Nanotraps, we first used dynamic light scattering (DLS) to measure the size dispersity of the constituent nanoparticles. Controlling particle size is important for tuning the phagocytosis efficacy, reproducible mechanical characteristics, and material biocompatibility[253,254]. The hydrolyzed diameter of the Nanotraps measured by DLS increased with the addition of each molecule

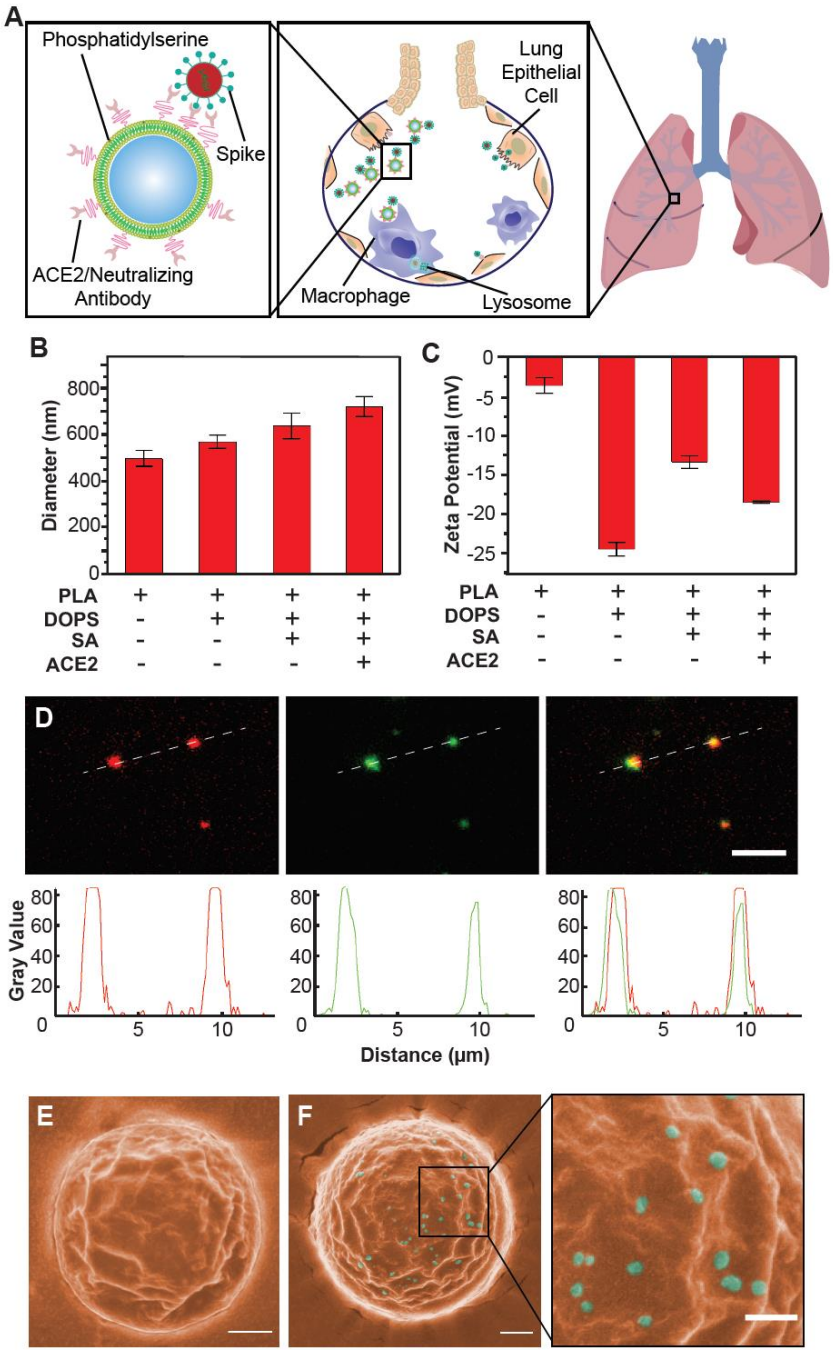


**Figure 11. Schematic design, synthesis, and characterization of Nanotraps for SARS-CoV-2**. (**A**) Schematic illustration showing the process of the Nanotraps with polymeric core coated with lipid-bilayer functionalized with ACE2 protein/neutralizing antibody. Following intratracheal administration, Nanotraps efficiently accumulated and trapped SARS-CoV-2 virions in the lung tissue forming virus-Nanotrap complexes, which can be cleared by macrophages via phagocytosis, thereby blocking viral cell-entry. (**B-C**) Dynamic light scattering (B) and Zeta-potential measurements (C) during different stages of Nanotrap preparation. (**D**) Fluorescent images of the prepared Nanotraps with PLA polymeric core (DiD, red) and ACE2 (anti-ACE2-AF488, green). Scale bar represents 5 μm. Dotted lines represent displayed plot profile below. (**E-F**) Pseudocolored SEM images of Nanotraps alone (E, orange) or with SARS-CoV-2 pseudovirus (F, cyan). To better visualize the selectivity for viral binding, larger Nanotraps were imaged. Scale bar represents 300 nm. This figure is reproduced from Chen, et al., *Matter* 2021.

(Figure 11B). The zeta potential, which reflects the surface charges of the Nanotraps[255], was found to change slightly with the addition of each molecule to the Nanotrap surface (Figure 11C). We next used fluorescent labeling and total internal reflection fluorescence microscopy (TIRFM) to confirm the presence of the ACE2 moiety on the Nanotraps. The PLA polymeric core of each Nanotrap was labelled with a lipophilic carbocyanine dye: 1,1'-dioctadecyl-3,3,3',3'- tetramethylindodicarbocyanine, 4-chlorobenzenesulfonate salt (DiD, red). The Nanotrap-ACE2 were further stained with an anti-ACE2 antibody labelled with Alexa fluor-488 dye (AF488, green). The TIRFM images clearly showed excellent co-localization between the Nanotrap core and surface ACE2 at the single particle level, confirmed by line scans of the fluorescent channels corresponding to each component (Figure 11D). These results demonstrated that we have successfully functionalized the Nanotraps with recombinant ACE2 protein. We employed scanning electron microscopy (SEM) and transmission electron microscopy (TEM) to image the Nanotraps at the sub-nanometer level. SEM images showed that the Nanotraps were spherical and well-dispersed (Figure 20B). The Nanotraps appeared slightly crenellated in the SEM images, as the lipid layer may have shrunk due to the drying sample preparation procedure before imaging (Figure 11E). As expected, after incubation with the pseudotyped SARS-CoV-2 for 1 h at 37 ℃, the Nanotraps effectively captured the virus as evidenced by single virions clearly visualized on the surface of a Nanotrap; no freestanding virions were observed outside of the Nanotrap (Figure 11F). The representative TEM image clearly shows the core-shell structure of the Nanotrap (Figure 20C). Importantly, Nanotraps that were lyophilized, sealed, and stored at -20°C for six months demonstrated no change in surface integrity (Figure 20D) or size (Figure 20E), indicating excellent stability over time.

We further quantified the surface molecular densities of the two Nanotraps by flow cytometry: the Nanotrap-ACE2 has (3.59±0.43) $\times 10^5$ ACE2 molecules per Nanotrap, and the Nanotrap-Antibody has (2.47±0.2) $\times 10^4$ neutralizing antibodies per Nanotrap (Figure 20F). We hypothesize that the lower concentration of surface antibodies is due to (1) the lower efficiency conjugation method of NHS-esters versus the site-specific, high-affinity ($10^{-14}$ M)[256] biotin-streptavidin conjugation used for ACE2

conjugation in aqueous solution, and (2) imperfect antibody orientation leading to blockage of the antibody binding site to virus spike protein (Figure 20G). However, future studies can easily manipulate this surface density as needed by simply adjusting the molar ratios of DSPE-$PEG_{2000}$-biotin or DSPE-$PEG_{2000}$-NHS on the lipid shell for Nanotrap synthesis (see Methods).

*Phagocytosis by Macrophages*

Macrophages are a class of phagocytes that engulf and clear cell debris, pathogens, microbes, cancer cells and other foreign intruders[237]. Macrophages specialize in the removal of dying or dead cells by recognizing phosphatidylserine on the outer leaflet of the plasma membrane of apoptotic cells[239–241]. Phosphatidylserine coatings have been previously employed to enhance macrophage uptake of liposomal nanoparticles[257–259]. Because phagocytosis by macrophages is highly dependent on size and surface phosphatidylserine, we determined the optimal size and surface phosphatidylserine density of Nanotraps. We first synthesized Nanotraps labelled with 3,3′-Dioctadecyloxacarbocyanine perchlorate (DiO) fluorescent dye on the PLA polymeric core with varying diameters: 200, 500, and 1200 nm (Figure 21A). After incubating Nanotraps with differentiated THP-1 (dTHP-1) macrophages[260] for varying time durations, we examined the size-dependent phagocytosis by dTHP-1 macrophages using flow cytometry. We found that the 500-nm Nanotraps outperformed the 200-nm and 1200-nm counterparts after 24- and 48-h incubations, as demonstrated by the percent uptake (Figure 12A) and the mean fluorescent intensity of DiO dye (Figure 12A and Figure 21A-E) in dTHP-1 macrophages. Accordingly, 500-nm PLA-core Nanotraps were chosen for all further experiments.

We next functionalized the Nanotraps with varying surface densities of phosphatidylserine to induce phagocytosis by macrophages. The overall negative charge of the Nanotraps increases as the percentage of phosphatidylserine ratio increases, confirming the presence of phosphatidylserine (Figure 21B). We found that phagocytosis by macrophage was roughly correlated to the percentage of phosphatidylserine (Figure 12C-D). The phosphatidylserine-dependent phagocytosis of Nanotraps by

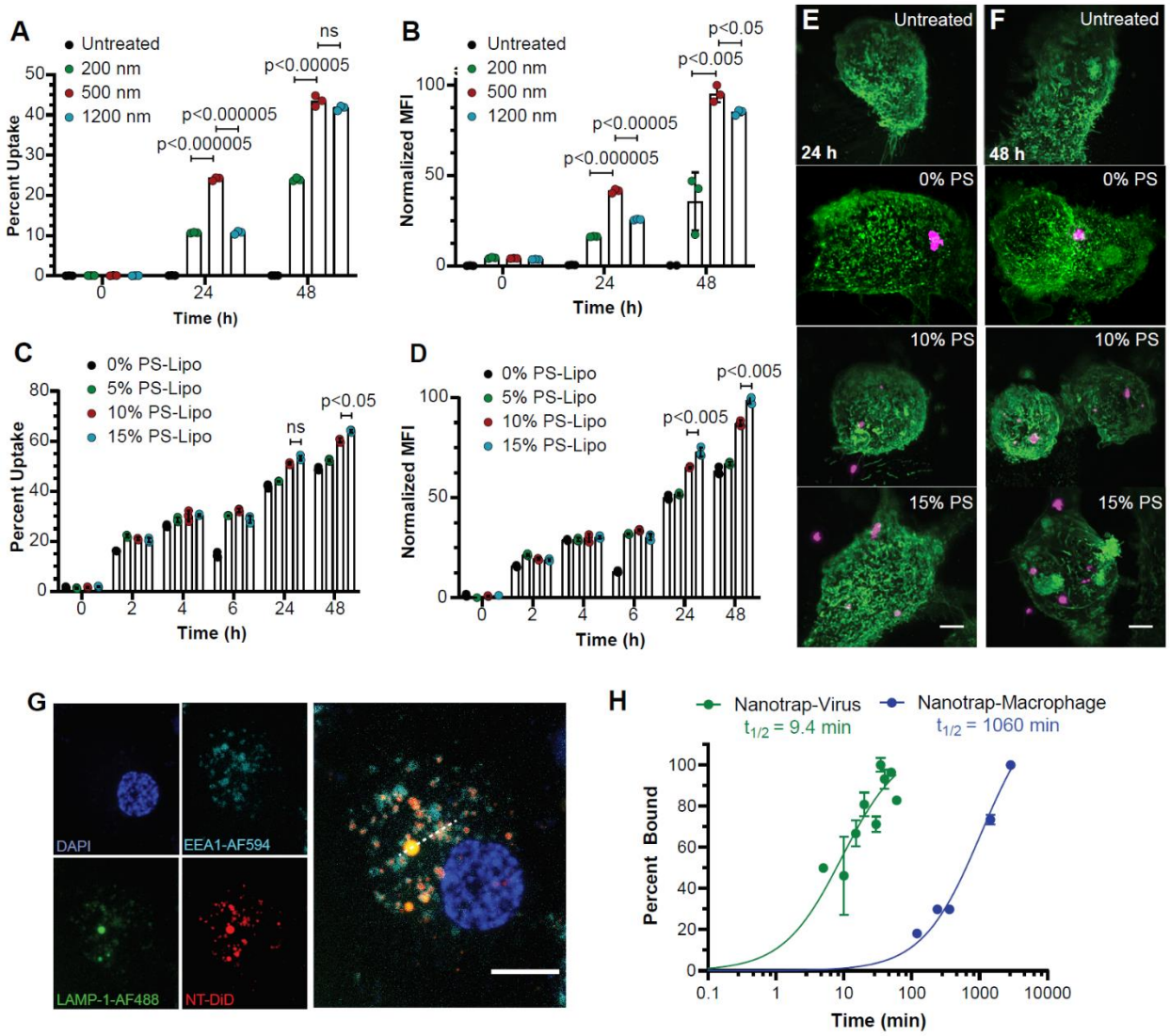


**Figure 12. Phagocytosis of Nanotraps by macrophages.** Nanotraps of varying size and phosphatidylserine (PS) densities were incubated with dTHP-1 macrophages. (**A-B**) Percent uptake (A) and mean fluorescent intensity (B) quantification of flow cytometry measurement of the internalization of Nanotraps with varying diameters. (**C-D**) Percent uptake (C) and mean fluorescent intensity (D) quantification of flow cytometry measurements of the internalization of Nanotraps with varying PS ratios. Data are shown as mean ± SD; unpaired t tests were conducted from three replicates. (**E-F**) Lattice light-sheet microscopy images of macrophages (Wheat Germ Agglutinin (WGA)-CF488, green) phagocytosing Nanotraps (DiD, magenta) after 24 h (E) or 48 h (F). Scale bar represents 5 μm. (**G**) Confocal microscopy image of dTHP-1 cell stained for DAPI (blue), lysosomes (LAMP-1-AF488, green), and endosomes (EEA1-AF594, cyan) incubated with Nanotrap-ACE2 (DiD, red) for 6 h. Dotted line indicates line scan analyzed in Figure S2. Scale bar represents 10 μm. (**H**) Viral particles labeled with lipophilic dye DiO incubated with Nanotraps (DiD) at 37°C for various time points (green) and dTHP-1 macrophages were incubated with Nanotraps (DiO) at 37°C for various time points (blue), were measured by flow cytometry. Double-positive events were gated and the mean fluorescence intensity of DiO was measured over time until saturation was reached. Data were fitted with a curve and $t_{1/2}$ was extrapolated at the time at which 50% of Nanotraps were bound or engulfed. This figure is reproduced from Chen, et al., *Matter* 2021.

dTHP-1 macrophages were further demonstrated by three-dimensional lattice light-sheet microscopy images (Figure 12E-F and Movie 9). These experiments not only confirmed successful functionalization of the Nanotraps, but also identified the optimal surface density of phosphatidylserine on the Nanotrap surfaces. Thus, we utilize the 500-nm core size and 15% surface phosphatidylserine Nanotraps for the following experiments to maximize viral capture and macrophage phagocytosis.

We further tested whether the engulfed Nanotraps would fuse with endosomes or lysosomes within the macrophages. As shown in Figure 12G, Nanotraps (DiD, red) in various regions in the cell colocalize with either endosomes (cyan) or lysosomes (green), suggesting they will in fact be degraded over time. In addition, we tested the kinetics of 1) the Nanotrap binding to the virus and 2) the macrophage engulfment of Nanotraps (Figure 12H). The binding between the pseudovirus and the Nanotraps saturated within an hour ($t_{1/2}$: 9.4 min), whereas the macrophage engulfment did not reach saturation with the Nanotraps until 48 h later ($t_{1/2}$: 1060 min), suggesting that the Nanotraps bind to virus before being engulfed by the macrophages. Finally, we tested whether pro-inflammatory cytokine IL-6 was secreted by the macrophages following the Nanotrap engulfment (Figure 21G). No significant differences were found amongst the following conditions: 1) Macrophages alone 2) Macrophages and Nanotraps 3) Macrophages and Epithelial cells 4) Macrophages, Epithelial cells, and Virus 5) Macrophages, Epithelial Cells, and Nanotraps and 6) Macrophages, Epithelial Cells, Virus, and Nanotraps. These data indicate that the Nanotraps do not promote a proinflammatory response by the macrophages at the treatment dosage.

*Nanotraps Neutralize SARS-CoV-2 infection* in vitro

We next generated multiple types of Nanotraps to test their efficacy. First, avi-tagged biotinylated ACE2 was conjugated to the Nanotrap surface via biotin-streptavidin interactions to make Nanotrap-ACE2. In addition, we synthesized Nanotrap-Antibody by conjugating a SARS-CoV-2 neutralizing

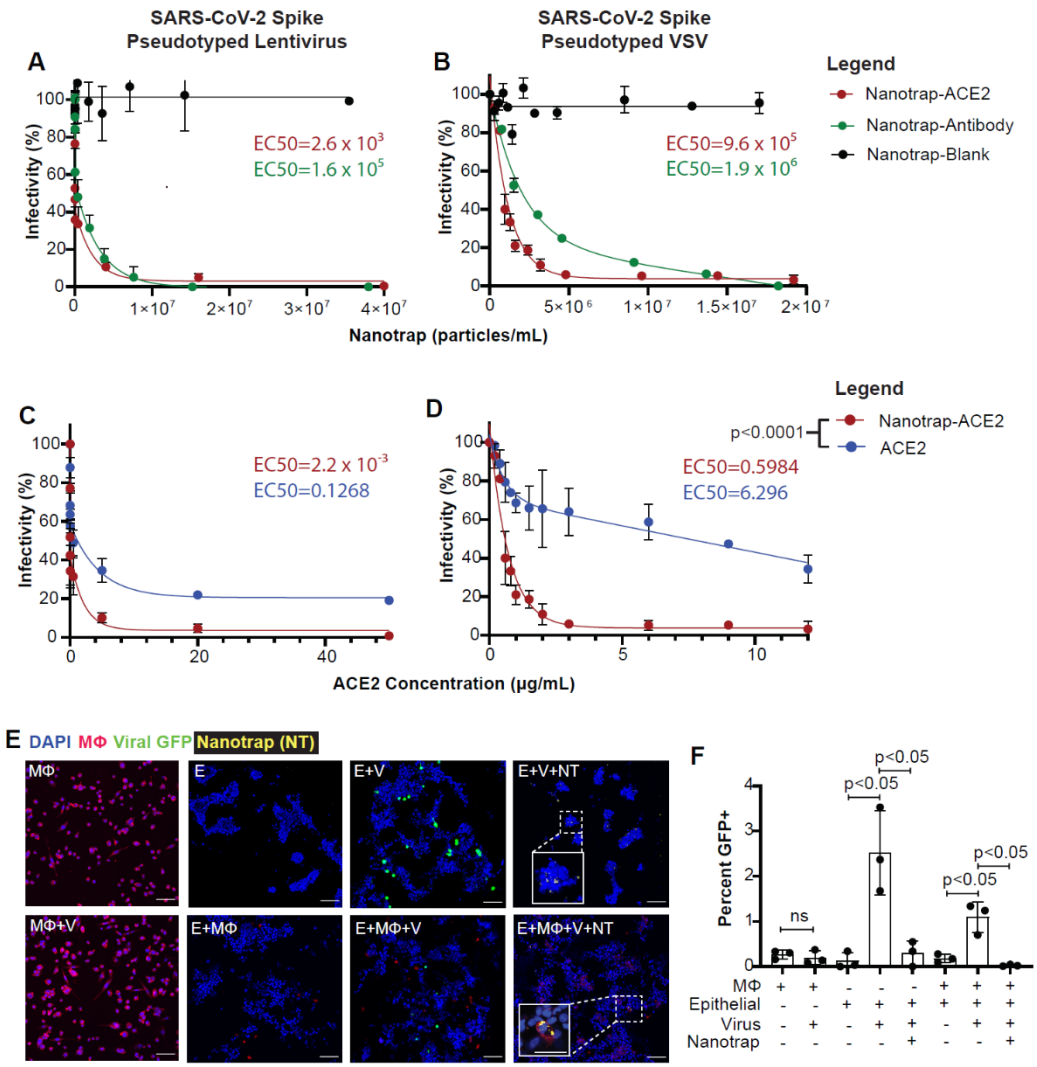


**Figure 13. Inhibition of SARS-CoV-2 viral infection of host cells.** (**A-B**) HEK293T-ACE2 cells were treated with SARS-CoV-2 spike pseudotyped lentivirus (A) or VSV (B) and Nanotrap-ACE2, Nanotrap-Antibody, or Nanotrap-Blank for 72 and 24 h, respectively. Particle densities were counted with a hemocytometer. Data are presented as mean ± SD and fitted with a two-phase decay model. (**C-D**) HEK293T-ACE2 cells were treated with SARS-CoV-2 spike pseudotyped lentivirus (C) or VSV (D) and Nanotrap-ACE2 or soluble ACE2 for 72 and 24 h, respectively. Data are presented as mean ± SD and fitted with a trend curve. For both SARS-CoV-2 spike pseudotyped lentivirus (C) and VSV (D), the Nanotrap-ACE2 and soluble ACE2 curves differ with $p<0.0001$, as tested by sum-of-squares F tests. (**E**) Confocal microscopy of pseudotyped VSV infection (GFP, green) in dTHP1 macrophages (WGA, red) and A549 epithelial cells (DAPI, blue); Nanotrap-ACE2 displayed in yellow. Scale bars represent 100 μm, with inset scale bars representing 40 μm. MΦ: macrophages; V: virus; E: epithelial cells; NT: Nanotraps. (**F**) Quantification of (E). Data are shown as mean ± SD; unpaired t tests were conducted from three independent experiments. This figure is reproduced from Chen, et al., *Matter* 2021.

antibody to the Nanotrap surface via N-hydroxysuccinimide (NHS) esters (see Methods). Finally, in order to test the specificity of the Nanotraps, we made Nanotrap-Blank without a virus-binding epitope.

We next examined whether the Nantraps could effectively capture and contain SARS-CoV-2 *in vitro*. All three Nanotraps were incubated with SARS-CoV-2 spike pseudotyped lentivirus or vesicular stomatitis virus (VSV) for 1 h before adding to HEK293T-ACE2 cells for 24 h and 72 h, respectively. Both Nanotrap-ACE2 and Nanotrap-Antibody completely blocked SARS-CoV-2 pseudovirus infection, while the Nanotrap-Blank did not, indicating both the specificity and functionality of our Nanotraps (Figure 13A-B, Figure 22A-B and Figure 22E). Interestingly, despite that neutralizing antibodies have a higher affinity for spike protein (0.07 nM) than that of ACE2 (22 nM)[261], the Nanotrap-ACE2 blocks SARS-CoV-2 pseudovirus infection more efficiently than the Nanotrap-Antibody. This is most likely due to the lower molecular density (Figure 12H) and the random orientation (Figure 20H) of neutralizing antibody on the Nanotraps than that of the ACE2. Thus, the overall avidity will be lower on the Nanotrap-Antibody than the Nanotrap-ACE2. This could be corrected in future studies by using the higher-efficiency biotin-streptavidin conjugation rather than the NHS-amine conjugation method used here. In sharp contrast to the Nanotraps, soluble recombinant ACE2 protein only partially inhibited infection to HEK293T-ACE2 cells with both SARS-CoV-2 spike pseudotyped lentivirus (Figure 13C and Figure 22C) and VSV (Figure 13D and Figure 22D), despite the previous use of soluble ACE2 protein[222,223].

Macrophages play a key role in controlling SARS-CoV-2 infection[260]. We thus further determined whether human macrophages could efficiently engulf and degrade the virus-bound Nanotraps-ACE2 without becoming infected (Figure 11E-F). Importantly, after incubating SARS-CoV-2 spike pseudotyped VSV with dTHP-1 macrophages for 24 h, no infection was found in the macrophages (Figure 13E-F, comparing "MΦ" with "MΦ +V"). This experiment demonstrated the feasibility of utilizing macrophages to clear the viral infection. We then infected a human lung epithelial cell line A549, which expresses physiological levels of surface ACE2, with SARS-CoV-2 spike pseudotyped VSV in the absence or presence of dTHP-1 macrophages. These data suggest that macrophages significantly

reduced the viral infection but could not completely eradicate it (Figure 13E-F, comparing "E+V" with "E+ MΦ+V"). Finally, we determined whether our engineered Nanotraps triggered phosphatidylserine-mediated phagocytosis by dTHP-1 macrophages for the clearance of virus. After adding Nanotrap-ACE2 into the co-culture of epithelial cells, macrophages, and SARS-CoV-2 spike pseudotyped VSV, the viral infection was completely inhibited (Figure 13E-F, comparing "E+V+NT" and "E+MΦ +V+NT" with "E+MΦ+V"). We further observed incorporation of Nanotrap-ACE2 into the macrophage cell body, but not into the epithelial cells, indicating successful macrophage-specific phagocytosis (Figure 12E, Figure 13E "E+MΦ+V+NT" inset).

In brief summary, our *in vitro* neutralizing experiments demonstrated that our Nanotraps not only served as a sponge to capture and contain SARS-CoV-2, but also utilized the phagocytosis and sterilization machinery of macrophages to defend the host cells from infection, as we depicted in our original experimental design (Figure 11A).

In vivo *Local Delivery to Lungs and Biosafety Profile of Nanotraps in Mice*

In order to assess the safety of Nanotrap treatment, we first examined *in vitro* cytotoxicity on human cell lines. Neither A549 nor HEK293T-ACE2 cells displayed significant cytotoxicity with the addition of Nanotrap-Blank, Nanotrap-ACE2, or Nanotrap-Antibody, as evaluated by a CCK8 cytotoxicity assay (Figure 23A-B).

We next examined the delivery of Nanotraps to mouse lungs and evaluated the biosafety of Nanotraps *in vivo*. We intratracheally injected immunocompetent mice with Nanotrap-ACE2 (labelled with DiD) at a dose of 10 mg/kg. Mice were sacrificed 3 days post-injection. Delivery of Nanotraps to mouse lungs was confirmed with cryosectioned mouse lung tissues: significant Nanotrap accumulation and distribution were found in the lung tissues, particularly in regions around bronchioles in the respiratory tracts. As expected, no Nanotraps were found in the lungs of PBS-treated mice (Figure 14A-B).

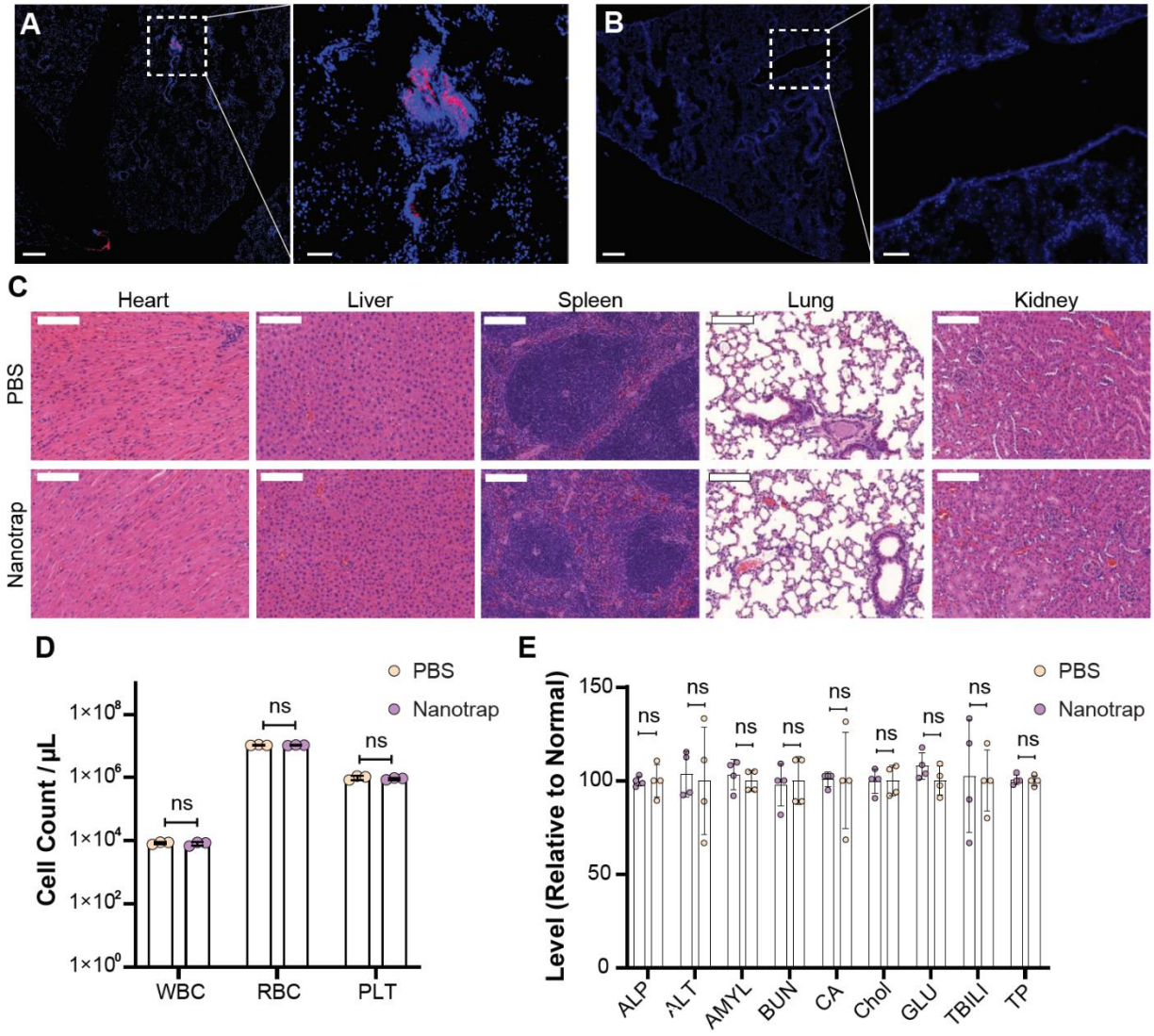


**Figure 14. Murine *in vivo* biosafety profile of Nanotrap treatment.** WT B6 mice were treated intratracheally with 10 mg/kg Nanotrap-ACE2 or PBS for 72 h (n=4, 2 male + 2 female). (**A-B**) Representative fluorescent images of Nanotraps (DiD, red) accumulating in the lung tissues (DAPI, blue) of NT-treated mice (A) or PBS-treated mice (B) 72 h post-intratracheal administration. Scale bars represent 250 µm; inset scale bars represent 50 µm. (**C**) Representative H&E staining of major organs sections, including heart, liver, spleen, lung and kidney. Scale bars represent 500 µm. (**D**) Blood cell counts of white blood cells (WBC), red blood cells (RBC) and platelets (PLT) 72 h after Nanotrap or PBS treatment. Data are shown as mean ± SD; unpaired t tests were conducted from 4 replicates. (**E**) Comprehensive blood chemistry panels comparing Nanotrap- and PBS-treated mice. ALP: alkaline phosphatase; ALT: alanine aminotransferase; AMYL: amylase; BUN: urea nitrogen; CA: calcium; Chol: cholesterol; GLU: glucose; TBIL: total bilirubin; CTP: total protein. This figure is reproduced from Chen, et al., *Matter* 2021.

*In* vivo safety was next analyzed. Hematoxylin and eosin (H&E) staining of major organs including lung, heart, liver, spleen, and kidney showed no histological differences in the Nanotrap-treated mice when compared to the PBS-treated control group (Figure 14C). Furthermore, complete blood counts were performed to evaluate white blood cells (WBCs), red blood cells (RBCs) and platelets (PLTs). The cell counts were similar between Nanotrap- and PBS-treated groups (Figure 4D). Next, comprehensive metabolic panels of mouse blood sera were examined to provide an overall picture of the chemical balance and metabolism. No statistical differences were found between Nanotrap- and PBS-treated mice for glucose levels, electrolyte and fluid balance, kidney function, or liver function (Figure 14E). These results demonstrated the safety of Nanotraps when delivered *in vivo*.

*Therapeutic Efficacy of Nanotraps in* ex vivo *Human Lungs*

We next examined their therapeutic efficacy in inhibiting pseudotyped SARS-CoV-2 infection in healthy, non-transplantable human donor lungs using an *ex vivo* lung perfusion (EVLP) system (Figure 15A and Movie 10. EVLP allows a lung to be perfused and ventilated *ex vivo* after organ retrieval by maintaining lungs at normothermic physiologic conditions and is thus an excellent platform to model lung diseases[255].

The infection potential of the SARS-CoV-2 spike pseudotyped lentivirus at different doses over time in primary human lung cells was first tested *in vitro*, and infection was observed within 8 h (Figure 24A-B). After confirming infection potential, we tested our Nanotraps on an EVLP system with a pair of non-transplantable human lungs. Static lung compliance and oxygenation capacity was measured over time (Figure 24C). SARS-CoV-2 pseudovirus carrying a luciferase reporter gene was injected into the lingula of left upper lung lobe, and pseudovirus plus Nanotrap-Antibody was injected into the right middle lobe; the right upper lung lobe was used as an untreated control (Figure 15C, arrows). Human lung tissue samples were collected after perfusing for 8 h. Single-cell suspensions were generated, and luciferase expression was determined (Figure 15B). The results showed that (1) the pseudovirus infected

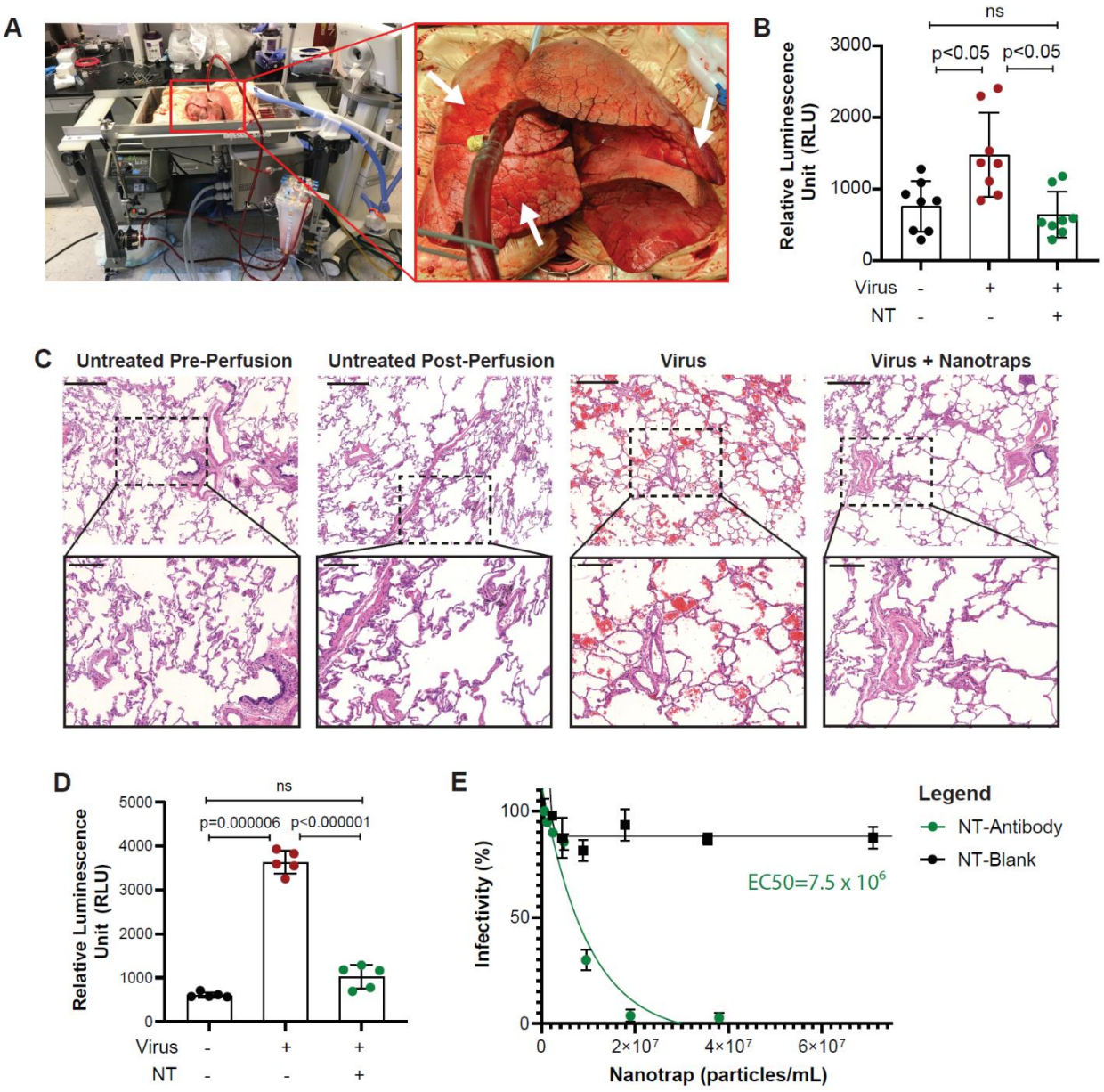


**Figure 15. *Ex vivo* human lung perfusion system for evaluating the neutralizing ability of the Nanotrap-Antibody.** (**A**) Image of human *ex vivo* lung perfusion (EVLP). Arrows indicate untreated (right upper lobe), virus only (right middle lobe), and virus + Nanotrap (lingula) regions. (**B**) Quantification of luciferase expression in EVLP samples 8 h post-infection in three regions indicated in the right panel of A. Data are shown as mean ± SD. (**C**) H&E staining of EVLP. Scale bars represent 500 μm; inset scale bars represent 200 μm. (**D**) Quantification of luciferase expression in *in vitro* primary human cells 48 h post-infection. Data are shown as mean ± SD. (**E**) Vero E6 cells treated with authentic SARS-CoV-2 and Nanotrap-Blank or Nanotrap-Antibody. Particle densities were counted with a hemocytometer. Data are shown as mean ± SD fitted with a trend curve. This figure is reproduced from Chen, et al., *Matter* 2021.

the lung tissues and (2) the Nanotraps completely inhibited the viral infection. Furthermore, H&E staining showed significant RBC infiltration in the virus-treated sample, which was not present in the virus plus Nanotrap-treated region (Figure 15C, Figure 24D-E).

As our EVLP system maintains lung viability for less than 12 h, we treated single-cell suspensions of healthy, untreated lung from the right upper lobe *in vitro* for 48 h to confirm the Nanotraps can function for longer term incubations in human tissue. Again, Nanotrap-Antibody was able to fully inhibit the virus (Figure 15D). Finally, since the EVLP could not be conducted under BSL-3 conditions in order to use authentic SARS-CoV-2, we tested the ability of the Nanotraps to prevent authentic SARS-CoV-2 from infecting Vero E6 cells, which are highly susceptible to SARS-CoV-2 infection[262]. Indeed, Nanotrap-Antibody was able to completely inhibit infection of authentic SARS-CoV-2, as expected (Figure 15E). Importantly, the Nanotrap-Antibody outperformed the soluble antibody in the authentic SARS-CoV-2 infection (Figure 24F, Supplemental Equation 1), despite that this assay cannot show the impact of the phagocytic targeting of our Nanotraps, which should further enhance the virus clearance (Figure 15E-F).

Taken together, our EVLP experiments demonstrated that (1) SARS-CoV-2 pseudovirus can infect human lung, and (2) our newly engineered Nanotraps can completely block the viral infection, thus paving the way for future clinical trials using Nanotraps for the inhibition of SARS-CoV-2 infection.

## CONCLUSIONS

The highly contagious SARS-CoV-2 has caused the global COVID-19 pandemic, so effective and safe treatments are urgently needed. Remdesivir has been approved by the FDA to treat severe COVID-19[263], despite its inconsistent clinical benefits and various reported adverse effects[264,265]. Transfusion of convalescent plasma from recovered patients has shown clinical benefits in some COVID-19 patients[266], however, this approach is challenged by the limited availability of donor plasma and appropriate medical facilities[267]. Simultaneously, tremendous efforts have been devoted to the development of vaccines,

neutralizing antibodies, and other drugs for the prevention and treatment of COVID-19. While recently developed vaccines are being dispersed to the population, safe and effective medicines to treat SARS-CoV-2 infection are largely lacking. For example, Nanosponges have been developed [268], but they cannot completely inhibit infection. They are also not a viable treatment option: as each patient's human leukocyte antigen is different, Nanosponges would have to be personalized for each patient. Large amounts of uninfected primary cells would have to be collected from each patient to make personalized Nanosponges, similar to CAR-T therapy, which has resulted in exorbitant costs and is thus unattainable by many patients[269]. In addition, recombinant soluble ACE2 or ACE2-IgG proteins have been proposed for use as treatments[222,228], but soluble proteins are known to be much more liable to degradation than nanoparticles[270]. Although some existing nanomedicines have been shown to inhibit viral entry[234,235], they do not trigger any specific clearing mechanism, leaving the risk of infection unaddressed. In contrast, our Nanotraps both inhibit cell entry and trigger the phagocytic clearance of the virus. The design of our Nanotraps was inspired by the ability of tumor cells to secrete PD-L1 exosomes, which bind to and suppress T-cell immune functions and thus prevent the killing and clearance of the tumor cells[236,271]. In a similar fashion, the synthetic Nanotraps can mimic the target cells to ensnare the virus. Meanwhile, the synthetic polymer-lipid complexes take advantage of both the stability from polymers and surface flexibility of lipids[272], thereby providing a well-controlled nanomaterial with a high capacity to trap the virus by mimicking target cells. We thus created Nanotraps to bind and inhibit SARS-CoV-2 infection to host cells.

To block the interaction between the SARS-CoV-2 spike protein and the host ACE2 receptors, we coated the Nanotrap surfaces with a high molecular density of either recombinant ACE2 proteins or anti-SARS-CoV-2 neutralizing antibodies (Figure 11A). In principle, the high binding avidity, high diffusivity, and small size of Nanotraps should enable them to easily outcompete low ACE2-expressing host cells in capturing the SARS-CoV-2, thus effectively containing the viruses on their surfaces. Indeed, our experiments demonstrated that viral infection of both pseudotyped and authentic SARS-CoV-2 across

human cell lines, lung primary cells and lung organs can be completely inhibited by Nanotrap-ACE2 or Nanotrap-Antibody (Figure 13 and Figure 15). Notably, Nanotrap-ACE2 was superior to the soluble recombinant ACE2 proteins in containing SARS-CoV-2[222,223], attributing to their high binding avidity (Figure 13C-D). We would also like to note that there are both advantages and disadvantages to bivalent/Fc-containing proteins, such as the antibody, versus monovalent/Fc-free proteins, such as ACE2. For example, bivalent proteins have increased binding capacity per molecule: while we showed that the Nanotrap-Antibody had a lower density than the Nanotrap-ACE2 (Figure 20F), the two Nanotraps still had comparable inhibitory effects (Figure 13A-B). However, it is possible that the Fc region could contribute to the aggravation of COVID-19 due to antibody dependent enhancement[273,274]. Future studies are required to optimize the choice of targeting molecule for human use.

Furthermore, our Nanotraps harness the immune system to clear the SARS-CoV-2 (Figure 12 and Figure 13). By incorporating the phagocyte-specific phosphatidylserine ligands onto the Nanotrap surfaces, macrophages readily engulfed the virus-bound Nanotraps without becoming infected themselves (Figure 13E-F). While macrophages were used as a proof-of-principle in this study, other professional phagocytes such as neutrophils, monocytes, and dendritic cells should be able to similarly clear the virus-bound Nanotraps. In particular, macrophages and dendritic cells are professional antigen presenting cells, which present engulfed antigens to the adaptive immune system[115]. Since the Nanotraps are able to engage antigen presenting cells, it is possible that they may also elicit virus-specific adaptive immune responses. Future studies will evaluate whether Nanotraps can prime adaptive immune responses, thereby promoting vaccine-like protection[275].

In addition, we purposely designed Nanotraps to be biocompatible, biodegradable and safe. The Nanotraps were composed of FDA-approved polymers and lipids, which provides the possibility for safe administration in a clinical setting. Indeed, our biosafety experiments have demonstrated excellent safety profile *in vitro* and *in vivo* (Figure 14).

Lastly, we tested the efficacy of the Nanotraps in a human EVLP system. Superior to lung organoids which cannot reproduce whole-organ response to viral infection[223,276,277], and non-human primate models which are extremely costly[278–280], the EVLP system is a clinically relevant model. We showed that our Nanotraps can completely inhibit viral infection in living human lungs (Figure 15). As current biosafety regulations preclude the testing of authentic SARS-CoV-2 in the EVLP, we further confirmed our Nanotraps can inhibit authentic virus *in vitro* (Figure 15E). These experiments together suggest our Nanotraps could potentially be used to treat SARS-CoV-2 infection in the clinic.

In summary, we developed a new type of potent, effective nanomedicine "Nanotraps" to contain and clear SARS-CoV-2 by harnessing and integrating the power of nanotechnology and immunology. The Nanotraps completely inhibited the SARS-CoV-2 infection to human cells and lung organs. The Nanotraps are effective, biocompatible, safe, stable, feasible for mass production. It is reasonable to hypothesize that the Nanotraps could be easily formulated into a nasal spray or inhaler for easy administration and direct delivery to the respiratory system, or as an oral or ocular liquid, or subcutaneous, intramuscular or intravenous injection to target different sites of SARS-CoV-2 exposure, thus offering flexibility in administration. Furthermore, the design of our Nanotrap is highly versatile: they can be modified to incorporate small molecule drugs or protein/mRNA vaccines to their core, and different human ACE2 recombinant proteins[222,223], human anti-SARS-CoV-2 neutralizing antibodies[224–228], or any developed therapeutic proteins or peptides can be conjugated to the surface, thus easily extending their applications beyond our current study. Overall, we thus expect continuous development of this nanomedicine for clinical use of preventing and treating SARS-CoV-2 infection.

# APPENDIX

The following section includes figures that supplement chapters 3-7.

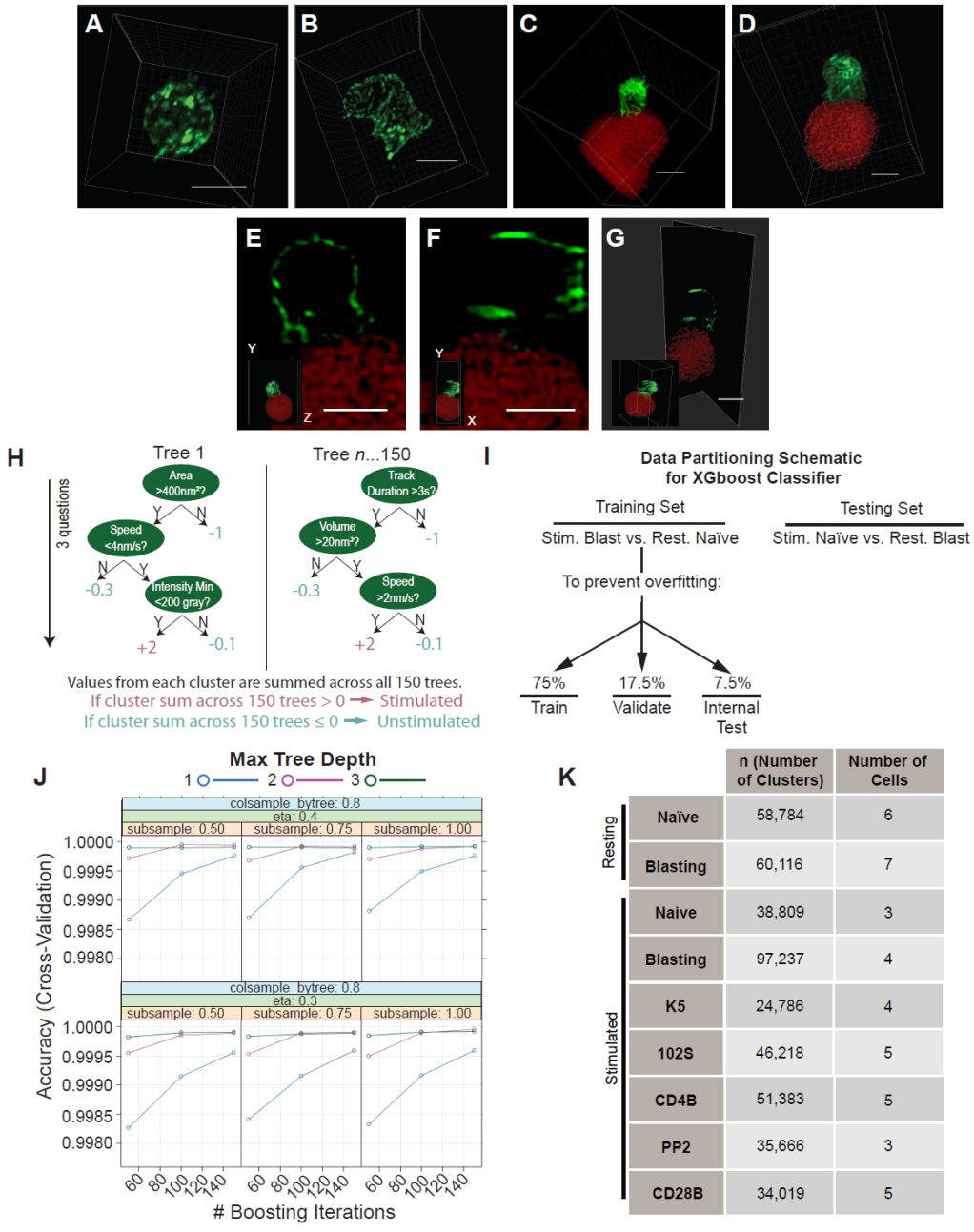


**Figure 16: Training and validation of machine learning using high-dimensional TCR microcluster imaging data.** Caption on next page.

**Figure 16: Training and validation of machine learning using high-dimensional TCR microcluster imaging data.** (**A**) Three-dimensional rendering of a naïve resting $CD4^+$ T cell labeled with Alexa Fluor 488 (AF488)-conjugated anti-TCRβ Fab. Scale bar = 5 μm. See also Supplemental Movie 3. (**B**) Three-dimensional rendering of a blasting resting $CD4^+$ T cell labeled with Alexa Fluor 488 (AF488)-conjugated anti-TCRβ Fab. Scale bar = 5 μm. See also Supplemental Movie 4. (**C**) Three-dimensional rendering of a naïve $CD4^+$ T cell labeled with Alexa Fluor 488 (AF488)-conjugated anti-TCRβ Fab as it encounters an mCherry-CH27 cell loaded with agonist MCC peptide. Scale bar = 5 μm. See also Supplemental Movie 5. (**D**) Three-dimensional rendering of a blasting $CD4^+$ T cell labeled with Alexa Fluor 488 (AF488)-conjugated anti-TCRβ Fab as it encounters an mCherry-CH27 cell loaded with agonist MCC peptide. Scale bar = 5 μm. See also Supplemental Movie 6. (**E**-**G**) XY (**E**), YX (**F**), or dual (**G**) orthogonal slices of a representative $CD4^+$ T cell labeled with Alexa Fluor 488 (AF488)-conjugated anti-TCRβ Fab as it encounters an mCherry-CH27 cell loaded with agonist MCC peptide. Inset is a reference frame of the whole cell. Scale bars = 5 μm. (**H**) Cartoon describing decision tree ensemble structure and prediction algorithm used in XGboost binary classifier. (**I**) Schematic detailing data partitioning for XGboost classifier. (**J**) Diagram showing tuning of hyper-parameters during the training of the XGboost model. (**K**) Numbers of TCR microclusters from each cell used for XGboost classification and UMAP production. This figure is reproduced from Rosenberg, et al., *Cell Systems* 2020.

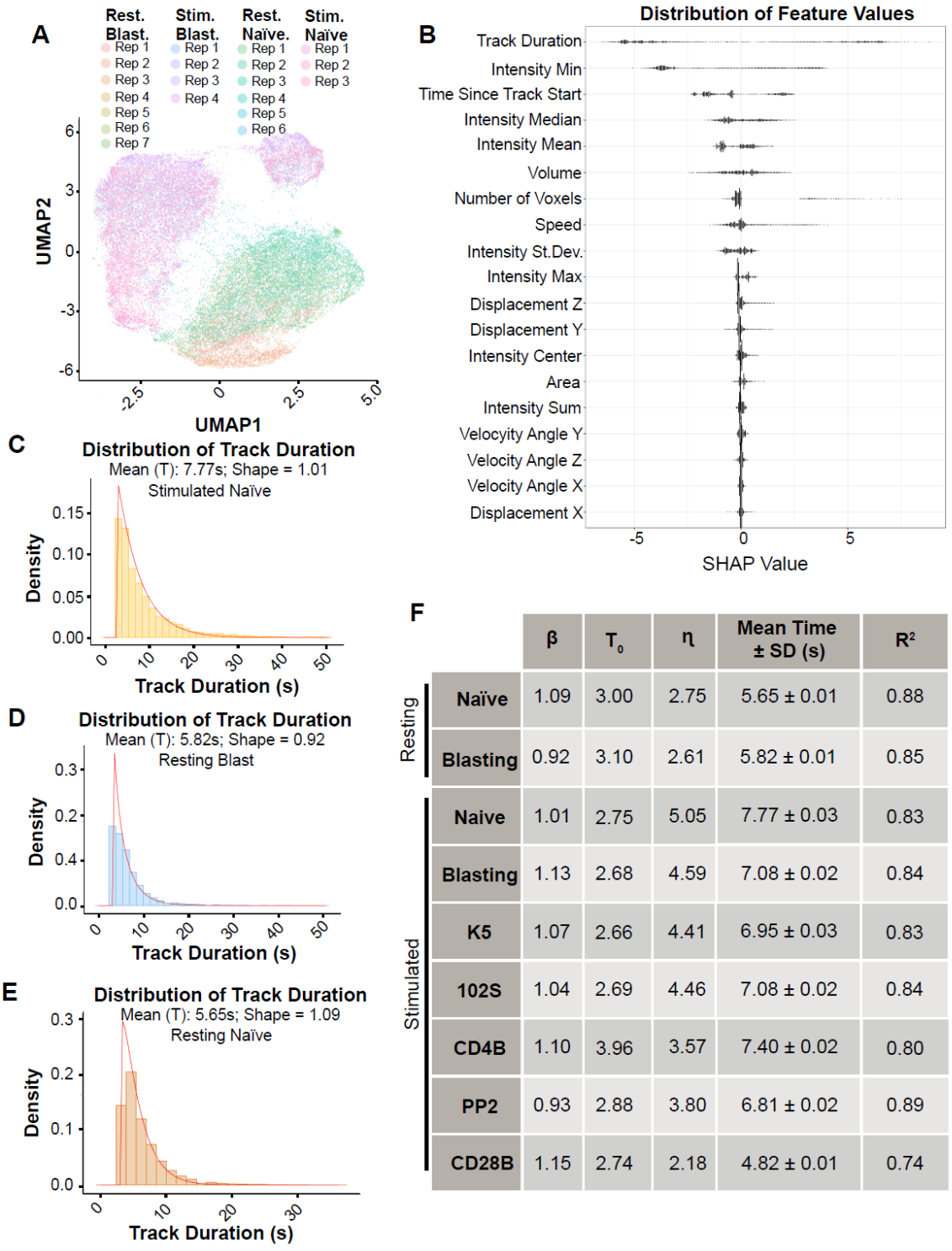


**F**

| | | β | $T_0$ | η | Mean Time ± SD (s) | $R^2$ |
|---|---|---|---|---|---|---|
| Resting | Naïve | 1.09 | 3.00 | 2.75 | 5.65 ± 0.01 | 0.88 |
| | Blasting | 0.92 | 3.10 | 2.61 | 5.82 ± 0.01 | 0.85 |
| Stimulated | Naive | 1.01 | 2.75 | 5.05 | 7.77 ± 0.03 | 0.83 |
| | Blasting | 1.13 | 2.68 | 4.59 | 7.08 ± 0.02 | 0.84 |
| | K5 | 1.07 | 2.66 | 4.41 | 6.95 ± 0.03 | 0.83 |
| | 102S | 1.04 | 2.69 | 4.46 | 7.08 ± 0.02 | 0.84 |
| | CD4B | 1.10 | 3.96 | 3.57 | 7.40 ± 0.02 | 0.80 |
| | PP2 | 0.93 | 2.88 | 3.80 | 6.81 ± 0.02 | 0.89 |
| | CD28B | 1.15 | 2.74 | 2.18 | 4.82 ± 0.01 | 0.74 |

**Figure 17: UMAP, SHAP values, and Weibull distribution fitting.** (**A**) UMAP from Fig. 2H color-coded by cell replicate. (**B**) Distribution of SHAP values of microclusters from Fig. 2J. (**C**-**E**) Weibull distribution fitting of microcluster track duration from stimulated naïve cells (**C**), resting blasting cells (**D**), and resting naïve cells (**E**). See also Fig. 2L. (**F**) Table of β, $T_0$, η, and mean duration obtained by Weibull distribution fittings of microcluster track durations from each cell group. Duration are presented as mean ± standard deviation (SD) and the goodness of fit was indicated by $R^2$ values. This figure is reproduced from Rosenberg, et al., *Cell Systems* 2020.

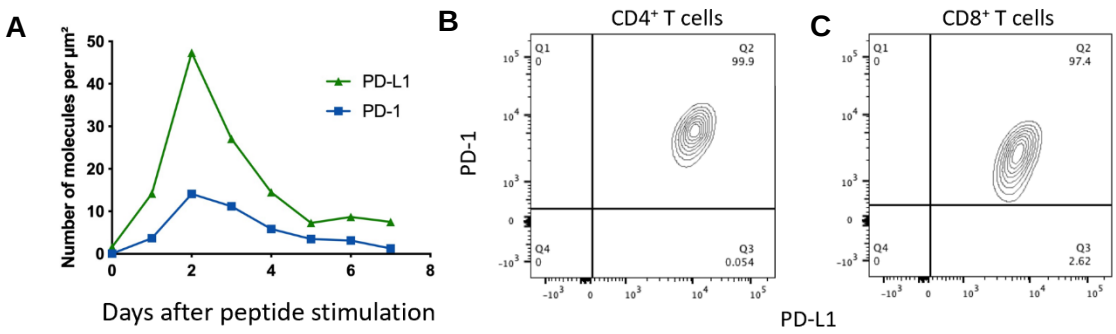


**Figure 18: PD-1/PD-L1 co-expression on primary T cells. (A).** Time course of PD-1 and PD-L1 expressions after antigen stimulation on primary $CD4^+$ T cells. **(B-C).** PD-1/PD-L1 co-expression on primary 5C.C7 $CD4^+$ T cells (B) and OT-I $CD8^+$ T cells (C) after 2 days' antigen stimulation. These data were produced by Chufan Cai.

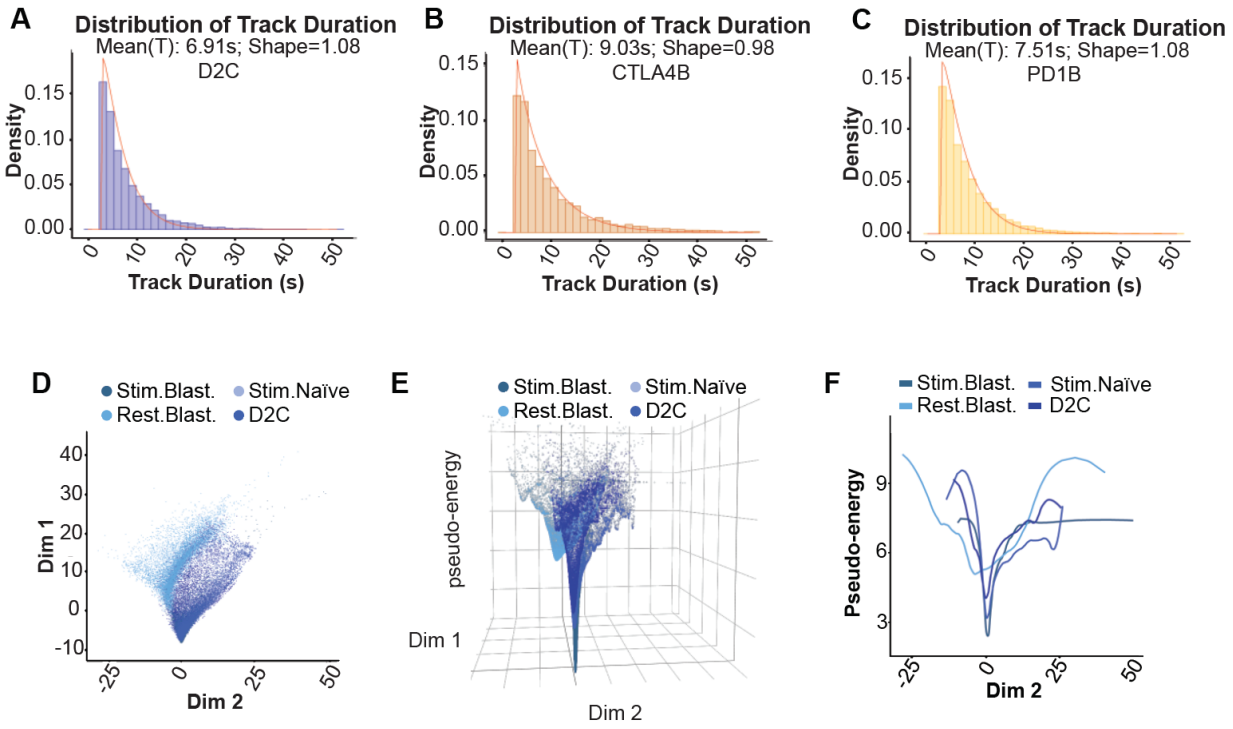


**Figure 19: Checkpoint Blockade Supplemental Data.** (**A**) UMAP from Fig. 2H color-coded by cell replicate. (**B**) Distribution of SHAP values of microclusters from Fig. 2J. (**A-C**) Weibull distribution fitting of microcluster track duration from day 2 stimulated control cells (**A**), stimulated blasting cells treated with CTLA-4 Blockade (**B**), and stimulated blasting cells treated with PD-1 Blockade (**C**). See also Fig. 5. (**D**) Diffusion map of stimulated blasting cells, resting blasting cells, stimulated naïve cells, and day 2 stimulated control cells. (**E**) Pseudo-engergy map of stimulated blasting cells, resting blasting cells, stimulated naïve cells, and day 2 stimulated control cells. (**F**) 2D projection of pseudo-engergy map of stimulated blasting cells, resting blasting cells, stimulated naïve cells, and day 2 stimulated control cells. This figure is reproduced from Rosenberg, et al., *Cell Systems* 2020.

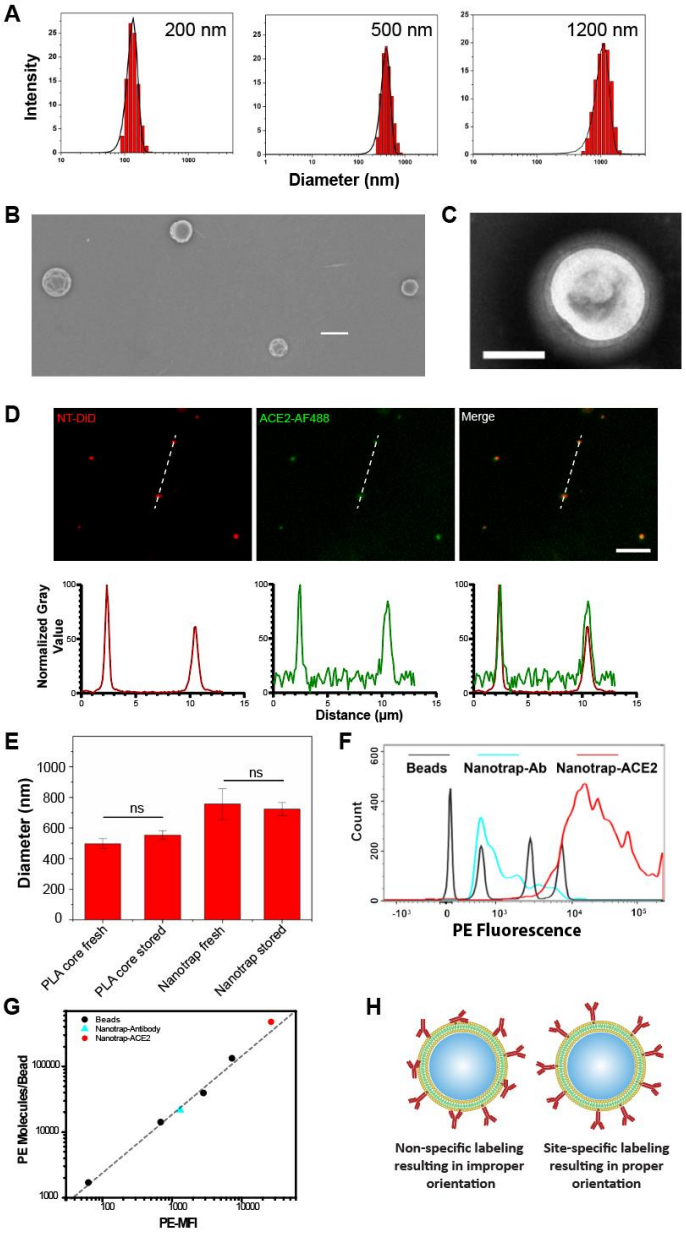


**Figure 20. Supplemental synthesis, and characterization of Nanotraps for SARS-CoV-2**. (**A**) Dynamic light scattering measurements of Nanotraps constructed of 200 nm (left), 500 nm (middle), and 1200 nm (right) sizes. (**B**) SEM image of dispersion of Nanotraps (500 nm) without virus. Scale bar represents 1 μm. (**C**) TEM image of a Nanotrap particle showing the core-shell structure. Scale bar represents 250 nm. (**D**) Fluorescent images of Nanotraps with PLA polymeric core (DiD, red) and ACE2 (anti-ACE2-AF488, green) that had been stored at -20°C for six months. Scale bar represents 5 μm. Dotted lines represent displayed plot profile below. (**E**) Dynamic light scattering measurements comparing freshly made PLA core or functionalized Nanotraps with PLA core or functionalized Nanotraps that had been lyophilized, sealed, and stored at -20°C for six months. (**F**) Histogram displaying PE Quantibrite Beads (BD Biosciences, black), Nanotrap-Antibody labeled with anti-IgG-PE (cyan), and Nanotrap-ACE2 labeled with anti-ACE2-PE (red). (**G**) Average surface density calculated following manufacturer's instructions. The average surface densities are calculated as $(3.59\pm0.43)\times10^5$ ACE2 molecules per Nanotrap-ACE2, and $(2.47\pm0.21)\times10^4$ neutralizing antibodies per Nanotrap-Antibody. (**H**) Scheme demonstrating orientation of antibodies resultant of NHS-amine conjugation (left) versus biotin-streptavidin conjugation (right). This figure is reproduced from Chen, et al., *Matter* 2021.

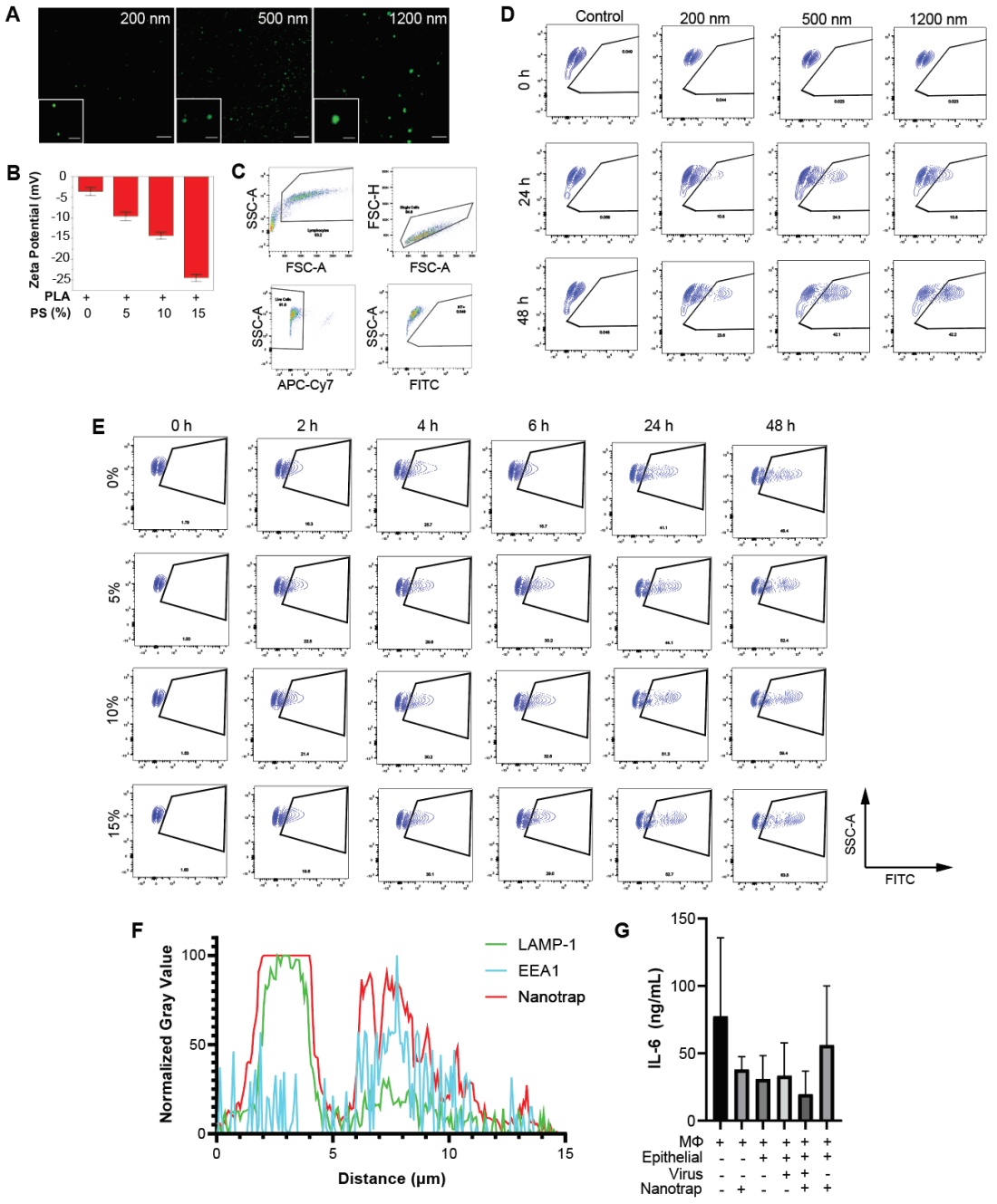


**Figure 21. Supplemental phagocytosis of Nanotraps by macrophages.** (**A**) Epifluorescent images of varying sizes of Nanotraps (DiO, green). (**B**) Measured zeta potentials of Nanotraps with varying PS ratios. (**C**) Gating strategy of the flow cytometry shown in Fig. 12A-D. APC-Cy7 represents live/dead, and FITC represents DiO (Nanotraps). (**D**) Contour plots of the flow cytometry of macrophages phagocytosing Nanotraps of various sizes at 0h (top), 24 h (middle) and 48 h (bottom). See also Fig. 12A-B. (**E**) Contour plots of the flow cytometry of macrophages phagocytosing Nanotraps made with varying levels of phosphatidylserine. See also Fig. 12C-D. (**F**) Normalized plot profile of fluorescent signal alone dotted line shown in Fig. 12G. (**G**) IL-6 ELISA conducted on supernatant from macrophages with or without lung epithelial cells, SARS-CoV-2 pseudovirus, or Nanotraps. No significant statistical differences were found between any groups. This figure is reproduced from Chen, et al., *Matter* 2021.

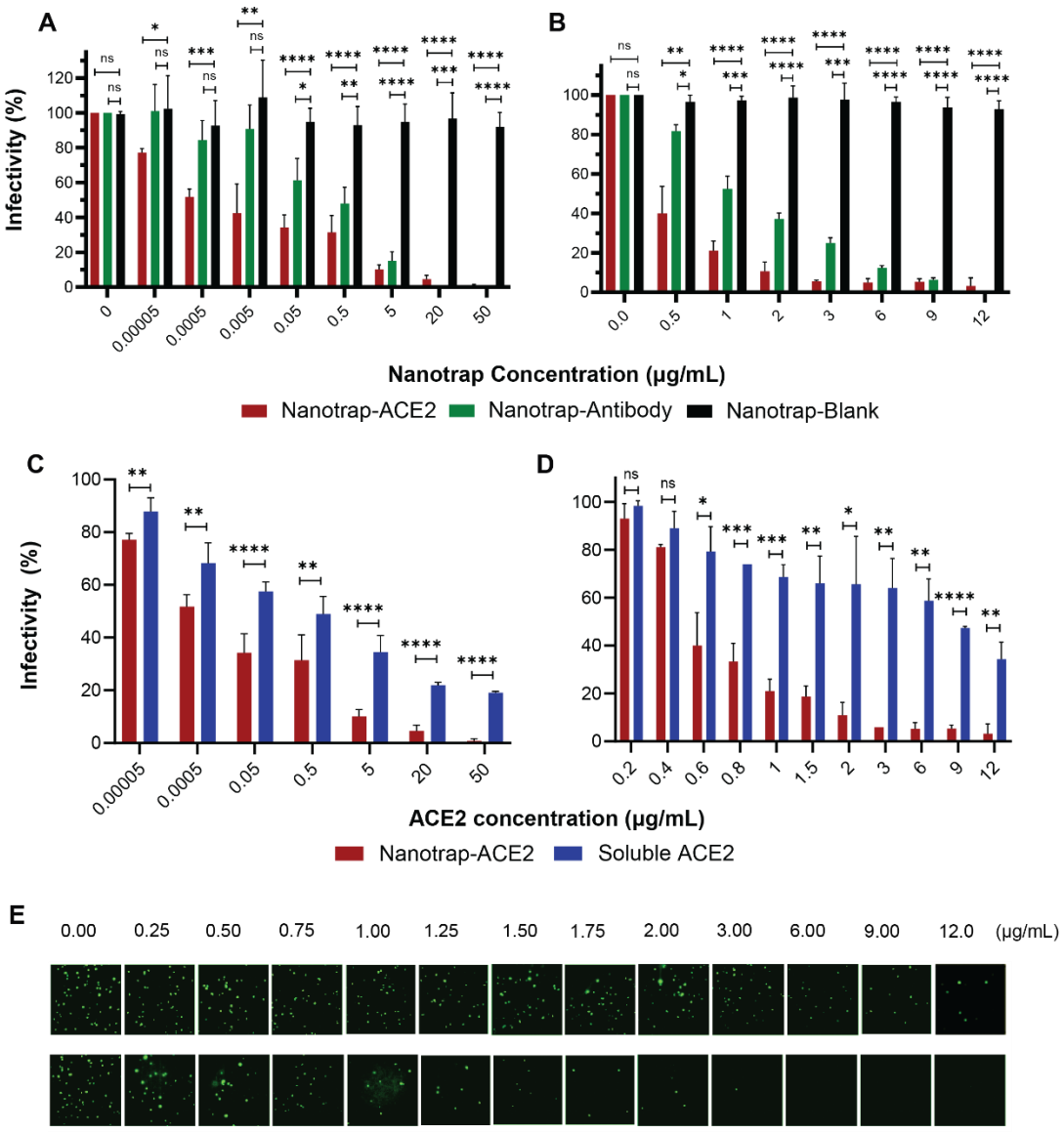


**Figure 22. Supplemental inhibition of SARS-CoV-2 pseudovirus in HEK293T-ACE2 cells**. (**A-B**) HEK293T-ACE2 cells were treated with SARS-CoV-2 spike pseudotyped lentivirus (A) or VSV (B) and Nanotrap-ACE2, Nanotrap-Antibody, or Nanotrap-Blank for 72 and 24 h, respectively. Data are presented as mean ± SD; unpaired t tests were conducted on three independent replicates. (**C-D**) HEK293T-ACE2 cells were treated with SARS-CoV-2 spike pseudotyped lentivirus (C) or VSV (D) and Nanotrap-ACE2 or soluble ACE2 for 72 and 24 h, respectively. Data are presented as mean ± SD; unpaired t tests were conducted on three independent replicates. (**E**) Representative fluorescent images of VSV-GFP pseudovirus infected HEK293T-ACE2 cells after treatment with ACE2 protein (top) and Nanotraps-ACE2 (bottom). *p < 0.05, **p < 0.005, ***p<0.0005, ****p<0.00005. N = 3 per group. This figure is reproduced from Chen, et al., *Matter* 2021.

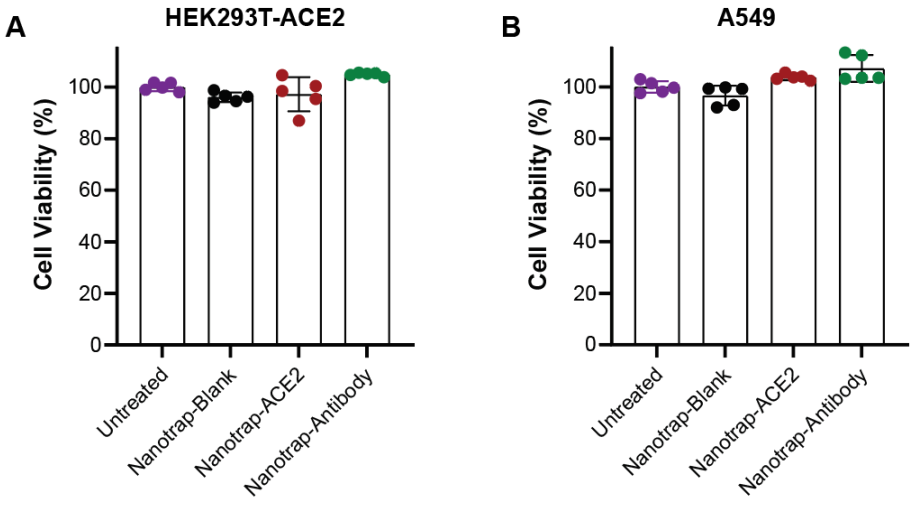


**Figure 23. *In vitro* biosafety profile of Nanotrap treatment.** (**A**-**B**) Viability of HEK293T-ACE2 (A) and A549 (B) cells with Nanotrap treatments for 72 h. Data are presented as mean ± SD; n = 5 per group. This figure is reproduced from Chen, et al., *Matter* 2021.

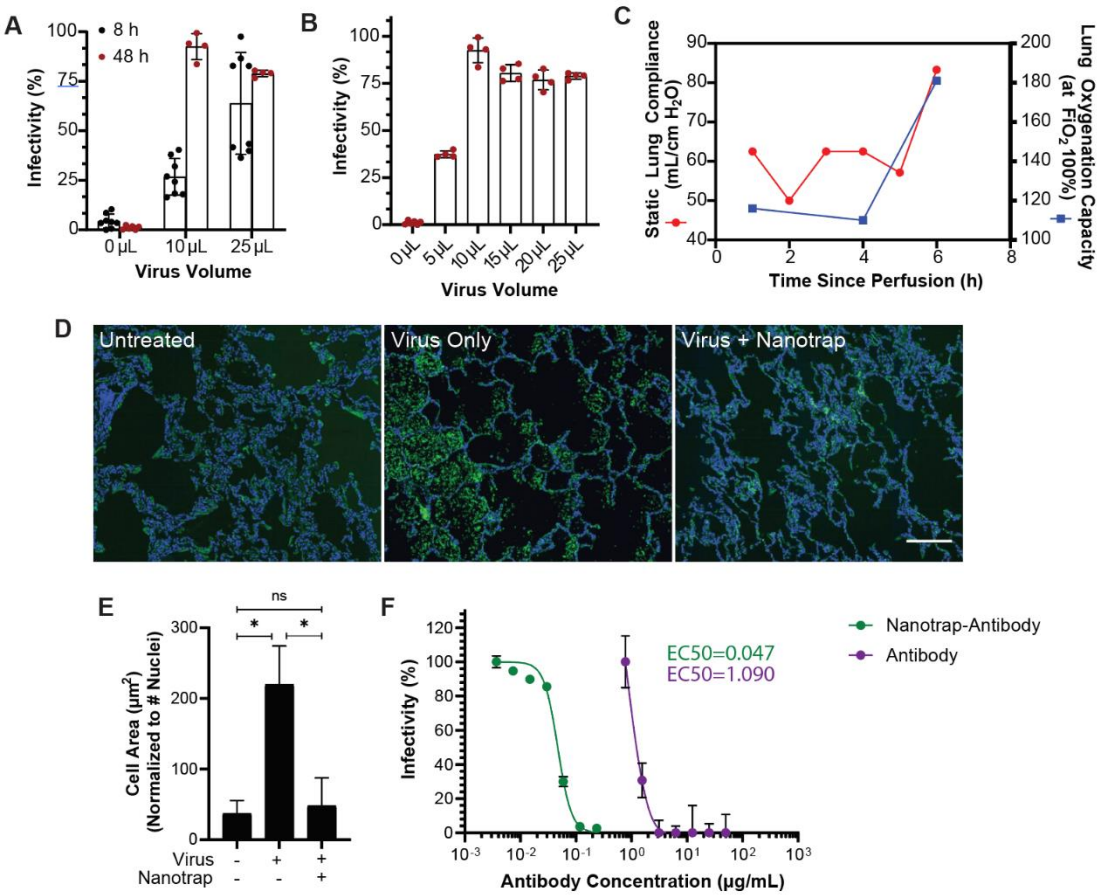


**Figure 24. EVLP perfusion system for evaluating the neutralizing ability of the Nanotraps.** (**A**) SARS-CoV-2 pseudotyped lentivirus infectivity of primary human cells *in vitro* 8 or 48 h post infection. (**B**) SARS-CoV-2 pseudotyped lentivirus infectivity of primary human cells *in vitro* 48 h post infection. (**C**) Quantification of lung compliance and oxygenation capacity while on EVLP. (**D**) Fluorescent images of *ex vivo* lung tissue sections stained with DAPI and imaged with 488 nm and 560 nm wavelengths. Scale bar represents 200 µm. (**E**) Quantification of fluorescence images in (D). Auto-fluorescence from the 560-nm wavelength channel was quantified and normalized to signal from 488-nm wavelength. (**F**) Vero E6 cells treated with authentic SARS-CoV-2 and Nanotrap-Antibody or soluble neutralizing antibody. Antibody concentrations on Nanotrap-antibody were calculated by multiplying the particle concentration per mL with antibody density per particle measured in Figure 20F (see Equation 1). Data are shown as mean ± SD fitted with a trend curve. This figure is reproduced from Chen, et al., *Matter* 2021.

# REFERENCES


1. (1957). *Microscopy apparatus* (1957).

2. Minsky, M. (1988). Memoir on inventing the confocal scanning microscope. Scanning **10**, 128–138 10.1002/sca.4950100403.

3. Elliott, A. D. (2020). Confocal Microscopy: Principles and Modern Practices. Curr. Protoc. Cytom. **92**, e68 10.1002/cpcy.68.

4. Fish, K. N. (2009). Total internal reflection fluorescence (TIRF) microscopy. Current Protocols in Cytometry vol. 0 12 Unit12.18 10.1002/0471142956.cy1218s50.

5. Axelrod, D., Burghardt, T. P. & Thompson, N. L. (1984). *TOTAL INTERNAL REFLECTION FLUORESCENCE* www.annualreviews.org (1984).

6. Al-Aghbar, M. A., Chu, Y. S., Chen, B. M. & Roffler, S. R. (2018). High-affinity ligands can trigger T cell receptor signaling without CD45 segregation. Front. Immunol. **9**, 10.3389/fimmu.2018.00713.

7. Balagopalan, L., Yi, J., Nguyen, T., McIntire, K. M., Harned, A. S., Narayan, K. & Samelson, L. E. (2018). Plasma membrane LAT activation precedes vesicular recruitment defining two phases of early T-cell activation. Nat. Commun. **9**, 10.1038/s41467-018-04419-x.

8. Sasmal, D. K., Feng, W., Roy, S., Leung, P., He, Y., Cai, C., Cao, G., Lian, H., Qin, J., Hui, E., *et al.* (2020). TCR–pMHC bond conformation controls TCR ligand discrimination. Cell. Mol. Immunol. **17**, 203–217 10.1038/s41423-019-0273-6.

9. Hashimoto-Tane, A., Yokosuka, T. & Saito, T. (2017). Analyzing the dynamics of signaling microclusters. in Methods in Molecular Biology vol. 1584 51–64 (Humana Press Inc., 2017). 10.1007/978-1-4939-6881-7_4.

10. Crites, T. J., Chen, L. & Varma, R. (2012). A TIRF microscopy technique for real-time, simultaneous imaging of the TCR and its associated signaling proteins. J. Vis. Exp. doi:10.3791/3892 10.3791/3892.

11. Klar, T. A. & Hell, S. W. (1999). Subdiffraction resolution in far-field fluorescence microscopy. Opt. Lett. **24**, 954 10.1364/ol.24.000954.

12. Hell, S. W. & Wichmann, J. (1994). Breaking the diffraction resolution limit by stimulated emission: stimulated-emission-depletion fluorescence microscopy. Opt. Lett. **19**, 780 10.1364/ol.19.000780.

13. Schrof, S., Staudt, T., Rittweger, E., Wittenmayer, N., Dresbach, T., Engelhardt, J. & Hell, S. W. (2011). STED nanoscopy with mass-produced laser diodes. Opt. Express **19**, 8066 10.1364/oe.19.008066.

14. Göttfert, F., Wurm, C. A., Mueller, V., Berning, S., Cordes, V. C., Honigmann, A. & Hell, S. W. (2013). Coaligned dual-channel STED nanoscopy and molecular diffusion analysis at 20 nm resolution. Biophys. J. **105**, L01–L03 10.1016/j.bpj.2013.05.029.

15. Guerra, J. M. (1995). Super-resolution through illumination by diffraction-born evanescent waves. Appl. Phys. Lett. **66**, 3555–3557 10.1063/1.113814.

16. Gustafsson, M. G. L. (2005). Nonlinear structured-illumination microscopy: Wide-field fluorescence imaging with theoretically unlimited resolution. Proc. Natl. Acad. Sci. U. S. A. **102**, 13081–13086 10.1073/pnas.0406877102.

17. Rust, M. J., Bates, M. & Zhuang, X. (2006). Sub-diffraction-limit imaging by stochastic optical reconstruction microscopy (STORM). Nat. Methods **3**, 793–796 10.1038/nmeth929.

18. Betzig, E., Patterson, G. H., Sougrat, R., Lindwasser, O. W., Olenych, S., Bonifacino, J. S., Davidson, M. W., Lippincott-Schwartz, J. & Hess, H. F. (2006). Imaging intracellular fluorescent proteins at nanometer resolution. Science (80-. ). **313**, 1642–1645 10.1126/science.1127344.

19. Hess, S. T., Girirajan, T. P. K. & Mason, M. D. (2006). Ultra-high resolution imaging by fluorescence photoactivation localization microscopy. Biophys. J. **91**, 4258–4272 10.1529/biophysj.106.091116.

20. Williamson, D. J., Owen, D. M., Rossy, J., Magenau, A., Wehrmann, M., Gooding, J. J. & Gaus, K. (2011). Pre-existing clusters of the adaptor Lat do not participate in early T cell signaling events. Nat. Immunol. **12**, 655–662 10.1038/ni.2049.

21. Diercks, B. P., Werner, R., Weidemüller, P., Czarniak, F., Hernandez, L., Lehmann, C., Rosche, A., Krüger, A., Kaufmann, U., Vaeth, M., *et al.* (2018). ORAI1, STIM1/2, and RYR1 shape subsecond Ca 2+ microdomains upon T cell activation. Sci. Signal. **11**, 10.1126/scisignal.aat0358.

22. Felce, J. H., Parolini, L., Sezgin, E., Céspedes, P. F., Korobchevskaya, K., Jones, M., Peng, Y., Dong, T., Fritzsche, M., Aarts, D., *et al.* (2021). Single-Molecule, Super-Resolution, and Functional Analysis of G Protein-Coupled Receptor Behavior Within the T Cell Immunological Synapse. Front. Cell Dev. Biol. **8**, 10.3389/fcell.2020.608484.

23. Rossboth, B., Arnold, A. M., Ta, H., Platzer, R., Kellner, F., Huppa, J. B., Brameshuber, M., Baumgart, F. & Schütz, G. J. (2018). TCRs are randomly distributed on the plasma membrane of resting antigen-experienced T cells. Nat. Immunol. **19**, 821–827 10.1038/s41590-018-0162-7.

24. Barr, V. A., Yi, J. & Samelson, L. E. (2017). Super-resolution analysis of TCR-dependent signaling: Single-molecule localization microscopy. in Methods in Molecular Biology vol. 1584 183–206 (Humana Press Inc., 2017). 10.1007/978-1-4939-6881-7_13.

25. Chen, B. C., Legant, W. R., Wang, K., Shao, L., Milkie, D. E., Davidson, M. W., Janetopoulos, C., Wu, X. S., Hammer, J. A., Liu, Z., *et al.* (2014). Lattice light-sheet microscopy: Imaging molecules to embryos at high spatiotemporal resolution. Science (80-. ). doi:10.1126/science.1257998 10.1126/science.1257998.

26. Rosenberg, J. & Huang, J. (2020). Visualizing Surface T-Cell Receptor Dynamics Four-Dimensionally Using Lattice Light-Sheet Microscopy. J. Vis. Exp. e59914 doi:10.3791/59914 10.3791/59914.

27. Ellefsen, K. L. & Parker, I. (2018). Dynamic Ca2+ imaging with a simplified lattice light-sheet microscope: A sideways view of subcellular Ca2+ puffs. Cell Calcium **71**, 34–44 10.1016/j.ceca.2017.11.005.

28. Gao, R., Asano, S. M., Upadhyayula, S., Pisarev, I., Milkie, D. E., Liu, T.-L., Singh, V., Graves, A., Huynh, G. H., Zhao, Y., *et al.* (2019). Cortical column and whole-brain imaging with molecular contrast and nanoscale resolution. Science **363**, eaau8302 10.1126/science.aau8302.

29. Cai, E., Marchuk, K., Beemiller, P., Beppler, C., Rubashkin, M. G., Weaver, V. M., Gérard, A., Liu, T. L., Chen, B. C., Betzig, E., *et al.* (2017). Visualizing dynamic microvillar search and stabilization during ligand detection by T cells. Science (80-. ). **356**, 10.1126/science.aal3118.

30. Mir, M., Stadler, M. R., Ortiz, S. A., Hannon, C. E., Harrison, M. M., Darzacq, X. & Eisen, M. B. (2018). Dynamic multifactor hubs interact transiently with sites of active transcription in drosophila embryos. Elife **7**, 10.7554/eLife.40497.

31. Cai, E., Marchuk, K., Beemiller, P., Beppler, C., Rubashkin, M. G., Weaver, V. M., Gérard, A., Liu, T.-L., Chen, B.-C., Betzig, E., *et al.* (2017). Visualizing dynamic microvillar search and stabilization during ligand detection by T cells. Science **356**, eaal3118 10.1126/science.aal3118.

32. McArthur, K., Whitehead, L. W., Heddleston, J. M., Li, L., Padman, B. S., Oorschot, V., Geoghegan, N. D., Chappaz, S., Davidson, S., Chin, H. S., *et al.* (2018). BAK/BAX macropores facilitate mitochondrial herniation and mtDNA efflux during apoptosis. Science (80-. ). **359**, eaao6047 10.1126/science.aao6047.

33. Rosenberg, J., Cao, G., Borja-Prieto, F. & Huang, J. (2020). Lattice Light-Sheet Microscopy Multi-dimensional Analyses (LaMDA) of T-Cell Receptor Dynamics Predict T-Cell Signaling States. Cell Syst. **10**, 433-444.e5 10.1016/j.cels.2020.04.006.

34. Mir, M., Reimer, A., Stadler, M., Tangara, A., Hansen, A. S., Hockemeyer, D., Eisen, M. B., Garcia, H. & Darzacq, X. (2018). Single molecule imaging in live embryos using lattice light-sheet microscopy. in Methods in Molecular Biology vol. 1814 541–559 (Humana Press Inc., 2018). 10.1007/978-1-4939-8591-3_32.

35. Chen, C. Y., Liu, Y. T., Lu, C. H., Lee, P. Y., Tsai, Y. C., Wu, J. S., Chen, P. & Chen, B. C. (2019). The applications of lattice light-sheet microscopy for functional volumetric imaging of hippocampal neurons in a three-dimensional culture system. Micromachines **10**, 10.3390/mi10090599.

36. O'Shaughnessy, E. C., Stone, O. J., LaFosse, P. K., Azoitei, M. L., Tsygankov, D., Heddleston, J. M., Legant, W. R., Wittchen, E. S., Burridge, K., Elston, T. C., *et al.* (2019). Software for lattice light-sheet imaging of FRET biosensors, illustrated with a new Rap1 biosensor. J. Cell Biol. **218**, 3153–3160 10.1083/jcb.201903019.

37. Phillips, J. K., Sherman, S. A., Cotton, K. Y., Heddleston, J. M., Taylor, A. B. & Finan, J. D. (2019). Characterization of neurite dystrophy after trauma by high speed structured illumination microscopy and lattice light sheet microscopy. J. Neurosci. Methods **312**, 154–161 10.1016/j.jneumeth.2018.12.005.

38. Schöneberg, J., Dambournet, D., Liu, T.-L., Forster, R., Hockemeyer, D., Betzig, E. & Drubin, D. G. (2018). 4D cell biology: big data image analytics and lattice light-sheet imaging reveal dynamics of clathrin-mediated endocytosis in stem cell-derived intestinal organoids. Mol. Biol. Cell **29**, 2959–2968 10.1091/mbc.E18-06-0375.

39. Gao, L., Tang, W.-C., Tsai, Y.-C. & Chen, B.-C. (2019). Lattice light sheet microscopy using

tiling lattice light sheets. Opt. Express **27**, 1497–1506 10.1364/OE.27.001497.

40. Legant, W. R., Shao, L., Grimm, J. B., Brown, T. A., Milkie, D. E., Avants, B. B., Lavis, L. D. & Betzig, E. (2016). High-density three-dimensional localization microscopy across large volumes. Nat. Methods doi:10.1038/nmeth.3797 10.1038/nmeth.3797.

41. ZEISS Lattice Lightsheet 7. https://www.zeiss.com/microscopy/int/products/imaging-systems/lattice-lightsheet-7.html.

42. Liu, T. L., Upadhyayula, S., Milkie, D. E., Singh, V., Wang, K., Swinburne, I. A., Mosaliganti, K. R., Collins, Z. M., Hiscock, T. W., Shea, J., *et al.* (2018). Observing the cell in its native state: Imaging subcellular dynamics in multicellular organisms. Science (80-. ). doi:10.1126/science.aaq1392 10.1126/science.aaq1392.

43. Castellino, F. & Germain, R. N. (2006). Cooperation between CD4+ and CD8+ T cells: When, where, and how. Annual Review of Immunology vol. 24 519–540 10.1146/annurev.immunol.23.021704.115825.

44. Laidlaw, B. J., Craft, J. E. & Kaech, S. M. (2016). The multifaceted role of CD4+ T cells in CD8+ T cell memory. Nature Reviews Immunology vol. 16 102–111 10.1038/nri.2015.10.

45. Mempel, T. R., Henrickson, S. E. & Von Andrian, U. H. (2004). T-cell priming by dendritic cells in lymph nodes occurs in three distinct phases. Nature **427**, 154–159 10.1038/nature02238.

46. Kaech, S. M. & Cui, W. (2012). Transcriptional control of effector and memory CD8+ T cell differentiation. Nature Reviews Immunology vol. 12 749–761 10.1038/nri3307.

47. MacLeod, M. K. L., Clambey, E. T., Kappler, J. W. & Marrack, P. (2009). CD4 memory T cells: What are they and what can they do? Seminars in Immunology vol. 21 53–61 10.1016/j.smim.2009.02.006.

48. Gallimore, A., Glithero, A., Godkin, A., Tissot, A. C., Plückthun, A., Elliott, T., Hengartner, H. & Zinkernagel, R. (1998). Induction and exhaustion of lymphocytic choriomeningitis virus-specific cytotoxic T lymphocytes visualized using soluble tetrameric major histocompatibility complex class I-peptide complexes. J. Exp. Med. **187**, 1383–1393 10.1084/jem.187.9.1383.

49. Virgin, H. W., Wherry, E. J. & Ahmed, R. (2009). Redefining Chronic Viral Infection. Cell vol. 138 30–50 10.1016/j.cell.2009.06.036.

50. McLane, L. M., Abdel-Hakeem, M. S. & Wherry, E. J. (2019). CD8 T Cell Exhaustion During Chronic Viral Infection and Cancer. Annual Review of Immunology vol. 37 457–495 10.1146/annurev-immunol-041015-055318.

51. Barber, D. L., Wherry, E. J., Masopust, D., Zhu, B., Allison, J. P., Sharpe, A. H., Freeman, G. J. & Ahmed, R. (2006). Restoring function in exhausted CD8 T cells during chronic viral infection. Nature **439**, 682–687 10.1038/nature04444.

52. Zhao, Y., Harrison, D. L., Song, Y., Ji, J., Huang, J. & Hui, E. (2018). Antigen-Presenting Cell-Intrinsic PD-1 Neutralizes PD-L1 in cis to Attenuate PD-1 Signaling in T Cells. Cell Rep. **24**, 379-390.e6 10.1016/J.CELREP.2018.06.054.

53. Blank, C. U., Haining, W. N., Held, W., Hogan, P. G., Kallies, A., Lugli, E., Lynn, R. C., Philip, M., Rao, A., Restifo, N. P., *et al.* (2019). Defining 'T cell exhaustion'. Nat. Rev. Immunol. **19**, 665–674 10.1038/s41577-019-0221-9.

54. Kahan, S. M., Wherry, E. J. & Zajac, A. J. (2015). T cell exhaustion during persistent viral infections. Virology vols 479–480 180–193 10.1016/j.virol.2014.12.033.

55. Korman, A. J., Peggs, K. S. & Allison, J. P. (2006). Checkpoint Blockade in Cancer Immunotherapy. Advances in Immunology vol. 90 297–339 10.1016/S0065-2776(06)90008-X.

56. Ribas, A. & Wolchok, J. D. (2018). Cancer immunotherapy using checkpoint blockade. Science vol. 359 1350–1355 10.1126/science.aar4060.

57. Barrueto, L., Caminero, F., Cash, L., Makris, C., Lamichhane, P. & Deshmukh, R. R. (2020). Resistance to Checkpoint Inhibition in Cancer Immunotherapy. Translational Oncology vol. 13 10.1016/j.tranon.2019.12.010.

58. Thommen, D. S. & Schumacher, T. N. (2018). T Cell Dysfunction in Cancer. Cancer Cell vol. 33 547–562 10.1016/j.ccell.2018.03.012.

59. Wherry, E. J. (2011). T cell exhaustion. Nature Immunology vol. 12 492–499 10.1038/ni.2035.

60. Simmons, K. B., Wubeshet, M., Ames, K. T., McMahan, C. J., Hale, J. S. & Fink, P. J. (2012). Modulation of TCRβ surface expression during TCR revision. Cell. Immunol. **272**, 124–129 10.1016/j.cellimm.2011.10.022.

61. Kuhns, M. S., Davis, M. M. & Garcia, K. C. (2006). Deconstructing the form and function of the TCR/CD3 complex. Immunity vol. 24 133–139 10.1016/j.immuni.2006.01.006.

62. Dong, D., Zheng, L., Lin, J., Zhang, B., Zhu, Y., Li, N., Xie, S., Wang, Y., Gao, N. & Huang, Z. (2019). Structural basis of assembly of the human T cell receptor–CD3 complex. Nature **573**, 546–552 10.1038/s41586-019-1537-0.

63. Sasmal, D. K., Feng, W., Roy, S., Leung, P., He, Y., Cai, C., Cao, G., Lian, H., Qin, J., Hui, E., *et al.* (2019). TCR–pMHC bond conformation controls TCR ligand discrimination. Cell. Mol. Immunol. doi:10.1038/s41423-019-0273-6 10.1038/s41423-019-0273-6.

64. Wang, H., Kadlecek, T. A., Au-Yeung, B. B., Goodfellow, H. E. S., Hsu, L. Y., Freedman, T. S. & Weiss, A. (2010). ZAP-70: an essential kinase in T-cell signaling. Cold Spring Harbor perspectives in biology vol. 2 10.1101/cshperspect.a002279.

65. Courtney, A. H., Lo, W. L. & Weiss, A. (2018). TCR Signaling: Mechanisms of Initiation and Propagation. Trends in Biochemical Sciences vol. 43 108–123 10.1016/j.tibs.2017.11.008.

66. Zhang, W., Irvin, B. J., Trible, R. P., Abraham, R. T. & Samelson, L. E. (1999). Functional analysis of LAT in TCR-mediated signaling pathways using a LAT-deficient Jurkat cell line. Int. Immunol. **11**, 943–950 10.1093/intimm/11.6.943.

67. Balagopalan, L., Kortum, R. L., Coussens, N. P., Barr, V. A. & Samelson, L. E. (2015). The linker for activation of T Cells (LAT) signaling hub: From signaling complexes to microclusters. Journal of Biological Chemistry vol. 290 26422–26429 10.1074/jbc.R115.665869.

68. Mueller, D. L., Jenkins, M. K. & Schwartz, R. H. (1989). Clonal expansion versus functional clonal inactivation: A costimulatory signalling pathway determines the outcome of T cell antigen receptor occupancy. Annual Review of Immunology vol. 7 445–480 10.1146/annurev.iy.07.040189.002305.

69. Bretscher, P. & Cohn, M. (1970). A theory of self-nonself discrimination. Science (80-. ). **169**, 1042–1049 10.1126/science.169.3950.1042.

70. June, C. H., Ledbetter, J. A., Gillespie, M. M., Lindsten, T. & Thompson, C. B. (1987). T-cell proliferation involving the CD28 pathway is associated with cyclosporine-resistant interleukin 2 gene expression. Mol. Cell. Biol. **7**, 4472–4481 10.1128/mcb.7.12.4472.

71. Chen, L. & Flies, D. B. (2013). Molecular mechanisms of T cell co-stimulation and co-inhibition. Nature Reviews Immunology vol. 13 227–242 10.1038/nri3405.

72. Courtney, A. H., Lo, W.-L. & Weiss, A. (2018). TCR Signaling: Mechanisms of Initiation and Propagation. Trends Biochem. Sci. **43**, 108–123 10.1016/j.tibs.2017.11.008.

73. Sharma, P. & Allison, J. P. (2015). The future of immune checkpoint therapy. Science **348**, 56–61 10.1126/science.aaa8172.

74. Krummel, M. F. & Allison, J. P. (1995). CD28 and CTLA-4 have opposing effects on the response of T ceils to stimulation. J. Exp. Med. **182**, 459–465 10.1084/jem.182.2.459.

75. Walunas, T. L., Lenschow, D. J., Bakker, C. Y., Linsley, P. S., Freeman, G. J., Green, J. M., Thompson, C. B. & Bluestone, J. A. (1994). CTLA-4 can function as a negative regulator of T cell activation. Immunity **1**, 405–413 10.1016/1074-7613(94)90071-X.

76. Yokosuka, T., Kobayashi, W., Takamatsu, M., Sakata-Sogawa, K., Zeng, H., Hashimoto-Tane, A., Yagita, H., Tokunaga, M. & Saito, T. (2010). Spatiotemporal Basis of CTLA-4 Costimulatory Molecule-Mediated Negative Regulation of T Cell Activation. Immunity **33**, 326–339 10.1016/j.immuni.2010.09.006.

77. Xu, X., Hou, B., Fulzele, A., Masubuchi, T., Zhao, Y., Wu, Z., Hu, Y., Jiang, Y., Ma, Y., Wang, H., *et al.* (2020). PD-1 and BTLA regulate T cell signaling differentially and only partially through SHP1 and SHP2. J. Cell Biol. **219**, 10.1083/JCB.201905085.

78. Sheppard, K. A., Fitz, L. J., Lee, J. M., Benander, C., George, J. A., Wooters, J., Qiu, Y., Jussif, J. M., Carter, L. L., Wood, C. R., *et al.* (2004). PD-1 inhibits T-cell receptor induced phosphorylation of the ZAP70/CD3ζ signalosome and downstream signaling to PKCθ. FEBS Lett. **574**, 37–41 10.1016/j.febslet.2004.07.083.

79. Alarcón, B., Mestre, D. & Martínez-Martín, N. (2011). The immunological synapse: A cause or consequence of T-cell receptor triggering? Immunology vol. 133 420–425 10.1111/j.1365-2567.2011.03458.x.

80. Grakoui, A., Bromley, S. K., Sumen, C., Davis, M. M., Shaw, A. S., Allen, P. M. & Dustin, M. L. (1999). The immunological synapse: A molecular machine controlling T cell activation. Science (80-. ). **285**, 221–227 10.1126/science.285.5425.221.

81. Purtic, B., Pitcher, L. A., Van Oers, N. S. C. & Wülfing, C. (2005). T cell receptor (TCR)

clustering in the immunological synapse integrates TCR and costimulatory signaling in selected T cells. Proc. Natl. Acad. Sci. U. S. A. **102**, 2904–2909 10.1073/pnas.0406867102.

82. Monks, C. R. F., Freiberg, B. A., Kupfer, H., Sciaky, N. & Kupfer, A. (1998). Three-dimensional segregation of supramolecular activation clusters in T cells. Nature **395**, 82–86 10.1038/25764.

83. Yokosuka, T. & Saito, T. (2010). The Immunological Synapse, TCR Microclusters, and T Cell Activation. in 81–107 (Springer, Berlin, Heidelberg, 2010). doi:10.1007/978-3-642-03858-7_5 10.1007/978-3-642-03858-7_5.

84. Fooksman, D. R., Vardhana, S., Vasiliver-Shamis, G., Liese, J., Blair, D. A., Waite, J., Sacristán, C., Victora, G. D., Zanin-Zhorov, A. & Dustin, M. L. (2010). Functional anatomy of T cell activation and synapse formation. Annu. Rev. Immunol. **28**, 79–105 10.1146/annurev-immunol-030409-101308.

85. Freiberg, B. A., Kupfer, H., Maslanik, W., Delli, J., Kappler, J., Zaller, D. M. & Kupfer, A. (2002). Staging and resetting T cell activation in SMACs. Nat. Immunol. **3**, 911–917 10.1038/ni836.

86. Beck-García, K., Beck-García, E., Bohler, S., Zorzin, C., Sezgin, E., Levental, I., Alarcón, B. & Schamel, W. W. A. (2015). Nanoclusters of the resting T cell antigen receptor (TCR) localize to non-raft domains. Biochim. Biophys. Acta - Mol. Cell Res. **1853**, 802–809 10.1016/j.bbamcr.2014.12.017.

87. Kumar, R., Ferez, M., Swamy, M., Arechaga, I., Rejas, M. T., Valpuesta, J. M., Schamel, W. W. A., Alarcon, B. & van Santen, H. M. (2011). Increased Sensitivity of Antigen-Experienced T Cells through the Enrichment of Oligomeric T Cell Receptor Complexes. Immunity **35**, 375–387 10.1016/j.immuni.2011.08.010.

88. Schamel, W. W. A., Arechaga, I., Risueño, R. M., Van Santen, H. M., Cabezas, P., Risco, C., Valpuesta, J. M. & Alarcón, B. (2005). Coexistence of multivalent and monovalent TCRs explains high sensitivity and wide range of response. J. Exp. Med. **202**, 493–503 10.1084/jem.20042155.

89. Pageon, S. V., Tabarin, T., Yamamoto, Y., Ma, Y., Bridgeman, J. S., Cohnen, A., Benzing, C., Gao, Y., Crowther, M. D., Tungatt, K., *et al.* (2016). Functional role of T-cell receptor nanoclusters in signal initiation and antigen discrimination. Proc. Natl. Acad. Sci. U. S. A. **113**, E5454–E5463 10.1073/pnas.1607436113.

90. Lillemeier, B. F., Mörtelmaier, M. A., Forstner, M. B., Huppa, J. B., Groves, J. T. & Davis, M. M. (2010). TCR and Lat are expressed on separate protein islands on T cell membranes and concatenate during activation. Nat. Immunol. **11**, 90–96 10.1038/ni.1832.

91. Krummel, M. F., Sjaastad, M. D., Wulfing, C. W. & Davis, M. M. (2000). Differential clustering of CD4 and CD3ζ during T cell recognition. Science (80-. ). **289**, 1349–1352 10.1126/science.289.5483.1349.

92. Bunnell, S. C., Hong, D. I., Kardon, J. R., Yamazaki, T., McGlade, C. J., Barr, V. A. & Samelson, L. E. (2002). T cell receptor ligation induces the formation of dynamically regulated signaling assemblies. J. Cell Biol. **158**, 1263–1275 10.1083/jcb.200203043.

93. Yi, J., Balagopalan, L., Nguyen, T., McIntire, K. M. & Samelson, L. E. (2019). TCR microclusters

form spatially segregated domains and sequentially assemble in calcium-dependent kinetic steps. Nat. Commun. **10**, 1–13 10.1038/s41467-018-08064-2.

94. Yokosuka, T., Sakata-Sogawa, K., Kobayashi, W., Hiroshima, M., Hashimoto-Tane, A., Tokunaga, M., Dustin, M. L. & Saito, T. (2005). Newly generated T cell receptor microclusters initiate and sustain T cell activation by recruitment of Zap70 and SLP-76. Nat. Immunol. **6**, 1253–1262 10.1038/ni1272.

95. Campi, G., Varma, R. & Dustin, M. L. (2005). Actin and agonist MHC-peptide complex-dependent T cell receptor microclusters as scaffolds for signaling. J. Exp. Med. **202**, 1031–1036 10.1084/jem.20051182.

96. Chung, W., Abel, S. M. & Chakraborty, A. K. (2012). Protein Clusters on the T Cell Surface May Suppress Spurious Early Signaling Events. PLoS One **7**, e44444 10.1371/journal.pone.0044444.

97. Rossboth, B., Arnold, A. M., Ta, H., Platzer, R., Kellner, F., Huppa, J. B., Brameshuber, M., Baumgart, F. & Schütz, G. J. (2018). TCRs are randomly distributed on the plasma membrane of resting antigen-experienced T cells. Nat. Immunol. **19**, 821–827 10.1038/s41590-018-0162-7.

98. Morita, D., Iwashita, C., Mizutani, T., Mori, N., Mikami, B. & Sugita, M. (2020). Crystal structure of the ternary complex of TCR, MHC class I and lipopeptides. Int. Immunol. **32**, 805–810 10.1093/intimm/dxaa050.

99. Brameshuber, M., Kellner, F., Rossboth, B. K., Ta, H., Alge, K., Sevcsik, E., Göhring, J., Axmann, M., Baumgart, F., Gascoigne, N. R. J., *et al.* (2018). Monomeric TCRs drive T cell antigen recognition. Nat. Immunol. **19**, 487–496 10.1038/s41590-018-0092-4.

100. Leisegang, M., Engels, B., Schreiber, K., Yew, P. Y., Kiyotani, K., Idel, C., Arina, A., Duraiswamy, J., Rweichselbaum, R., Uckert, W., *et al.* (2016). Eradication of large solid tumors by gene therapy with a T-cell receptor targeting a single cancer-specific point mutation. Clin. Cancer Res. **22**, 2734–2743 10.1158/1078-0432.CCR-15-2361.

101. Lawless, J. F. (2002). *Statistical Models and Methods for Lifetime Data* (John Wiley & Sons, Inc., 2002). doi:10.1002/9781118033005 10.1002/9781118033005.

102. McInnes, L., Healy, J. & Melville, J. (2018). UMAP: Uniform Manifold Approximation and Projection for Dimension Reduction.

103. Coifman, R. R. & Lafon, S. (2006). Diffusion maps. Appl. Comput. Harmon. Anal. **21**, 5–30 10.1016/J.ACHA.2006.04.006.

104. by WALTER SI IEWHA RT, E. A. & Wilks, S. S. *Statistical Models and Methods for Lifetime Data, 2nd ed. (Wiley Series in Probability and Statistics)*.

105. Li, S., Gou, T., Wang, Q., Chen, M., Chen, Z., Xu, M., Wang, Y., Han, D., Cao, R., Liu, J., *et al.* (2020). Ultrasound/Optical Dual-Modality Imaging for Evaluation of Vulnerable Atherosclerotic Plaques with Osteopontin Targeted Nanoparticles. Macromol. Biosci. **20**, 10.1002/mabi.201900279.

106. Mattrey, R. F., Brown, J. J., Shelton, R. E., Ogino, M. T., Johnson, K. K. & Mitten, R. M. (1991). Use of perfluorooctylbromide (PFOB)to detect liver abscesses with computed tomography: Safety

and efficacy. Invest. Radiol. **26**, 792–798 10.1097/00004424-199109000-00003.

107. Huang, J., Edwards, L. J., Evavold, B. D. & Zhu, C. (2007). Kinetics of MHC-CD8 Interaction at the T Cell Membrane. J. Immunol. **179**, 7653–7662 10.4049/jimmunol.179.11.7653.

108. Hsu, H. Y., Nicholson, A. C. & Hajjar, D. P. (1996). Inhibition of macrophage scavenger receptor activity by tumor necrosis factor-α is transcriptionally and post-transcriptionally regulated. J. Biol. Chem. **271**, 7767–7773 10.1074/jbc.271.13.7767.

109. Liu, S. L., Wang, Z. G., Xie, H. Y., Liu, A. A., Lamb, D. C. & Pang, D. W. (2020). Single-Virus Tracking: From Imaging Methodologies to Virological Applications. Chemical Reviews vol. 120 1936–1979 10.1021/acs.chemrev.9b00692.

110. Huang, L.-K. & Wang, M.-J. J. Image thresholding by minimizing the measures of fuzziness. Pattern Recognit. **28**, 41–51.

111. Cypel, M., Yeung, J. C., Hirayama, S., Rubacha, M., Fischer, S., Anraku, M., Sato, M., Harwood, S., Pierre, A., Waddell, T. K., *et al.* (2008). Technique for Prolonged Normothermic Ex Vivo Lung Perfusion. J. Hear. Lung Transplant. **27**, 1319–1325 10.1016/j.healun.2008.09.003.

112. Ross, J. T., Nesseler, N., Lee, J. W., Ware, L. B. & Matthay, M. A. (2019). The ex vivo human lung: Research value for translational science. JCI Insight **4**, 10.1172/jci.insight.128833.

113. Kahan, S. M., Wherry, E. J. & Zajac, A. J. (2015). T cell exhaustion during persistent viral infections. Virology vols 479–480 180–193 10.1016/j.virol.2014.12.033.

114. Charles A Janeway, Jr, Paul Travers, Mark Walport, and M. J. S. (2001). Immunobiology - 5th edition. Garland Science https://www.ncbi.nlm.nih.gov/books/NBK10757/ (2001).

115. Janeway, K. M. C. W. C. (2008). *Janeway's Immunobiology* (Garland Science, 2008).

116. Janeway, C. A. (1992). The T Cell Receptor as a Multicomponent Signalling Machine: CD4/CD8 Coreceptors and CD45 in T Cell Activation. Annu. Rev. Immunol. **10**, 645–674 10.1146/annurev.iy.10.040192.003241.

117. Kumar, B. V., Connors, T. J. & Farber, D. L. (2018). Human T Cell Development, Localization, and Function throughout Life. Immunity vol. 48 202–213 10.1016/j.immuni.2018.01.007.

118. Chen, T. & Guestrin, C. *XGBoost: A Scalable Tree Boosting System* https://github.com/dmlc/xgboost.

119. Ferguson, A. L., Panagiotopoulos, A. Z., Debenedetti, P. G. & Kevrekidis, I. G. (2010). Systematic determination of order parameters for chain dynamics using diffusion maps. Proc. Natl. Acad. Sci. U. S. A. **107**, 13597–13602 10.1073/pnas.1003293107.

120. Chakraborty, A. K. & Weiss, A. (2014). Insights into the initiation of TCR signaling. Nature Immunology vol. 15 798–807 10.1038/ni.2940.

121. Van Der Merwe, P. A. & Dushek, O. (2011). Mechanisms for T cell receptor triggering. Nature Reviews Immunology vol. 11 47–55 10.1038/nri2887.

122. Schamel, W. W. A., Arechaga, I., Risueño, R. M., Van Santen, H. M., Cabezas, P., Risco, C.,

Valpuesta, J. M. & Alarcón, B. (2005). Coexistence of multivalent and monovalent TCRs explains high sensitivity and wide range of response. J. Exp. Med. **202**, 493–503 10.1084/jem.20042155.

123. Smoligovets, A. A., Smith, A. W., Wu, H. J., Petit, R. S. & Groves, J. T. (2012). Characterization of dynamic actin associations with T-cell receptor microclusters in primary T cells. J. Cell Sci. **125**, 735–742 10.1242/jcs.092825.

124. Varma, R., Campi, G., Yokosuka, T., Saito, T. & Dustin, M. L. (2006). T Cell Receptor-Proximal Signals Are Sustained in Peripheral Microclusters and Terminated in the Central Supramolecular Activation Cluster. Immunity **25**, 117–127 10.1016/j.immuni.2006.04.010.

125. Wang, Q.-L., Liang, J.-Q., Gong, B.-N., Xie, J.-J., Yi, Y.-T., Lan, X. & Li, Y. (2019). T Cell Receptor (TCR)-Induced PLC-γ1 Sumoylation via PIASxβ and PIAS3 SUMO E3 Ligases Regulates the Microcluster Assembly and Physiological Function of PLC-γ1. Front. Immunol. **10**, 10.3389/fimmu.2019.00314.

126. Yi, J., Balagopalan, L., Nguyen, T., McIntire, K. M. & Samelson, L. E. (2019). TCR microclusters form spatially segregated domains and sequentially assemble in calcium-dependent kinetic steps. Nat. Commun. **10**, 10.1038/s41467-018-08064-2.

127. Yokosuka, T., Sakata-Sogawa, K., Kobayashi, W., Hiroshima, M., Hashimoto-Tane, A., Tokunaga, M., Dustin, M. L. & Saito, T. (2005). Newly generated T cell receptor microclusters initiate and sustain T cell activation by recruitment of Zap70 and SLP-76. Nat. Immunol. **6**, 1253–1262 10.1038/ni1272.

128. Campi, G., Varma, R. & Dustin, M. L. (2005). Actin and agonist MHC-peptide complex-dependent T cell receptor microclusters as scaffolds for signaling. J. Exp. Med. **202**, 1031–1036 10.1084/jem.20051182.

129. Crites, T. J., Padhan, K., Muller, J., Krogsgaard, M., Gudla, P. R., Lockett, S. J. & Varma, R. (2014). TCR Microclusters Pre-Exist and Contain Molecules Necessary for TCR Signal Transduction. J. Immunol. **193**, 56–67 10.4049/jimmunol.1400315.

130. Hashimoto-Tane, A., Yokosuka, T., Sakata-Sogawa, K., Sakuma, M., Ishihara, C., Tokunaga, M. & Saito, T. (2011). Dynein-Driven Transport of T Cell Receptor Microclusters Regulates Immune Synapse Formation and T Cell Activation. Immunity **34**, 919–931 10.1016/j.immuni.2011.05.012.

131. Hashimoto-Tane, A. & Saito, T. (2016). Dynamic Regulation of TCR-Microclusters and the Microsynapse for T Cell Activation. Front. Immunol. **7**, 255 10.3389/fimmu.2016.00255.

132. Huang, J., Brameshuber, M., Zeng, X., Xie, J., Li, Q., Chien, Y., Valitutti, S. & Davis, M. M. (2013). A Single Peptide-Major Histocompatibility Complex Ligand Triggers Digital Cytokine Secretion in CD4+ T Cells. Immunity **39**, 846–857 10.1016/j.immuni.2013.08.036.

133. Lewis, J. B., Scangarello, F. A., Murphy, J. M., Eidell, K. P., Sodipo, M. O., Ophir, M. J., Sargeant, R., Seminario, M. C. & Bunnell, S. C. (2018). ADAP is an upstream regulator that precedes SLP-76 at sites of TCR engagement and stabilizes signaling microclusters. J. Cell Sci. **131**, 10.1242/jcs.215517.

134. Murugesan, S., Hong, J., Yi, J., Li, D., Beach, J. R., Shao, L., Meinhardt, J., Madison, G., Wu, X., Betzig, E., *et al.* (2016). Formin-generated actomyosin arcs propel t cell receptor microcluster

movement at the immune synapse. Journal of Cell Biology vol. 215 383–399 10.1083/jcb.201603080.

135. Roh, K.-H., Lillemeier, B. F., Wang, F. & Davis, M. M. (2015). The coreceptor CD4 is expressed in distinct nanoclusters and does not colocalize with T-cell receptor and active protein tyrosine kinase p56lck. Proc. Natl. Acad. Sci. U. S. A. **112**, E1604-13 10.1073/pnas.1503532112.

136. Lundberg, S. & Lee, S.-I. (2017). A Unified Approach to Interpreting Model Predictions.

137. Lundberg, S. M. & Allen, P. G. *Consistent feature attribution for tree ensembles* https://arxiv.org/pdf/1706.06060.pdf.

138. Fritz-Laylin, L. K., Riel-Mehan, M., Chen, B. C., Lord, S. J., Goddard, T. D., Ferrin, T. E., Nicholson-Dykstra, S. M., Higgs, H., Johnson, G. T., Betzig, E., *et al.* (2017). Actin-Based protrusions of migrating neutrophils are intrinsically lamellar and facilitate direction changes. Elife **6**, 10.7554/eLife.26990.

139. Gao, R., Asano, S. M., Upadhyayula, S., Pisarev, I., Milkie, D. E., Liu, T. L., Singh, V., Graves, A., Huynh, G. H., Zhao, Y., *et al.* (2019). Cortical column and whole-brain imaging with molecular contrast and nanoscale resolution. Science (80-. ). **363**, 10.1126/science.aau8302.

140. Ritter, A. T., Asano, Y., Stinchcombe, J. C., Dieckmann, N. M. G., Chen, B. C., Gawden-Bone, C., van Engelenburg, S., Legant, W., Gao, L., Davidson, M. W., *et al.* (2015). Actin Depletion Initiates Events Leading to Granule Secretion at the Immunological Synapse. Immunity doi:10.1016/j.immuni.2015.04.013 10.1016/j.immuni.2015.04.013.

141. Cai, E., Marchuk, K., Beemiller, P., Beppler, C., Rubashkin, M. G., Weaver, V. M., Gérard, A., Liu, T.-L., Chen, B.-C., Betzig, E., *et al.* (2017). Visualizing dynamic microvillar search and stabilization during ligand detection by T cells. Science **356**, eaal3118 10.1126/science.aal3118.

142. Condon, N. D., Heddleston, J. M., Chew, T. L., Luo, L., McPherson, P. S., Ioannou, M. S., Hodgson, L., Stow, J. L. & Wall, A. A. (2018). Macropinosome formation by tent pole ruffling in macrophages. J. Cell Biol. **217**, 3873–3885 10.1083/jcb.201804137.

143. David, A. F., Roudot, P., Legant, W. R., Betzig, E., Danuser, G. & Gerlich, D. W. (2019). Augmin accumulation on long-lived microtubules drives amplification and kinetochore-directed growth. J. Cell Biol. **218**, 2150–2168 10.1083/jcb.201805044.

144. Merwe, P. A. van der & Davis, S. J. (2003). M OLECULAR I NTERACTIONS M EDIATING T C ELL A NTIGEN R ECOGNITION . Annu. Rev. Immunol. **21**, 659–684 10.1146/annurev.immunol.21.120601.141036.

145. Thorn, K. (2016). A quick guide to light microscopy in cell biology. Mol. Biol. Cell **27**, 219–222 10.1091/mbc.E15-02-0088.

146. Rudd, C. E., Trevillyan, J. M., Dasgupta, J. D., Wong, L. L. & Schlossman, S. F. (1988). The CD4 receptor is complexed in detergent lysates to a protein-tyrosine kinase (pp58) from human T lymphocytes. Proc. Natl. Acad. Sci. U. S. A. **85**, 5190–5194 10.1073/pnas.85.14.5190.

147. Veillette, A., Bookman, M. A., Horak, E. M. & Bolen, J. B. (1988). The CD4 and CD8 T cell surface antigens are associated with the internal membrane tyrosine-protein kinase p56lck. Cell

**55**, 301–308 10.1016/0092-8674(88)90053-0.

148. Janeway, C. A., Carding, S., Jones, B., Murray, J., Portoles, P., Rasmussen, R., Rojo, J., Saizawa, K., West, J. & Bottomly, K. (1988). CD4+ T Cells: Specificity and Function. Immunol. Rev. **101**, 39–80 10.1111/j.1600-065X.1988.tb00732.x.

149. Boise, L. H., Minn, A. J., Noel, P. J., June, C. H., Accavitti, M. A., Lindsten, T. & Thompson, C. B. (1995). CD28 costimulation can promote T cell survival by enhancing the expression of Bcl-xL. Immunity **3**, 87–98 10.1016/1074-7613(95)90161-2.

150. Esensten, J. H., Helou, Y. A., Chopra, G., Weiss, A. & Bluestone, J. A. (2016). CD28 Costimulation: From Mechanism to Therapy. Immunity vol. 44 973–988 10.1016/j.immuni.2016.04.020.

151. Linsley, P. S. & Ledbetter, J. A. (1993). The Role of the CD28 Receptor During T Cell Responses to Antigen. Annu. Rev. Immunol. **11**, 191–212 10.1146/annurev.iy.11.040193.001203.

152. Jenkins, M. K., Ashwell, J. D. & Schwartz, R. H. (1988). Allogeneic non-T spleen cells restore the responsiveness of normal T cell clones stimulated with antigen and chemically modified antigen-presenting cells. J. Immunol. **140**, 3324–30.

153. Mueller, D. L., Jenkins, M. K. & Schwartz, R. H. (1989). An accessory cell-derived costimulatory signal acts independently of protein kinase C activation to allow T cell proliferation and prevent the induction of unresponsiveness. J. Immunol. **142**, 2617–28.

154. Zaitsu, M., Issa, F., Hester, J., Vanhove, B. & Wood, K. J. (2017). Selective blockade of CD28 on human T cells facilitates regulation of alloimmune responses. JCI Insight **2**, 10.1172/jci.insight.89381.

155. Hui, E., Cheung, J., Zhu, J., Su, X., Taylor, M. J., Wallweber, H. A., Sasmal, D. K., Huang, J., Kim, J. M., Mellman, I., *et al.* (2017). T cell costimulatory receptor CD28 is a primary target for PD-1-mediated inhibition. Science (80-. ). **355**, 1428–1433 10.1126/science.aaf1292.

156. Kamphorst, A. O., Wieland, A., Nasti, T., Yang, S., Zhang, R., Barber, D. L., Konieczny, B. T., Daugherty, C. Z., Koenig, L., Yu, K., *et al.* (2017). Rescue of exhausted CD8 T cells by PD-1-targeted therapies is CD28-dependent. Science (80-. ). **355**, 1423–1427 10.1126/science.aaf0683.

157. Chen, L. & Flies, D. B. (2013). Molecular mechanisms of T cell co-stimulation and co-inhibition. Nature Reviews Immunology vol. 13 227–242 10.1038/nri3405.

158. Rowshanravan, B., Halliday, N. & Sansom, D. M. (2018). CTLA-4: A moving target in immunotherapy. Blood vol. 131 58–67 10.1182/blood-2017-06-741033.

159. Linsley, P. S., Bradshaw, J., Greene, J. A., Peach, R., Bennett, K. L. & Mittler, R. S. (1996). Intracellular trafficking of CTLA-4 and focal localization towards sites of TCR engagement. Immunity **4**, 535–543 10.1016/S1074-7613(00)80480-X.

160. Buchbinder, E. I. & Desai, A. (2016). CTLA-4 and PD-1 pathways similarities, differences, and implications of their inhibition. American Journal of Clinical Oncology: Cancer Clinical Trials vol. 39 98–106 10.1097/COC.0000000000000239.

161. Arasanz, H., Gato-Cañas, M., Zuazo, M., Ibañez-Vea, M., Breckpot, K., Kochan, G. & Escors, D. (2017). PD1 signal transduction pathways in T cells. Oncotarget vol. 8 51936–51945 10.18632/oncotarget.17232.

162. Karwacz, K., Bricogne, C., MacDonald, D., Arce, F., Bennett, C. L., Collins, M. & Escors, D. (2011). PD-L1 co-stimulation contributes to ligand-induced T cell receptor down-modulation on CD8 + T cells. EMBO Mol. Med. **3**, 581–592 10.1002/emmm.201100165.

163. Hanahan, D. & Weinberg, R. A. (2011). Hallmarks of cancer: The next generation. Cell vol. 144 646–674 10.1016/j.cell.2011.02.013.

164. Gide, T. N., Quek, C., Menzies, A. M., Scolyer, R. A., Long, G. V & Wilmott Correspondence, J. S. (2019). Distinct Immune Cell Populations Define Response to Anti-PD-1 Monotherapy and Anti-PD-1/Anti-CTLA-4 Combined Therapy. Cancer Cell **35**, 238-255.e6 10.1016/j.ccell.2019.01.003.

165. Gauci, M. L., Lanoy, E., Champiat, S., Caramella, C., Ammari, S., Aspeslagh, S., Varga, A., Baldini, C., Bahleda, R., Gazzah, A., *et al.* (2019). Long-term survival in patients responding to anti-PD-1/PD-L1 therapy and disease outcome upon treatment discontinuation. Clin. Cancer Res. **25**, 946–956 10.1158/1078-0432.CCR-18-0793.

166. Ngoi, N. Y. L., Heong, V., Lee, X. W., Huang, Y. Q., Thian, Y. L., Choo, B. A., Lim, D., Lim, Y. W., Lim, S. E., Ilancheran, A., *et al.* (2018). Tumor molecular profiling of responders and non-responders following pembrolizumab monotherapy in chemotherapy resistant advanced cervical cancer. Gynecol. Oncol. Reports **24**, 1–5 10.1016/j.gore.2018.01.009.

167. Cohen, J. V. & Flaherty, K. T. (2019). Response to immune checkpoint antibodies: Not all responses are created equal. Clin. Cancer Res. **25**, 910–911 10.1158/1078-0432.CCR-18-3296.

168. Topalian, S. L., Taube, J. M. & Pardoll, D. M. (2020). Neoadjuvant checkpoint blockade for cancer immunotherapy. Science vol. 367 10.1126/science.aax0182.

169. Irvine, D. J., Purbhoo, M. A., Krogsgaard, M. & Davis, M. M. (2002). Direct observation of ligand recognition by T cells. Nature **419**, 845–849 10.1038/nature01076.

170. Huang, J., Zarnitsyna, V. I., Liu, B., Edwards, L. J., Jiang, N., Evavold, B. D. & Zhu, C. (2010). The kinetics of two-dimensional TCR and pMHC interactions determine T-cell responsiveness. Nature doi:10.1038/nature08944 10.1038/nature08944.

171. Alam, S. M., Travers, P. J., Wung, J. L., Nasholds, W., Redpath, S., Jameson, S. C. & Gascoigne, N. R. J. (1996). T cell-receptor affinity and thymocyte positive selection. Nature **381**, 616–620 10.1038/381616a0.

172. Kersh, G. J., Kersh, E. N., Fremont, D. H. & Allen, P. M. (1998). High- and low-potency ligands with similar affinities for the TCR: The importance of kinetic in TCR signaling. Immunity **9**, 817–826 10.1016/S1074-7613(00)80647-0.

173. Corse, E., Gottschalk, R. A., Krogsgaard, M. & Allison, J. P. (2010). Attenuated T Cell Responses to a High-Potency Ligand In Vivo. PLoS Biol. **8**, e1000481 10.1371/journal.pbio.1000481.

174. Rabinowitz, J. D., Beeson, C., Wülfing, C., Tate, K., Allen, P. M., Davis, M. M. & McConnell, H.

M. (1996). Altered T cell receptor ligands trigger a subset of early T cell signals. Immunity **5**, 125–135 10.1016/S1074-7613(00)80489-6.

175. Li, Q. J., Dinner, A. R., Qi, S., Irvine, D. J., Huppa, J. B., Davis, M. M. & Chakraborty, A. K. (2004). CD4 enhances T cell sensitivity to antigen by coordinating Lck accumulation at the immunological synapse. Nat. Immunol. **5**, 791–799 10.1038/ni1095.

176. Li, W., Joshi, M. D., Singhania, S., Ramsey, K. H. & Murthy, A. K. (2014). Peptide vaccine: Progress and challenges. Vaccines vol. 2 515–536 10.3390/vaccines2030515.

177. Hos, B. J., Tondini, E., van Kasteren, S. I. & Ossendorp, F. (2018). Approaches to improve chemically defined synthetic peptide vaccines. Frontiers in Immunology vol. 9 884 10.3389/fimmu.2018.00884.

178. Barr, V. A., Bernot, K. M., Srikanth, S., Gwack, Y., Balagopalan, L., Regan, C. K., Helman, D. J., Sommers, C. L., Oh-hora, M., Rao, A., *et al.* (2008). Dynamic movement of the calcium sensor STIM1 and the calcium channel orai1 in activated T-cells: Puncta and distal caps. Mol. Biol. Cell **19**, 2802–2817 10.1091/mbc.E08-02-0146.

179. Cullinan, P., Sperling, A. I. & Burkhardt, J. K. (2002). The distal pole complex: a novel membrane domain distal to the immunological synapse. Immunol. Rev. **189**, 111–122 10.1034/j.1600-065X.2002.18910.x.

180. Allenspach, E. J., Cullinan, P., Tong, J., Tang, Q., Tesciuba, A. G., Cannon, J. L., Takahashi, S. M., Morgan, R., Burkhardt, J. K. & Sperling, A. I. (2001). ERM-dependent movement of CD43 defines a novel protein complex distal to the immunological synapse. Immunity **15**, 739–750 10.1016/S1074-7613(01)00224-2.

181. Chloéguedj, C., Abraham, N., Jullié1, D. J. & Randriamampita, C. (2016). T cell adhesion triggers an early signaling pole distal to the immune synapse. doi:10.1242/jcs.182311 10.1242/jcs.182311.

182. Cullinan, P., Sperling, A. I. & Burkhardt, J. K. (2002). The distal pole complex: a novel membrane domain distal to the immunological synapse. Immunol. Rev. **189**, 111–122 10.1034/j.1600-065X.2002.18910.x.

183. Billadeau, D. D., Nolz, J. C. & Gomez, T. S. (2007). Regulation of T-cell activation by the cytoskeleton. Nature Reviews Immunology vol. 7 131–143 10.1038/nri2021.

184. Bunnell, S. C., Kapoor, V., Trible, R. P., Zhang, W. & Samelson, L. E. (2001). Dynamic actin polymerization drives T cell receptor-induced spreading: A role for the signal transduction adaptor LAT. Immunity **14**, 315–329 10.1016/S1074-7613(01)00112-1.

185. Fritzsche, M., Fernandes, R. A., Chang, V. T., Colin-York, H., Clausen, M. P., Felce, J. H., Galiani, S., Erlenkämper, C., Santos, A. M., Heddleston, J. M., *et al.* (2017). Cytoskeletal actin dynamics shape a ramifying actin network underpinning immunological synapse formation. Sci. Adv. **3**, 10.1126/sciadv.1603032.

186. Kumari, S., Curado, S., Mayya, V. & Dustin, M. L. (2014). T cell antigen receptor activation and actin cytoskeleton remodeling. Biochimica et Biophysica Acta - Biomembranes vol. 1838 546–556 10.1016/j.bbamem.2013.05.004.

187. Roy, N. H. & Burkhardt, J. K. (2018). The actin cytoskeleton: A mechanical intermediate for signal integration at the immunological synapse. Front. Cell Dev. Biol. **6**, 10.3389/fcell.2018.00116.

188. Tsopoulidis, N., Kaw, S., Laketa, V., Kutscheidt, S., Baarlink, C., Stolp, B., Grosse, R. & Fackler, O. T. (2019). T cell receptor–triggered nuclear actin network formation drives CD4+ T cell effector functions. Sci. Immunol. **4**, 10.1126/sciimmunol.aav1987.

189. Valitutti, S., Dessing, M., Aktories, K., Gallati, H. & Lanzavecchia, A. (1995). Sustained signaling leading to t cell activation results from prolonged t cell receptor occupancy. role of t cell actin cytoskeleton. J. Exp. Med. **181**, 577–584 10.1084/jem.181.2.577.

190. Kummerow, C., Junker, C., Kruse, K., Rieger, H., Quintana, A. & Hoth, M. (2009). The immunological synapse controls local and global calcium signals in T lymphocytes. Immunological Reviews vol. 231 132–147 10.1111/j.1600-065X.2009.00811.x.

191. Billadeau, D. D., Nolz, J. C. & Gomez, T. S. (2007). Regulation of T-cell activation by the cytoskeleton. Nature Reviews Immunology vol. 7 131–143 10.1038/nri2021.

192. Serrador, J. M., Nieto, M. & Sánchez-Madrid, F. (1999). Cytoskeletal rearrangement during migration and activation of T lymphocytes. Trends in Cell Biology vol. 9 228–233 10.1016/S0962-8924(99)01553-6.

193. Kumari, S., Curado, S., Mayya, V. & Dustin, M. L. (2014). T cell antigen receptor activation and actin cytoskeleton remodeling. Biochimica et Biophysica Acta - Biomembranes vol. 1838 546–556 10.1016/j.bbamem.2013.05.004.

194. Hashimoto-Tane, A., Yokosuka, T., Sakata-Sogawa, K., Sakuma, M., Ishihara, C., Tokunaga, M. & Saito, T. (2011). Dynein-Driven Transport of T Cell Receptor Microclusters Regulates Immune Synapse Formation and T Cell Activation. Immunity **34**, 919–931 10.1016/j.immuni.2011.05.012.

195. Hashimoto-Tane, A. & Saito, T. (2016). Dynamic regulation of TCR-microclusters and the microsynapse for T cell activation. Frontiers in Immunology vol. 7 1 10.3389/fimmu.2016.00255.

196. Burkhardt, J. K. (2013). Cytoskeletal function in the immune system. Immunol. Rev. **256**, 5–9 10.1111/imr.12121.

197. Ritter, A. T., Angus, K. L. & Griffiths, G. M. (2013). The role of the cytoskeleton at the immunological synapse. Immunol. Rev. **256**, 107–117 10.1111/imr.12117.

198. DeMond, A. L., Mossman, K. D., Starr, T., Dustin, M. L. & Groves, J. T. (2008). T cell receptor microcluster transport through molecular mazes reveals mechanism of translocation. Biophys. J. **94**, 3286–3292 10.1529/biophysj.107.119099.

199. Gomez, T. S. & Billadeau, D. D. (2008). T Cell Activation and the Cytoskeleton: You Can't Have One Without the Other. Advances in Immunology vol. 97 1–64 10.1016/S0065-2776(08)00001-1.

200. Burkhardt, J. K., Carrizosa, E. & Shaffer, M. H. (2008). The Actin Cytoskeleton in T Cell Activation. Annu. Rev. Immunol. **26**, 233–259 10.1146/annurev.immunol.26.021607.090347.

201. Kumari, S., Depoil, D., Martinelli, R., Judokusumo, E., Carmona, G., Gertler, F. B., Kam, L. C.,

Carman, C. V., Burkhardt, J. K., Irvine, D. J., *et al.* (2015). Actin foci facilitate activation of the phospholipase C-γ in primary T lymphocytes via the WASP pathway. Elife **2015**, 1–31 10.7554/eLife.04953.

202. June, C. H., O'Connor, R. S., Kawalekar, O. U., Ghassemi, S. & Milone, M. C. (2018). CAR T cell immunotherapy for human cancer. Science vol. 359 1361–1365 10.1126/science.aar6711.

203. Guedj, C., Abraham, N., Jullié, D. & Randriamampita, C. (2016). T cell adhesion triggers an early signaling pole distal to the immune synapse. J. Cell Sci. **129**, 2526–2537 10.1242/jcs.182311.

204. Allenspach, E. J., Cullinan, P., Tong, J., Tang, Q., Tesciuba, A. G., Cannon, J. L., Takahashi, S. M., Morgan, R., Burkhardt, J. K. & Sperling, A. I. (2001). ERM-Dependent Movement of CD43 Defines a Novel Protein Complex Distal to the Immunological Synapse. Immunity **15**, 739–750 10.1016/S1074-7613(01)00224-2.

205. Mosenden, R., Moltu, K., Ruppelt, A., Berge, T. & Taskén, K. (2011). Effects of Type I Protein Kinase A Modulation on the T Cell Distal Pole Complex. Scand. J. Immunol. **74**, 568–573 10.1111/j.1365-3083.2011.02611.x.

206. Brown, C. E. & Mackall, C. L. (2019). CAR T cell therapy: inroads to response and resistance. Nat. Rev. Immunol. **19**, 73–74 10.1038/s41577-018-0119-y.

207. Martinez, M. & Moon, E. K. (2019). CAR T cells for solid tumors: New strategies for finding, infiltrating, and surviving in the tumor microenvironment. Front. Immunol. **10**, 10.3389/fimmu.2019.00128.

208. Eyquem, J., Mansilla-Soto, J., Giavridis, T., Van Der Stegen, S. J. C., Hamieh, M., Cunanan, K. M., Odak, A., Gönen, M. & Sadelain, M. (2017). Targeting a CAR to the TRAC locus with CRISPR/Cas9 enhances tumour rejection. Nature **543**, 113–117 10.1038/nature21405.

209. Stadtmauer, E. A., Fraietta, J. A., Davis, M. M., Cohen, A. D., Weber, K. L., Lancaster, E., Mangan, P. A., Kulikovskaya, I., Gupta, M., Chen, F., *et al.* (2020). CRISPR-engineered T cells in patients with refractory cancer. Science (80-. ). **367**, 10.1126/science.aba7365.

210. Stenger, D., Stief, T. A., Kaeuferle, T., Willier, S., Rataj, F., Schober, K., Vick, B., Lotfi, R., Wagner, B., Grünewald, T. G. P., *et al.* (2020). Endogenous TCR promotes in vivo persistence of CD19-CAR-T cells compared to a CRISPR/Cas9-mediated TCR knockout CAR. Blood **136**, 1407–1418 10.1182/blood.2020005185.

211. Lee, D. W., Kochenderfer, J. N., Stetler-Stevenson, M., Cui, Y. K., Delbrook, C., Feldman, S. A., Fry, T. J., Orentas, R., Sabatino, M., Shah, N. N., *et al.* (2015). T cells expressing CD19 chimeric antigen receptors for acute lymphoblastic leukaemia in children and young adults: A phase 1 dose-escalation trial. Lancet **385**, 517–528 10.1016/S0140-6736(14)61403-3.

212. Maude, S. L., Frey, N., Shaw, P. A., Aplenc, R., Barrett, D. M., Bunin, N. J., Chew, A., Gonzalez, V. E., Zheng, Z., Lacey, S. F., *et al.* (2014). Chimeric Antigen Receptor T Cells for Sustained Remissions in Leukemia. N. Engl. J. Med. **371**, 1507–1517 10.1056/nejmoa1407222.

213. Long, A. H., Haso, W. M., Shern, J. F., Wanhainen, K. M., Murgai, M., Ingaramo, M., Smith, J. P., Walker, A. J., Kohler, M. E., Venkateshwara, V. R., *et al.* (2015). 4-1BB costimulation ameliorates T cell exhaustion induced by tonic signaling of chimeric antigen receptors. Nat. Med.

**21**, 581–590 10.1038/nm.3838.

214. Savoldo, B., Ramos, C. A., Liu, E., Mims, M. P., Keating, M. J., Carrum, G., Kamble, R. T., Bollard, C. M., Gee, A. P., Mei, Z., *et al.* (2011). CD28 costimulation improves expansion and persistence of chimeric antigen receptor-modified T cells in lymphoma patients. J. Clin. Invest. **121**, 1822–1826 10.1172/JCI46110.

215. Dong, E., Du, H. & Gardner, L. (2020). An interactive web-based dashboard to track COVID-19 in real time. The Lancet Infectious Diseases vol. 20 533–534 10.1016/S1473-3099(20)30120-1.

216. Florindo, H. F., Kleiner, R., Vaskovich-Koubi, D., Acúrcio, R. C., Carreira, B., Yeini, E., Tiram, G., Liubomirski, Y. & Satchi-Fainaro, R. (2020). Immune-mediated approaches against COVID-19. Nat. Nanotechnol. **15**, 630–645 10.1038/s41565-020-0732-3.

217. Shin, M. D., Shukla, S., Chung, Y. H., Beiss, V., Chan, S. K., Ortega-Rivera, O. A., Wirth, D. M., Chen, A., Sack, M., Pokorski, J. K., *et al.* (2020). COVID-19 vaccine development and a potential nanomaterial path forward. Nature Nanotechnology vol. 15 646–655 10.1038/s41565-020-0737-y.

218. Walls, A. C., Park, Y. J., Tortorici, M. A., Wall, A., McGuire, A. T. & Veesler, D. (2020). Structure, Function, and Antigenicity of the SARS-CoV-2 Spike Glycoprotein. Cell **181**, 281-292.e6 10.1016/j.cell.2020.02.058.

219. Vabret, N., Britton, G. J., Gruber, C., Hegde, S., Kim, J., Kuksin, M., Levantovsky, R., Malle, L., Moreira, A., Park, M. D., *et al.* (2020). Immunology of COVID-19: Current State of the Science. Immunity vol. 52 910–941 10.1016/j.immuni.2020.05.002.

220. Shang, J., Ye, G., Shi, K., Wan, Y., Luo, C., Aihara, H., Geng, Q., Auerbach, A. & Li, F. (2020). Structural basis of receptor recognition by SARS-CoV-2. Nature **581**, 221–224 10.1038/s41586-020-2179-y.

221. Shang, J., Wan, Y., Luo, C., Ye, G., Geng, Q., Auerbach, A. & Li, F. (2020). Cell entry mechanisms of SARS-CoV-2. Proc. Natl. Acad. Sci. U. S. A. **117**, 10.1073/pnas.2003138117.

222. Lei, C., Qian, K., Li, T., Zhang, S., Fu, W., Ding, M. & Hu, S. (2020). Neutralization of SARS-CoV-2 spike pseudotyped virus by recombinant ACE2-Ig. Nat. Commun. **11**, 10.1038/s41467-020-16048-4.

223. Monteil, V., Kwon, H., Prado, P., Hagelkrüys, A., Wimmer, R. A., Stahl, M., Leopoldi, A., Garreta, E., Hurtado del Pozo, C., Prosper, F., *et al.* (2020). Inhibition of SARS-CoV-2 Infections in Engineered Human Tissues Using Clinical-Grade Soluble Human ACE2. Cell **181**, 905-913.e7 10.1016/j.cell.2020.04.004.

224. Chi, X., Yan, R., Zhang, J., Zhang, G., Zhang, Y., Hao, M., Zhang, Z., Fan, P., Dong, Y., Yang, Y., *et al.* (2020). A neutralizing human antibody binds to the N-terminal domain of the Spike protein of SARS-CoV-2. Science (80-. ). **369**, 650–655 10.1126/science.abc6952.

225. Rogers, T. F., Zhao, F., Huang, D., Beutler, N., Burns, A., He, W. T., Limbo, O., Smith, C., Song, G., Woehl, J., *et al.* (2020). Isolation of potent SARS-CoV-2 neutralizing antibodies and protection from disease in a small animal model. Science (80-. ). **369**, 956–963 10.1126/science.abc7520.

226. Shi, R., Shan, C., Duan, X., Chen, Z., Liu, P., Song, J., Song, T., Bi, X., Han, C., Wu, L., *et al.* (2020). A human neutralizing antibody targets the receptor-binding site of SARS-CoV-2. Nature **584**, 120–124 10.1038/s41586-020-2381-y.

227. Cao, Y., Su, B., Guo, X., Sun, W., Deng, Y., Bao, L., Zhu, Q., Zhang, X., Zheng, Y., Geng, C., *et al.* (2020). Potent Neutralizing Antibodies against SARS-CoV-2 Identified by High-Throughput Single-Cell Sequencing of Convalescent Patients' B Cells. Cell **182**, 73-84.e16 10.1016/j.cell.2020.05.025.

228. Chen, X., Li, R., Pan, Z., Qian, C., Yang, Y., You, R., Zhao, J., Liu, P., Gao, L., Li, Z., *et al.* (2020). Human monoclonal antibodies block the binding of SARS-CoV-2 spike protein to angiotensin converting enzyme 2 receptor. Cellular and Molecular Immunology vol. 17 647–649 10.1038/s41423-020-0426-7.

229. Chen, P., Nirula, A., Heller, B., Gottlieb, R. L., Boscia, J., Morris, J., Huhn, G., Cardona, J., Mocherla, B., Stosor, V., *et al.* (2020). SARS-CoV-2 Neutralizing Antibody LY-CoV555 in Outpatients with Covid-19. N. Engl. J. Med. doi:10.1056/nejmoa2029849 10.1056/nejmoa2029849.

230. Chen, W., Cai, B., Geng, Z., Chen, F., Wang, Z., Wang, L. & Chen, X. (2020). Reducing False Negatives in COVID-19 Testing by Using Microneedle-Based Oropharyngeal Swabs. doi:10.1016/j.matt.2020.09.021 10.1016/j.matt.2020.09.021.

231. Torrente-Rodríguez, R. M., Lukas, H., Tu, J., Min, J., Yang, Y., Xu, C., Rossiter, H. B. & Gao, W. (2020). SARS-CoV-2 RapidPlex: A Graphene-Based Multiplexed Telemedicine Platform for Rapid and Low-Cost COVID-19 Diagnosis and Monitoring. Matter **3**, 1981–1998 10.1016/j.matt.2020.09.027.

232. Qin, Z., Peng, R., Baravik, I. K. & Liu, X. (2020). Fighting COVID-19: Integrated Micro- and Nanosystems for Viral Infection Diagnostics. Matter vol. 3 628–651 10.1016/j.matt.2020.06.015.

233. Cai, X., Prominski, A., Lin, Y., Ankenbruck, N., Rosenberg, J., Chen, M., Shi, J., Chang, E. B., Penaloza-MacMaster, P., Tian, B., *et al.* (2020). A neutralizing antibody-conjugated photothermal nanoparticle captures and inactivates SARS-CoV-2. bioRxiv 2020.11.30.404624 doi:10.1101/2020.11.30.404624 10.1101/2020.11.30.404624.

234. Rao, L., Xia, S., Xu, W., Tian, R., Yu, G., Gu, C., Pan, P., Meng, Q. F., Cai, X., Qu, D., *et al.* (2020). Decoy nanoparticles protect against COVID-19 by concurrently adsorbing viruses and inflammatory cytokines. Proc. Natl. Acad. Sci. U. S. A. **117**, 27141–27147 10.1073/pnas.2014352117.

235. Zhang, Q., Honko, A., Zhou, J., Gong, H., Downs, S. N., Vasquez, J. H., Fang, R. H., Gao, W., Griffiths, A. & Zhang, L. (2020). Cellular Nanosponges Inhibit SARS-CoV-2 Infectivity. Nano Lett. **20**, 5570–5574 10.1021/acs.nanolett.0c02278.

236. Daassi, D., Mahoney, K. M. & Freeman, G. J. (2020). The importance of exosomal PDL1 in tumour immune evasion. Nature Reviews Immunology vol. 20 209–215 10.1038/s41577-019-0264-y.

237. Gordon, S. (2016). Phagocytosis: An Immunobiologic Process. Immunity vol. 44 463–475 10.1016/j.immuni.2016.02.026.

238. Liao, M., Liu, Y., Yuan, J., Wen, Y., Xu, G., Zhao, J., Cheng, L., Li, J., Wang, X., Wang, F., *et al.* (2020). Single-cell landscape of bronchoalveolar immune cells in patients with COVID-19. Nat. Med. **26**, 842–844 10.1038/s41591-020-0901-9.

239. Fadok, V. A., Bratton, D. L., Frasch, S. C., Warner, M. L. & Henson, P. M. (1998). The role of phosphatidylserine in recognition of apoptotic cells by phagocytes. Cell Death and Differentiation vol. 5 551–562 10.1038/sj.cdd.4400404.

240. Wu, Y., Tibrewal, N. & Birge, R. B. (2006). Phosphatidylserine recognition by phagocytes: a view to a kill. Trends in Cell Biology vol. 16 189–197 10.1016/j.tcb.2006.02.003.

241. Aderem, A. & Underhill, D. M. (1999). Mechanisms of phagocytosis in macrophages. Annual Review of Immunology vol. 17 593–623 10.1146/annurev.immunol.17.1.593.

242. Johnstone, S. A., Masin, D., Mayer, L. & Bally, M. B. (2001). Surface-associated serum proteins inhibit the uptake of phosphatidylserine and poly(ethylene glycol) liposomes by mouse macrophages. Biochim. Biophys. Acta - Biomembr. **1513**, 25–37 10.1016/S0005-2736(01)00292-9.

243. Shah, N. K., Gupta, S. K., Wang, Z. & Meenach, S. A. (2019). Enhancement of macrophage uptake via phosphatidylserine-coated acetalated dextran nanoparticles. J. Drug Deliv. Sci. Technol. **50**, 57–65 10.1016/j.jddst.2019.01.013.

244. Divithotawela, C., Cypel, M., Martinu, T., Singer, L. G., Binnie, M., Chow, C. W., Chaparro, C., Waddell, T. K., De Perrot, M., Pierre, A., *et al.* (2019). Long-term Outcomes of Lung Transplant with Ex Vivo Lung Perfusion. JAMA Surg. **154**, 1143–1150 10.1001/jamasurg.2019.4079.

245. Wang, Q., Zhang, Y., Wu, L., Niu, S., Song, C., Zhang, Z., Lu, G., Qiao, C., Hu, Y., Yuen, K. Y., *et al.* (2020). Structural and Functional Basis of SARS-CoV-2 Entry by Using Human ACE2. Cell **181**, 894-904.e9 10.1016/j.cell.2020.03.045.

246. Hwang, S. S., Lim, J., Yu, Z., Kong, P., Sefik, E., Xu, H., Harman, C. C. D., Kim, L. K., Lee, G. R., Li, H. B., *et al.* (2020). MRNA destabilization by BTG1 and BTG2 maintains T cell quiescence. Science (80-. ). **367**, 1255–1260 10.1126/science.abb2507.

247. Lan, J., Ge, J., Yu, J., Shan, S., Zhou, H., Fan, S., Zhang, Q., Shi, X., Wang, Q., Zhang, L., *et al.* (2020). Structure of the SARS-CoV-2 spike receptor-binding domain bound to the ACE2 receptor. Nature **581**, 215–220 10.1038/s41586-020-2180-5.

248. Torchilin, V. P. (2005). Recent advances with liposomes as pharmaceutical carriers. Nature Reviews Drug Discovery vol. 4 145–160 10.1038/nrd1632.

249. Riley, R. S., June, C. H., Langer, R. & Mitchell, M. J. (2019). Delivery technologies for cancer immunotherapy. Nature Reviews Drug Discovery vol. 18 175–196 10.1038/s41573-018-0006-z.

250. Allen, T. M. & Cullis, P. R. (2013). Liposomal drug delivery systems: From concept to clinical applications. Advanced Drug Delivery Reviews vol. 65 36–48 10.1016/j.addr.2012.09.037.

251. Torchilin, V. P. (2014). Multifunctional, stimuli-sensitive nanoparticulate systems for drug delivery. Nature Reviews Drug Discovery vol. 13 813–827 10.1038/nrd4333.

252. Suk, J. S., Xu, Q., Kim, N., Hanes, J. & Ensign, L. M. (2016). PEGylation as a strategy for improving nanoparticle-based drug and gene delivery. Advanced Drug Delivery Reviews vol. 99 28–51 10.1016/j.addr.2015.09.012.

253. He, C., Hu, Y., Yin, L., Tang, C. & Yin, C. (2010). Effects of particle size and surface charge on cellular uptake and biodistribution of polymeric nanoparticles. Biomaterials **31**, 3657–3666 10.1016/j.biomaterials.2010.01.065.

254. Champion, J. A., Walker, A. & Mitragotri, S. (2008). Role of particle size in phagocytosis of polymeric microspheres. Pharm. Res. **25**, 1815–1821 10.1007/s11095-008-9562-y.

255. Doane, T. L., Chuang, C. H., Hill, R. J. & Burda, C. (2012). Nanoparticle ζ -potentials. Acc. Chem. Res. **45**, 317–326 10.1021/ar200113c.

256. Howarth, M., Chinnapen, D. J. F., Gerrow, K., Dorrestein, P. C., Grandy, M. R., Kelleher, N. L., El-Husseini, A. & Ting, A. Y. (2006). A monovalent streptavidin with a single femtomolar biotin binding site. Nat. Methods **3**, 267–273 10.1038/nmeth861.

257. Toita, R., Kawano, T., Murata, M. & Kang, J. H. (2016). Anti-obesity and anti-inflammatory effects of macrophage-targeted interleukin-10-conjugated liposomes in obese mice. Biomaterials **110**, 81–88 10.1016/j.biomaterials.2016.09.018.

258. Harel-Adar, T., Mordechai, T. Ben, Amsalem, Y., Feinberg, M. S., Leor, J. & Cohen, S. (2011). Modulation of cardiac macrophages by phosphatidylserine-presenting liposomes improves infarct repair. Proc. Natl. Acad. Sci. U. S. A. **108**, 1827–1832 10.1073/pnas.1015623108.

259. Han, C. Z., Juncadella, I. J., Kinchen, J. M., Buckley, M. W., Klibanov, A. L., Dryden, K., Onengut-Gumuscu, S., Erdbrügger, U., Turner, S. D., Shim, Y. M., *et al.* (2016). Macrophages redirect phagocytosis by non-professional phagocytes and influence inflammation. Nature **539**, 570–574 10.1038/nature20141.

260. Lund, M. E., To, J., O'Brien, B. A. & Donnelly, S. (2016). The choice of phorbol 12-myristate 13-acetate differentiation protocol influences the response of THP-1 macrophages to a pro-inflammatory stimulus. J. Immunol. Methods **430**, 64–70 10.1016/j.jim.2016.01.012.

261. Chan, K. K., Dorosky, D., Sharma, P., Abbasi, S. A., Dye, J. M., Kranz, D. M., Herbert, A. S. & Procko, E. (2020). Engineering human ACE2 to optimize binding to the spike protein of SARS coronavirus 2. Science (80-. ). **369**, 1261–1265 10.1126/SCIENCE.ABC0870.

262. Matsuyama, S., Nao, N., Shirato, K., Kawase, M., Saito, S., Takayama, I., Nagata, N., Sekizuka, T., Katoh, H., Kato, F., *et al.* (2020). Enhanced isolation of SARS-CoV-2 by TMPRSS2-expressing cells. Proc. Natl. Acad. Sci. U. S. A. **117**, 7001–7003 10.1073/pnas.2002589117.

263. Beigel, J. H., Tomashek, K. M., Dodd, L. E., Mehta, A. K., Zingman, B. S., Kalil, A. C., Hohmann, E., Chu, H. Y., Luetkemeyer, A., Kline, S., *et al.* (2020). Remdesivir for the Treatment of Covid-19 — Final Report. N. Engl. J. Med. doi:10.1056/nejmoa2007764 10.1056/nejmoa2007764.

264. Wang, Y., Zhang, D., Du, G., Du, R., Zhao, J., Jin, Y., Fu, S., Gao, L., Cheng, Z., Lu, Q., *et al.* (2020). Remdesivir in adults with severe COVID-19: a randomised, double-blind, placebo-controlled, multicentre trial. Lancet **395**, 1569–1578 10.1016/S0140-6736(20)31022-9.

265. Grein, J., Ohmagari, N., Shin, D., Diaz, G., Asperges, E., Castagna, A., Feldt, T., Green, G., Green, M. L., Lescure, F.-X., *et al.* (2020). Compassionate Use of Remdesivir for Patients with Severe Covid-19. N. Engl. J. Med. **382**, 2327–2336 10.1056/nejmoa2007016.

266. Shen, C., Wang, Z., Zhao, F., Yang, Y., Li, J., Yuan, J., Wang, F., Li, D., Yang, M., Xing, L., *et al.* (2020). Treatment of 5 Critically Ill Patients with COVID-19 with Convalescent Plasma. JAMA - J. Am. Med. Assoc. **323**, 1582–1589 10.1001/jama.2020.4783.

267. Pérez-Cameo, C. & Marín-Lahoz, J. (2020). Serosurveys and convalescent plasma in COVID-19. EClinicalMedicine vol. 23 10.1016/j.eclinm.2020.100370.

268. Zhang, Q., Honko, A., Zhou, J., Gong, H., Downs, S. N., Vasquez, J. H., Fang, R. H., Gao, W., Griffiths, A. & Zhang, L. (2020). Cellular Nanosponges Inhibit SARS-CoV-2 Infectivity. Nano Lett. **20**, 5570–5574 10.1021/acs.nanolett.0c02278.

269. Fiorenza, S., Ritchie, D. S., Ramsey, S. D., Turtle, C. J. & Roth, J. A. (2020). Value and affordability of CAR T-cell therapy in the United States. Bone Marrow Transplantation vol. 55 1706–1715 10.1038/s41409-020-0956-8.

270. Yu, M., Wu, J., Shi, J. & Farokhzad, O. C. (2016). Nanotechnology for protein delivery: Overview and perspectives. J. Control. Release **240**, 24–37 10.1016/j.jconrel.2015.10.012.

271. Chen, G., Huang, A. C., Zhang, W., Zhang, G., Wu, M., Xu, W., Yu, Z., Yang, J., Wang, B., Sun, H., *et al.* (2018). Exosomal PD-L1 contributes to immunosuppression and is associated with anti-PD-1 response. Nature **560**, 382–386 10.1038/s41586-018-0392-8.

272. Mukherjee, A., Waters, A. K., Kalyan, P., Achrol, A. S., Kesari, S. & Yenugonda, V. M. (2019). Lipid-polymer hybrid nanoparticles as a nextgeneration drug delivery platform: State of the art, emerging technologies, and perspectives. International Journal of Nanomedicine vol. 14 1937–1952 10.2147/IJN.S198353.

273. Bournazos, S., Gupta, A. & Ravetch, J. V. (2020). The role of IgG Fc receptors in antibody-dependent enhancement. Nature Reviews Immunology vol. 20 633–643 10.1038/s41577-020-00410-0.

274. Lee, W. S., Wheatley, A. K., Kent, S. J. & DeKosky, B. J. (2020). Antibody-dependent enhancement and SARS-CoV-2 vaccines and therapies. Nat. Microbiol. **5**, 1185–1191 10.1038/s41564-020-00789-5.

275. Klichinsky, M., Ruella, M., Shestova, O., Lu, X. M., Best, A., Zeeman, M., Schmierer, M., Gabrusiewicz, K., Anderson, N. R., Petty, N. E., *et al.* (2020). Human chimeric antigen receptor macrophages for cancer immunotherapy. Nat. Biotechnol. **38**, 947–953 10.1038/s41587-020-0462-y.

276. Suzuki, T., Itoh, Y., Sakai, Y., Saito, A., Okuzaki, D., Motooka, D., Minami, S., Kobayashi, T., Yamamoto, T., Okamoto, T., *et al.* (2020). Generation of human bronchial organoids for SARS-CoV-2 research. Daisuke Okuzaki **4**, 2020.05.25.115600 10.1101/2020.05.25.115600.

277. Han, Y., Yang, L., Duan, X., Duan, F., Nilsson-Payant, B., Yaron, T., Wang, P., Tang, X., Zhang, T., Zhao, Z., *et al.* (2020). Identification of Candidate COVID-19 Therapeutics using hPSC-derived Lung Organoids. bioRxiv Prepr. Serv. Biol. doi:10.1101/2020.05.05.079095

10.1101/2020.05.05.079095.

278. Chandrashekar, A., Liu, J., Martino, A. J., McMahan, K., Mercad, N. B., Peter, L., Tostanosk, L. H., Yu, J., Maliga, Z., Nekorchuk, M., *et al.* (2020). SARS-CoV-2 infection protects against rechallenge in rhesus macaques. Science (80-. ). **369**, 812–817 10.1126/science.abc4776.

279. Yu, J., Tostanosk, L. H., Peter, L., Mercad, N. B., McMahan, K., Mahrokhia, S. H., Nkolol, J. P., Liu, J., Li, Z., Chandrashekar, A., *et al.* (2020). DNA vaccine protection against SARS-CoV-2 in rhesus macaques. Science (80-. ). **369**, 806–811 10.1126/science.abc6284.

280. Rockx, B., Kuiken, T., Herfst, S., Bestebroer, T., Lamers, M. M., Munnink, B. B. O., De Meulder, D., Van Amerongen, G., Van Den Brand, J., Okba, N. M. A., *et al.* (2020). Comparative pathogenesis of COVID-19, MERS, and SARS in a nonhuman primate model. Science (80-. ). **368**, 1012–1015 10.1126/science.abb7314.